The mitigation of underwater noise by a big bubble curtain

A study into the optimization of a big bubble curtain configuration and a contribution to noise mitigation modelling.

Karel Brandt

A thesis presented for the degree of
Master of Science
in Structural Engineering at the Delft University of Technology

Student number:	4331508	
Thesis committee:	Dr. ir. Apostolos Tsouvalas	TU Delft, chairman
	Dr. ir. Özkan Sertlek	TU Delft, supervisor
	MSc. P.J. Elzinga	Van Oord, supervisor
	MSc. G.J.W. Glasbergen	Van Oord, supervisor
	Dr. ir. G.J. de Boer	Van Oord, supervisor

Preface

Before you lies the thesis which concludes my time as a student at the Delft University of Technology. It has been a wonderful journey with mostly ups and a few downs. I have made friends and memories which I will cherish for the rest of my life and it has enriched me as a human being. I am grateful to my parents for making this all possible.

This thesis also concludes my time at Van Oord. I started as an intern in January of 2021 and have been promoted to graduate intern in July of 2021. Although I started in the middle of the COVID-19 pandemic, which made it tough at times, my colleagues and supervisors made the absolute best of the situation. For this, I would like to thank them.

Special appreciation goes to my two most involved supervisors at Van Oord, Jesper and Govert. Jesper, your pragmatic mindset and relaxed attitude helped me a lot in staying on the right path to achieve my goal. Govert, your expertise on underwater noise was essential at times when I needed it the most. In addition, I would like to thank Gerben for our nice evaluation meetings after every progress meeting. Your take on conveying information to the reader was inspiring and helped me a lot in writing my report.

Also, I would like to thank in particular my supervisor from the university, Özkan. You were always available for questions and discussions and never lost your patience. Your knowledge and dedication to your job was inspiring to me and will be inspiring to me throughout my career. I would like to express my gratitude to Apostolos, my chair, for sharing his knowledge in the field of underwater noise and for giving me the opportunity to graduate at Van Oord under his supervision.

Furthermore, I would like to thank my family and friends. In particular, my eight roommates who made graduating in times of covid a remarkable, at times difficult, experience to never forget. Lastly, I would like to thank Annabel for always being there for me.

Karel Brandt
May, 2022

Summary

With a worldwide growing consensus on fossil fuel combustion having a negative impact on climate, society, and biodiversity the urge for renewable energies is growing rapidly. One of the most widely used renewable energy sources is wind energy and for this purpose both onshore and offshore wind farms (OWFs) are being developed. In recent years the development of OWFs are getting more attractive due to fewer constraints on turbine size, more stable wind resources, and generally less environmental impact.

Offshore wind turbine generators (OWTGs) have various possible foundation concepts for shallow waters of which the monopile (MP) is the most widely used foundation concept. The dominant installation method for MPs is percussive pile driving where energy is transferred from a hydraulic impact hammer to the MP driving the latter into the seabed. Due to this energy transfer, a structural response is induced in the MP which in turn inflicts an acoustic response in the water column and surrounding soil.

The underwater noise emissions generated during offshore pile driving have a negative effect on the marine fauna. This negative effect can be subdivided in three categories, that is instant death or injury from single noise pulses, auditory damage due to accumulative noise, and behavioural disturbance. For this reason, government agencies have imposed rules and legislation concerning underwater noise thresholds during offshore pile driving. To comply with these noise limits, noise mitigation systems are often deployed during offshore construction works of which the big bubble curtain (BBC) is the most frequently applied. A BBC is formed by air being injected into the water through nozzles in air supply hoses laying on the seabed enclosing the entire MP.

Currently, the BBC configuration is often based on rules of thumb (Bellmann et al., 2020) and experience from similar past project. However, Bellmann et al. (2020) states that a BBC configuration can be optimized beforehand, depending on local technical-constructive and site-specific parameters. This thesis focuses on the link between the influence of different soil configurations on the characteristics of the underwater noise emissions and the intrinsic mitigation performance of a BBC and what this means for the design of a BBC configuration. One objective of this thesis is to provide a framework for optimizing a BBC configuration which consists of a quantitative and qualitative analysis.

For both analyses, use is made of the semi-analytical model SILENCE BUBBLES, which captures the acoustic interaction between MP, fluid, soil, and an air bubble curtain model. This air bubble curtain model makes use of a one-dimensional coupling approach to capture the interaction between the bubbly medium and the travelling sound wave. Another objective of this thesis is to investigate an alternative approach for modelling waves travelling through the bubbly medium taking

into account its two-dimensional properties, thus include the angle dependency of the incident sound wave.

Therefore, the focus of this thesis is twofold with the overarching theme; "Noise mitigation by a BBC". On the one hand, a framework for optimizing a BBC configuration is proposed which is applied to three different soil configurations. This framework consists of a quantitative and qualitative analysis. The qualitative analysis focuses on the effect of different soil configurations on the mitigation effectiveness of a BBC. The quantitative analysis provides an optimal combination of BBC configuration parameters for complying with a set noise limit. On the other hand, an alternative two-dimensional (2D) coupling approach is examined for coupling an air bubble curtain model to a non-mitigated field.

Optimizing mitigation by a BBC

A sensitivity analysis was performed to identify the model sensitivity to different BBC parameters. Here, it was shown that the model is sensitive to the nozzle diameter and the gas velocity at the nozzle. Furthermore, the radial distance of the BBC is of significant importance for the SEL at $r = 750$ m.

SILENCE BUBBLES can be used for a quantitative robust approach for determining an optimal configuration of a BBC for different soil configurations. Each soil configuration has its own distinct optimization process.

Together with a qualitative analysis regarding energy distribution over the radial distance and total energy being irradiated into the fluid domain, the framework presented can lead to a better estimation of whether noise limits will be met for future noise prognoses.

An alternative coupling approach for integrating an air bubble curtain model

This thesis presents a mode-coupling approach for coupling a similar air bubble curtain model as the one used in SILENCE BUBBLES to a non-mitigated field. The results showed that for higher frequencies ($f \geq 300$ Hz), the 1D approach is conservative compared to the 2D approach. For lower frequencies, the 2D approach is more conservative where the 1D approach shows significantly higher transmission loss for certain frequencies below 300 Hz. It could not be identified where these large differences come from.

Contents

List of Figures

List of Tables

Chapter 1

Introduction

With a worldwide growing consensus on fossil fuel combustion having a negative impact on climate, society, and biodiversity the urge for renewable energies is growing rapidly (Lima et al., 2020; Saidur et al., 2010). An alternative for fossil-fueled energy and one of the most widely used renewable energy sources is energy harvested from the wind (Sadorsky, 2021). According to Fried et al. (2017), wind power has proven to be a mature and reliable technology and is a competitive way of adding new sustainable power capacity to the energy grid. Bórawski et al. (2020) state that wind is one of the most promising sources of alternative energy. To harvest the energy from the wind, both on- and offshore wind farms (OWFs) are being developed. In recent years, the development of OWFs is getting more attractive due to fewer constraints on turbine size and more stable wind resources, together with generally less environmental impact (Li et al., 2020).

The offshore wind turbine generators (OWTG) have various possible foundation concepts for shallow waters, namely gravity-based foundations, monopiles, jacket structures, and tripod structures (Wu et al., 2019). Despite numerous available foundation concepts, the monopile (MP) is the most widely used foundation concept for shallow waters due to its simplicity, adaptability, and favourable structural behaviour (Sánchez et al., 2019). Eighty percent of all OWTG installations in the European waters in 2020 had an MP foundation (Ramírez et al., 2021).

The dominant installation method for MPs is percussive pile driving or pile driving. Here, use is made of a hydraulic impact hammer where an impact weight is dropped onto an anvil that rests on the MP's flange. A hammer strike onto the MP is referred to as a blow. The energy caused by the blow is transferred to the MP driving the latter into the seabed (Klages et al., 2019). Due to this energy transfer, a structural response is induced in the MP which in turn inflicts an acoustic response in the water column and the surrounding soil (Kuhn et al., 2014; Tsouvalas, 2020). These elastic waves can re-emerge and contribute to the acoustic response in the water column. Technical-constructive- and site-specific parameters have a strong influence on the radiated noise profile (Bellmann et al., 2020; Tsouvalas, 2020).

The underwater noise emissions generated during offshore pile driving have a negative effect on the marine fauna (Southall et al., 2019). This negative effect can be subdivided in three categories, that is instant death or injury from single noise pulses, auditory damage due to accumulative noise, and behavioural disturbance (P. M. Thompson et al., 2020). Due to these negative effects on marine fauna, governmental bodies from different countries have imposed rules and legislation concerning maximum underwater noise thresholds during offshore pile driving. Table 1.1 gives an overview of the noise quantities and their maximum values for The Netherlands (Rijkswaterstaat, 2016), Belgium (Degraer et al., 2018), and Germany (Müller et al., 2019).

Country	**Indicator**	**Limit**
The Netherlands	SEL	159-172 dB re 1 $\mu Pa^2 s$
Germany	SEL_{05} $\mathrm{L}_{\mathrm{p,pk}}$	160 dB re 1 $\mu Pa^2 s$ 190 dB re 1 μPa
Belgium	$\mathrm{L}_{\mathrm{p,pk}}$	185 dB re 1 μPa

Table 1.1: Legislation on maximum noise thresholds for offshore construction works at 750m from the noise source.

Apart from the countries depicted in Table 1.1, many countries have imposed noise limits. To comply with these limits, noise mitigation systems are deployed during heavy noise offshore construction works (Bellmann, 2014). There are numerous abatement systems currently available on the market, e.g., the noise mitigation screen (IHC-NMS), the hydro-sound damper (HSD), the AdBm system, and the cofferdam. However, the most frequently applied noise mitigation system is the single big bubble curtain (BBC) or double BBC with over several hundred applications in water depths up to 41 meters (Bellmann et al., 2020). A BBC is formed by air being injected into the water through perforated holes or nozzles in air supply hoses laying on the seabed enclosing the entire MP at a certain radial distance (Göttsche et al., 2013; Koschinski & Lüdemann, 2020). Figure 1.1a shows a schematic cross-section of an air supply hose laying on the seabed. Above the perforated hole, bubbles are formed due to the injection of air into the water. Figure 1.1b shows an aerial view of the application of a double BBC with the installation vessel in the center of the figure. The two rings are the rising bubbles which reach the sea surface.

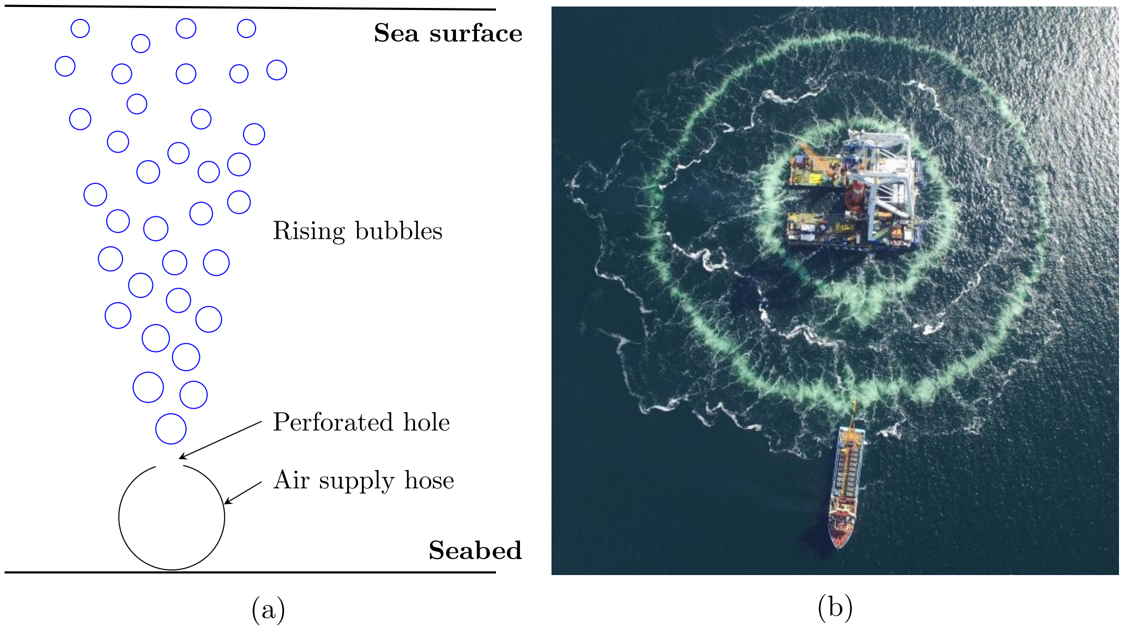

(a) (b)

Figure 1.1: (a) Schematic cross-section of an air supply hose laying on the seabed. (b) Aerial view of the application of a double BBC configuration.

1.1 Motivation for this research

This thesis treats two subjects in parallel with the overarching theme; "Noise mitigation by a BBC". This section describes the motivation for both subjects, where Section 1.1.1 and Section 1.1.2 describe the motivation for: "Optimizing mitigation by a BBC" and "An alternative coupling approach for integrating an air bubble curtain model", respectively.

1.1.1 Optimizing mitigation by a BBC

To comply with the set noise limits for offshore pile driving activities, a thorough understanding of the mitigation effectiveness of a BBC is of importance. According to Bellmann et al. (2020), both the intrinsic mitigation performance of the BBC and the characteristics of the underwater noise emissions influence the effectiveness of a BBC. The intrinsic mitigation performance of a BBC is solely dependent on the BBC parameters; i.e., gas velocity at the nozzle, nozzle diameter, and nozzle spacing.

The underwater noise emissions, or propagated sound field, caused by offshore pile driving can be divided into three noise paths (Tsouvalas, 2020). The primary and secondary noise path consist of direct radiation into the fluid domain and noise leaking back into the fluid domain through the soil, respectively. Lastly, noise is emitted in the fluid domain in the vicinity of the seabed by interface waves travelling along the fluid-soil interface (see Figure 1.2).

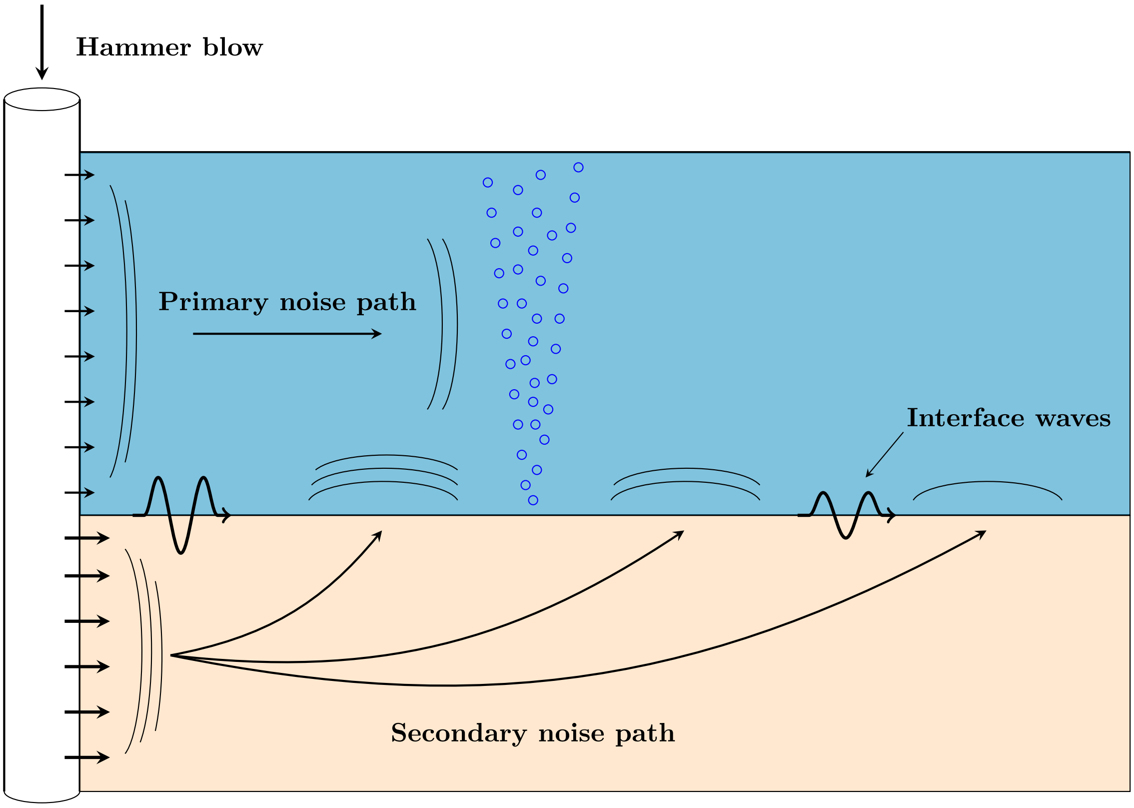

Figure 1.2: Schematization of underwater noise emissions due to offshore pile driving.

How and how much energy is irradiated from the MP through these noise paths into the fluid domain is determined by technical-constructive (e.g., pile diameter) and site-specific (e.g., water depth and soil configuration) factors. E.g., a larger pile diameter requires more energy to be driven into the soil due to larger soil resistance. Therefore, more energy is irradiatad into the fluid (primary noise path) and soil domain. In turn, the soil configuration and characteristics determine how and how much energy is leaked from the soil back into the fluid domain (secondary noise path and interface waves). Tsouvalas (2015) showed that around 1% of the total energy is irradiated into the fluid domain whereas 80-90% is irradiated into the soil domain making the soil a big factor of consideration for determining the mitigation effectiveness of a BBC.

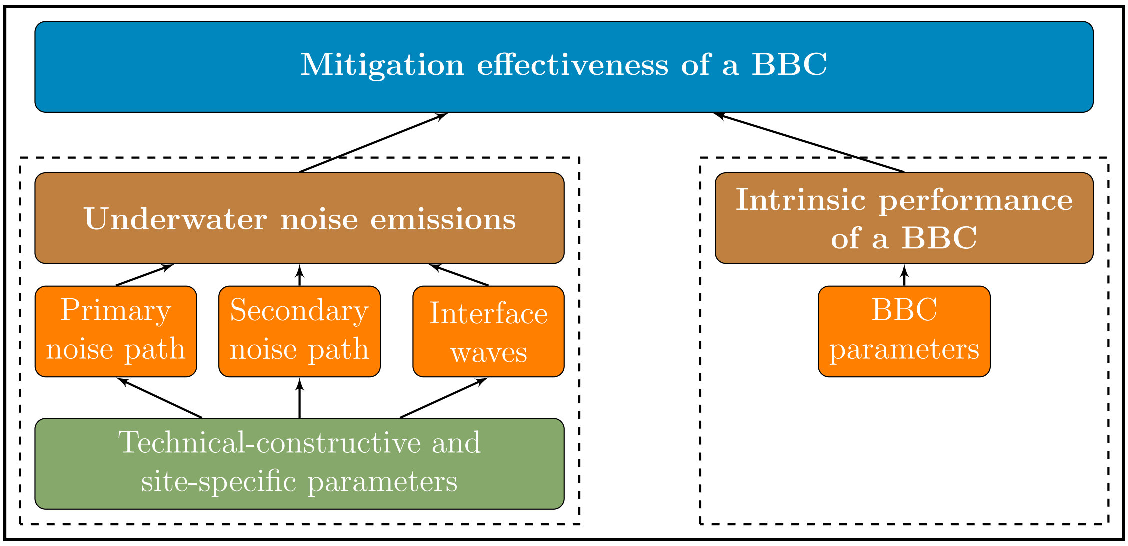

Figure 1.3: Visual overview of influencing factors for the mitigation effectiveness of a BBC.

To obtain a complete view of the mitigation effectiveness of a BBC, a link has to be made between the intrinsic mitigation performance of the BBC and the characteristics of the underwater noise emissions. These characteristics are in turn influenced by the technical-constructive and site-specific parameters (see Figure 1.3). Questions remain regarding this link and what this means for a BBC configuration consisting of BBC parameters and the radial distance from the MP. Currently, the BBC configuration is often based on rules of thumb (Bellmann et al., 2020) and experience from similar past projects. According to personal communication within Van Oord, the radial distance of the air supply hose is generalized for all MPs despite a possible difference in soil configurations. However, this difference in soil configuration could mean a different leakage pattern through the secondary noise path which in turn requires a different radial distance of the BBC. BBC parameters can be adjusted to some extent in between MP installations to achieve more noise reduction, however, this is often a trial and error procedure. Bellmann et al. (2020) states that a BBC configuration can be optimized beforehand. One objective of this thesis is to provide a framework for optimizing a BBC configuration.

1.1.2 An alternative coupling approach for integrating an air bubble curtain model

All simulations predicting the noise propagation and mitigation are performed in SILENCE BUBBLES (Peng et al., 2021b). SILENCE BUBBLES is an extended version the semi-analytical model SILENCE (Peng et al., 2021a; Tsouvalas, 2015) by the integration of an air bubble curtain model (Bohne et al., 2020). SILENCE allows for the prediction of the propagated sound field by fully describing the coupled pile-water-soil interaction after a blow on the MP. The noise mitigation by a BBC is predicted by the integrated air bubble curtain model.

By means of discretization, this model approximates the triangular shaped distribution of an air bubble cloud. Based on the bubble distribution, the corresponding wave speed is determined for each discrete area (see Figure 1.4b; discrete areas enclosed by the dashed lines; triangular shaped air bubble curtain in blue). At the interface between each consecutive discrete area, an impedance mismatch occurs due to a difference in wave speed. A wave travelling through the air bubble curtain encounters multiple interfaces. Due to the impedance mismatch, the travelling wave is reflected and transmitted at each interface (see Figure 1.4c). As the energy of the incident wave is divided into a reflected and transmitted component, the energy of the transmitted travelling wave is lowered at each interface. In SILENCE BUBBLES, a transfer function captures the overall decrease in amplitude over the full width of the air bubble curtain taking into account every encountered interface. No impedance mismatch exists at the interfaces which fall outside the width of the air bubble curtain, therefore no reflection occurs at these interfaces.

This transfer function is based on a simplified approach where only the horizontal component of the travelling sound wave is taken into account where the actual incident sound wave is two-dimensional having also a vertical component (see Figure 1.4a). This vertical component is neglected in the current simplified approach, indicated by the dashed green vertical arrow in Figure 1.4a, thereby neglecting the angle dependency of the incident sound wave. This in turn leads to negligence of the angle dependency of the wave travelling through the air bubble curtain.

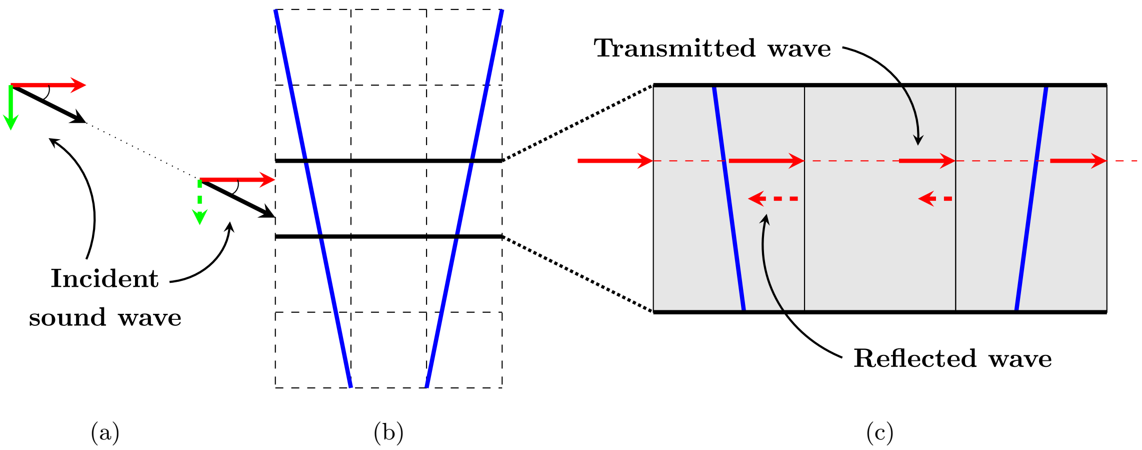

(a) (b) (c)

Figure 1.4: Schematization of (a) an incident sound wave under an angle with the vertical component in green and the horizontal component in red. (b) A discretization of the triangular shaped air bubble curtain in blue. (c) The reflected and transmitted waves due to the impedance mismatch.

Another objective of this thesis is to investigate an alternative approach for modelling waves travelling through the bubbly medium taking into account its two-dimensional properties, thus include the angle dependency of the incident sound wave. Subsequently, it is studied how this new approach can be implemented in SILENCE BUBBLES.

1.2 Research questions

This thesis treats two subjects in parallel with the overarching theme; "Noise mitigation by an air (big) bubble curtain". For both subjects, one main research question and two sub research questions were defined. The research questions are as follows where the main research questions are shown in bold.

1. **How can the effectiveness of a BBC configuration be optimized with respect to noise mitigation for a variety of scenarios using the predictive modelling software SILENCE BUBBLES?**
    (a) What is the model sensitivity to different BBC parameters and how can this sensitivity be determined by SILENCE BUBBLES?
    (b) What is the effect of different soil configurations on the performance of a BBC?
2. **What is the difference between a two-dimensional and a one-dimensional coupling approach with respect to noise mitigation?**
    (a) How can the effect of the two-dimensional coupling approach be modelled?
    (b) How can the two-dimensional coupling approach be integrated in SILENCE BUBBLES?

1.3 Approach

First, a literature study is performed in order to acquire the necessary background knowledge regarding underwater acoustics due to impact pile driving. An in depth study into the field of underwater ocean acoustics is performed in order to obtain a better understanding of the advanced SILENCE model. SILENCE is validated with measurement data from the **confidential** made available by Van Oord. To answer sub-question 1a, a parametric study is performed comprising of different soil configurations to provide more insight in the coupling between the propagated and mitigated sound field. Next, a sensitivity study is performed to highlight the model sensitivity to different BBC parameters to answer sub-question 1b. The sensitive parameters will be included in the optimization process. The effectiveness of the BBC will be analyzed for multiple distances from the MP. For each distance, the BBC parameters will be varied ranging from their predetermined minimum to maximum value to answer main research question 1.

Alongside these simulations, the focus is placed on the two-dimensional coupling approach. First, to increase comprehension of the current air bubble curtain model (Bohne et al., 2020) integrated into SILENCE BUBBLES, the less extensive but similar air bubble curtain model developed by Bohne et al. (2019) is reproduced. The effective wavenumber distribution is obtained and simplified to a depth and width independent distribution. To answer sub-question 2a, a point source is modelled in an ideal fluid waveguide to generate a pressure field and the simplified air bubble curtain model is implemented. A two-dimensional approach for coupling the travelling waves through the bubbly medium and subsequently coupling it to the free field is introduced and is compared to the current one-dimensional coupling. To answer sub-question 2b, an assessment will be made based on the modelling efforts on how this alternative coupling approach can be integrated into SILENCE BUBBLES. Main research question 2 will be answered by comparing the transmission loss results from the 1D and the 2D coupling approach.

1.4 Limitations

Prior to this research, its limitations are indicated. The number of geo-acoustic profiles of the ocean's bottom is infinite and each geo-acoustic profile has its own unique optimal BBC configuration. As it is not realistic to study all the geo-acoustic profiles, this thesis will only focus on providing an optimal configuration for three scenarios. Furthermore, bathymetry is not taken into account by the SILENCE model. The seabed is modelled as a perfectly flat surface, whereas in reality variation in the bathymetry occurs. However, according to T. Lippert et al. (2018), for moderate-range predictions the varying bathymetry has little influence on the sound predictions and the seabed can often be assumed flat. This applies to a lesser extent also to the sea surface. This is also modelled as a perfectly flat surface, whereas in reality a more rough sea state is expected (Sertlek & Blacquiere, 2019).

1.5 Thesis outline

The outline for this thesis is as follows.

- Chapter 2 provides a theoretical background in underwater acoustics. First, relevant acoustic quantities are explained. Secondly, the structure-borne noise due to offshore pile driving is explained after which the mitigation by an air bubble curtain is described.
- Chapter 3 comprises of a description of the sound reduction module in SILENCE BUBBLES. Furthermore, a validation of SILENCE is performed. Lastly, the base case BBC parameters are determined for the sensitivity study.
- Chapter 4 shows the sensitivity study, the qualitative analysis of the mitigation effectiveness of a BBC for different soil configurations, and the quantitative analysis for optimizing the mitigation by a BBC.
- Chapter 5 elaborates on the proposed two-dimensional coupling approach.

Chapter 2

Underwater noise due to offshore pile driving

This chapter presents a necessary acoustic background of this thesis and it's aim is to contribute to a better understanding of acoustic principles of offshore pile driving. First, the most common used acoustic quantities are addressed in Section 2.1. Subsequently, Section 2.2 describes the structure-borne noise generation due to offshore pile driving as well as the mitigation of noise by a BBC. An historic overview of predictive sound modelling and the state-of-the-art is given in Section 2.4. Lastly, the influencing factors for sound propagation and mitigation are described in Section 2.3.

2.1 Acoustic quantities

2.1.1 Pressure

Sound pressure or acoustic pressure is defined as the pressure derivation from the ambient static pressure caused by a travelling sound wave (Kim, 2010). Figure 2.1 shows a typical sound pressure variation signal in time. The SI-unit for the sound pressure is Pa (Jensen et al., 2011).

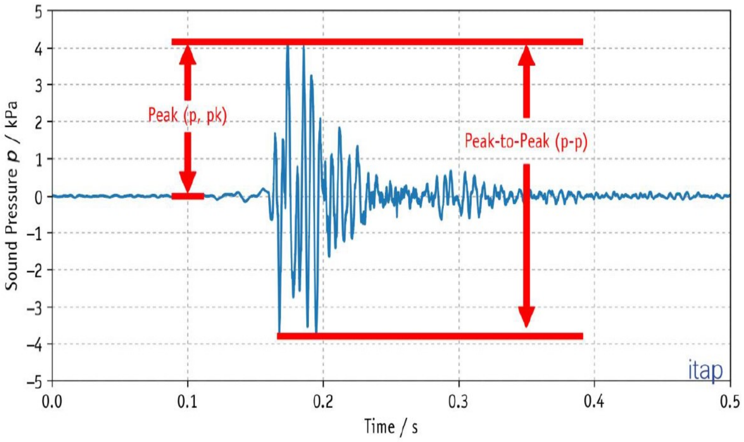

Figure 2.1: Typical sound pressure signal in time (Bellmann et al., 2020).

2.1.2 Acoustic impedance

Acoustic impedance (Z) is a physical property of the medium and describes the opposition of the medium to a travelling sound wave (Kaltenbacher, 2018). It is a measure of the ease with which the sound wave propagates through the medium and it is defined by Equation (2.1) (Jensen et al., 2011). It describes a relationship between the density of the medium ρ and the speed of sound in that medium c.

$$Z = \rho c \tag{2.1}$$

An impedance mismatch occurs when a wave travelling through a medium meets a medium with another wave speed and/or density. Because of this impedance mismatch part of the travelling wave is reflected and part of the wave is transmitted (Jensen et al., 2011).

2.1.3 Intensity

Intensity is the averaged sound energy rate which passes through a unit area normal to the direction of propagation. Intensity can be described by the following Equation (2.2) (Jensen et al., 2011).

$$I = \frac{p_{rms}^2}{\rho c} = \frac{p_{rms}^2}{Z} \tag{2.2}$$

Where, ρ is the density, c is the speed of sound and p_{rms} is the root mean square of the pressure calculated by the following Equation (2.3).

$$p_{rms} = \sqrt{\frac{1}{T}\int_{t1}^{t2} p^2(t)\ dt} \tag{2.3}$$

2.1.4 Decibel and level quantities

An explanation of level quantities is given prior to the defining the most used acoustic quantities. Level quantities are given in the unit of decibel due to the generally large dynamic ranges which are associated with acoustic pressures. One decibel represents the ratio of two values inside a base 10 logarithm where the ratio of these values is equal to 10, multiplied by a factor 10 (A. Thompson & Taylor, 2008). The term level implies the use of a decibel scale (Chapman & Ellis, 1998). Thus, if for example $I_1 = 10I_2$, then the intensity level is given by the following formula.

$$L = 10\log_{10}\left(\frac{I_1}{I_2}\right) = 10\text{ dB} \tag{2.4}$$

From Equation (2.4) it can be seen that an increase of I_1 by a factor 10 represents 20 dB and an increase of I_1 by a factor 100 represents 30 dB. Often level quantities are given with respect to a reference intensity or pressure, in this case represented by I_2 (Bellmann et al., 2020).

2.1.5 Sound exposure level

Exposure (E) represents the integral over a certain time period of the squared sound pressure. Equation (2.5) describes the exposure where $p(t)$ is the pressure signal over time.

$$E = \int_{t_1}^{t_2} p^2(t)\ dt \tag{2.5}$$

A common quantity in underwater acoustics is the sound exposure level (SEL). This quantity takes into account both sound intensity as well as the duration (Martin et al., 2019). The SEL is represented by 10 times the base 10 logarithm of the exposure over the reference exposure and is described by Equation (2.6). The reference pressure is given by p_0. The common reference pressure in water is 1 μPa (Bellmann et al., 2020). As a result, $E_0 = p_0^2 = 1 \cdot 10^{-12}$.

$$SEL = 10 \log_{10} \left(\frac{E}{E_0} \right) = 10 \log_{10} \left(\frac{1}{T_0} \int_{t_1}^{t_2} \frac{p^2(t)}{p_0^2}\ dt \right) \text{ dB re 1 } \mu\text{Pa}^2\text{s} \tag{2.6}$$

2.1.6 Peak pressure level

Another common used acoustic quantity is the peak pressure level ($\mathrm{L_{p,pk}}$). Equation (2.7) represents the formula for the level of the ratio between the absolute maximum sound pressure in a time signal ($|p_{p,k}|$) and the reference pressure (p_0). The visual representation of $|p_{p,k}|$ is depicted in Figure 2.1.

$$L_{p,pk} = 10 \log_{10} \left(\frac{|p_{p,k}|}{p_0} \right) \text{ dB re 1 } \mu\text{Pa} \tag{2.7}$$

2.2 Sound propagation and mitigation

This section focuses on the structure-borne noise generated during pile driving where the pile-water-soil interaction is explained in Section 2.2.1. Furthermore, the noise reduction mechanisms of a BBC is described in Section 2.2.2.

2.2.1 Pile-water-soil interaction

Generally, impact hammers are used to drive MPs into the seabed. An impact weight inside the hammer falls onto an anvil at the top of the MP. The blow generated by the impact falling onto the anvil is transferred through the anvil to the MP driving the MP into the soil (Klages et al., 2019). Furthermore, this blow causes a downward propagating compression wave with a wave speed c_p driving the MP into the seabed (Kuhn et al., 2014; Reinhall & Dahl, 2011). The function for the wave speed is given in Equation (2.8) where E is the modulus of elasticity and ρ is the density (Kuhn et al., 2014).

$$c_p = \sqrt{\frac{E}{\rho}} \tag{2.8}$$

As a consequence of Poisson's effect, the downward propagating compression wave has an associated radial expansion wave (Kuhn et al., 2014). This structural wave is depicted in Figure 2.2.

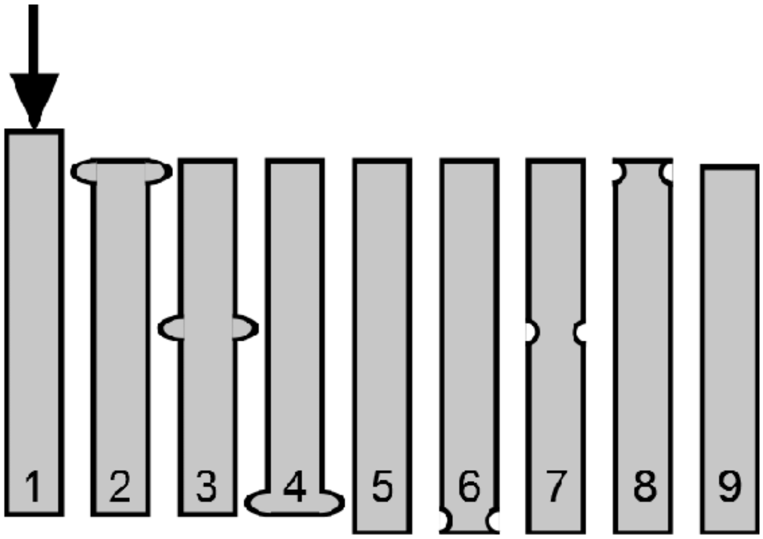

Figure 2.2: Downward propagating structural wave caused by a single blow (Kuhn et al., 2014).

The longitudinal wave speed of the radial expansion wave is faster than the speed of sound in water causing a compression wave field in the form of a Mach cone under an angle in the surrounding water column. The angle of the compression wave field concerning the direction of propagation can be calculated via Snell's law. This is given by Equation (2.9) where c_w is the speed of sound in water and c_p is the speed of the downward propagating structural wave (Reinhall & Dahl, 2011).

$$\phi_w = \sin^{-1}\left(\frac{c_w}{c_p}\right) \tag{2.9}$$

When the structural wave reaches the soil domain the same Mach cone shaped compression wave fields can be observed in the soil, however under a different angle, due to a difference in sound speeds between water and soil causing refraction and reflection of the compression wave field (Reinhall & Dahl, 2011). The angle of the refracted compressional wave can be calculated in the same manner as before using Equation (2.9).

$$\phi_s = \sin^{-1}\left(\frac{c_s}{c_p}\right) \tag{2.10}$$

At the pile toe the downward propagating structural wave will reflect due to an impedance mismatch between the steel and the soil. This wave will travel upwards as a tension wave and an associated radial rarefaction wave, the latter creating a compression wave field in the soil in the form of Mach cones moving upwards and under an angle ϕ_s (Reinhall & Dahl, 2011).

Once this upward propagating compression wave field reaches the soil-water boundary, an impedance mismatch between the soil and water causes the wave to reflect and refract. The angle of reflection and refraction can be determined based on Snell's law (Jensen et al., 2011). Figure 2.3 shows the compression wave fields associated with the downward radial expansion wave and the upward radial rarefaction wave. Note that Figure 2.3 only shows the refracted part (with angle ϕ_{ws}) of the upward moving compression wave in the water and not the reflected part.

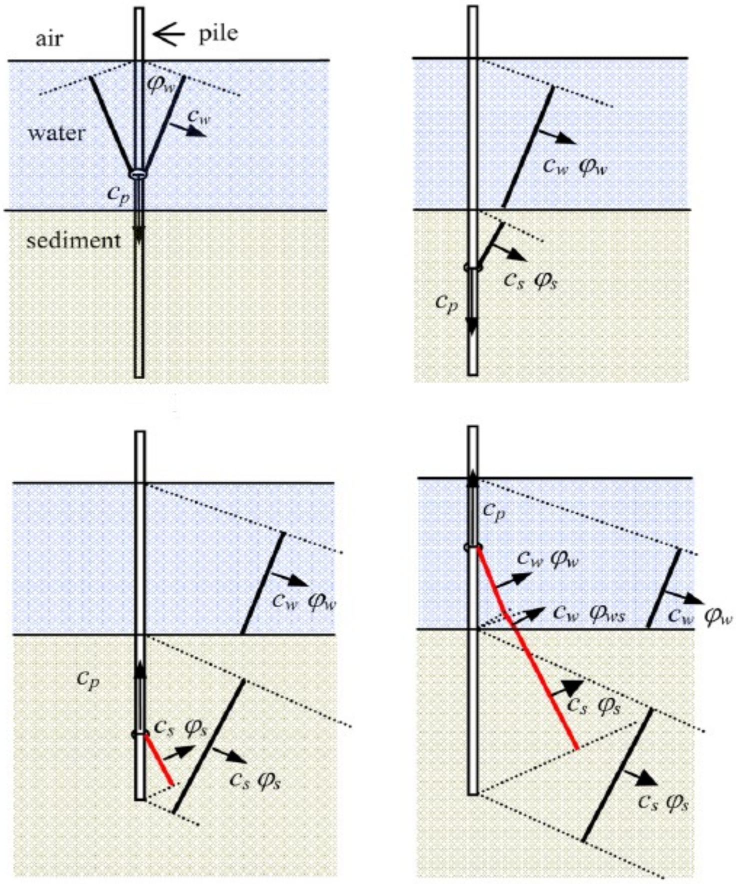

Figure 2.3: Mach cone wave propagating in the soil-water domain under an angle (Reinhall & Dahl, 2011).

At the pile toe compression waves are also generated due to the downward movement of the MP. Along with the compression waves, shear waves are radiated into the soil as an effect of the pile-soil interaction (Fricke & Rolfes, 2015). Shear waves can be divided into vertical shear waves (SV) and horizontal shear waves (SH). Tsouvalas (2015) showed that the radiated shear waves have a dominant vertical polarisation due to a significant difference between the shear wave speed in the soil and the structural wave speed in the MP.

Besides the above mentioned body waves, interface waves are generated due to the impact pile driving (Tsouvalas, 2015). Interface waves generated during offshore pile driving are either Scholte waves travelling along a solid-fluid boundary or Stoneley waves travelling along a solid-solid interface (Meegan et al., 1999). In contrast to body waves, which radiate spherically, interface waves spread cylindrically and decay therefore less rapidly over distance (Meegan et al., 1999). The influence of Scholte waves travelling along the soil-water boundary is significant for pressure fluctuations in the water column near the seabed. This influence becomes less significant further away from the seabed (Tsouvalas, 2015).

2.2.2 Mitigation by a BBC

The benefits of using an air bubble curtain with percussive pile driving was shown by Würsig et al. (2000) where the emitted sound waves were measured at distances of 250, 500 and 1000 meters from the pile. The results showed a reduction of around 5 dB of the broadband pulse level. Bellmann (2014) showed that the noise reduction by BBC varies for different frequencies. In general, there is an increase in reduction visible for frequencies up to 1250 Hz, after which the reduction decreases for frequencies higher than 1250 Hz. The main attenuation of noise by a BBC is ascribed to an impedance mismatch within the water due to the air bubbles. This leads to partial reflection of the sound waves back into the domain between the MP and the BBC (Peng et al., 2021b). Furthermore, Göttsche et al. (2013) describes that the vibration of air bubbles due to the waves passing through leads to absorption of noise. However, this vibration is only induced by high frequencies which lie outside the frequency spectrum associated with pile driving of large-size MPs (Tsouvalas, 2020).

2.3 Influencing factors for sound propagation and mitigation

This section focuses on the parameters of influence regarding pile driving noise. For the application of the BBC it is of importance to have an understanding about these parameters to reduce the noise during the construction works (Bellmann et al., 2020). First, the technical-constructive influencing factors will be discussed (2.3.1). Second, the site-specific characteristics will be elaborated (2.3.2). This distinction between characteristics is based on the work of Bellmann et al. (2020). Lastly, the influencing factors of the BBC are described (2.3.3).

2.3.1 Technical-constructive influencing factors

For this thesis the focus lies on MP foundations. The most important factor with respect to noise regarding MP design is the chosen pile diameter (Bellmann et al., 2020). Figure 2.4 shows the relation between pile diameter and corresponding SEL and $L_{p,pk}$. It can be seen that the noise levels increase for increasing pile diameter.

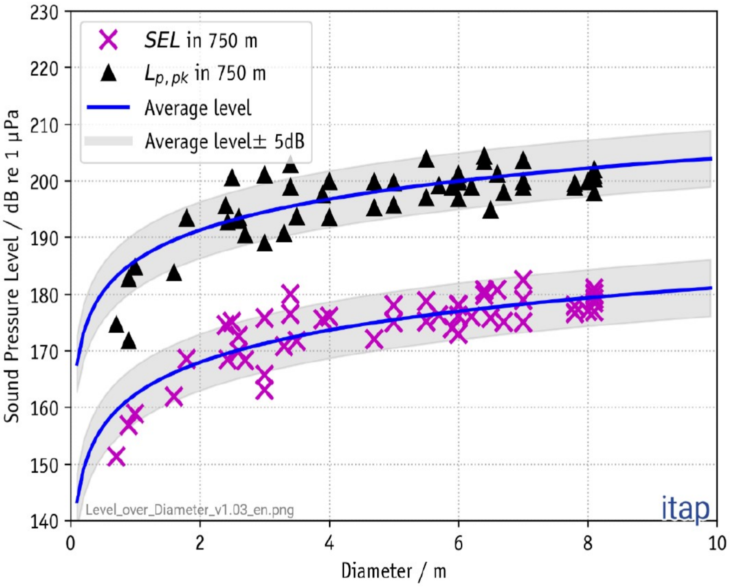

Figure 2.4: Plot of SEL and $L_{p,pk}$ against the pile diameter (Bellmann et al., 2020).

As the diameter of the MP increases the size of the hammer needs to increase as well as the used blow energy (Bellmann et al., 2020). The blow energy has to increase due to the increasing soil resistance as an effect of larger MP diameters (Kong et al., 2020).

For larger MPs (>6 m) the maximum in the frequency spectrum shifts from approximately 160 Hz to 100 Hz (Bellmann et al., 2020). This shift cannot be attributed to either the pile diameter or the size of the hammer. It can be assumed that the used blow energy, the pile diameter and the size of the hammer are strongly correlated (Bellmann et al., 2020).

2.3.2 Site-specific influencing factors

2.3.2.1 Soil parameters and -layering

The structure and characteristics of ocean bottoms is of significant importance when sound interacts with the seafloor (Jensen et al., 2011). Marine sediments are often modelled as an equivalent fluid which means that they only support only compressional sound waves. However, according to Hamilton (1980), all marine sediments possess enough shear rigidity to transfer shear waves. This is of importance as compression waves can also be partially converted into shear waves, Scholte waves which travel along the soil-fluid interface and Stoneley which travel along soil-soil interfaces. A proper detailing of the true thicknesses and properties of the ocean bottom is called a geoacoustic model (Hamilton, 1980). A complete geoacoustic model contains the following material properties: the compressional wave speed c_p, the shear wave speed c_s, the compressional wave attenuation α_p, the shear wave attenuation α_s and the density ρ (Jensen et al., 2011).

In most cases, underwater sound waves encounter two types of interfaces: fluid-soil interfaces and soil-soil interfaces. An impedance mismatch (see Section 2.1.2) between the fluid-soil and soil-soil interfaces causes the wave to partly reflect back up and partly transmit deeper into the ocean bottom. Figure 2.5 shows an example of an incident wave being partly reflected and partly transmitted by an interface,

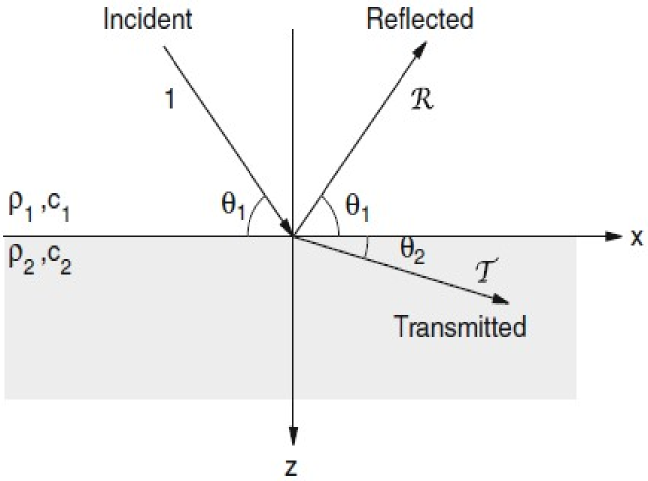

Figure 2.5: Incident wave reflected and transmitted (Jensen et al., 2011)

where the amplitude of the transmitted wave is given by Equation (2.11) (Jensen et al., 2011).

$$1 + \mathcal{R} = \mathcal{T} \tag{2.11}$$

The amplitude of the reflected- and the transmitted wave are given in terms of effective impedance which is defined as

$$\mathcal{Z}_i = \frac{\rho_i c_i}{\sin \theta_i}. \tag{2.12}$$

For the case of fluid-soil or soil-soil interfaces where the soil contains shear rigidity, the amplitude coefficient of the reflected wave is given in terms of the total effective impedance accounting for both the compressional wave speed as well as the shear wave speed (Jensen et al., 2011),

$$\mathcal{R} = \frac{\mathcal{Z}_{tot} - \mathcal{Z}_1}{\mathcal{Z}_{tot} + \mathcal{Z}_1}, \tag{2.13}$$

and the amplitude coefficient of the transmitted wave is given by

$$\mathcal{T} = \frac{2\mathcal{Z}_{tot}}{\mathcal{Z}_{tot} + \mathcal{Z}_1}, \tag{2.14}$$

where the total effective impedance $\mathcal{Z}_{tot}$ is given as

$$\mathcal{Z}_{tot} = \mathcal{Z}_p \cos^2(2\theta_s) + \mathcal{Z}_s \sin^2(2\theta_s). \tag{2.15}$$

This means that for increasing mismatch in impedance, the amplitudes of both the reflected- and transmitted wave increase as well. The soil parameters responsible for the effective impedance are the density ρ and the compressional and shear wave speed c_p and c_s. For a layered structure of the ocean bottom, the travelling sound wave encounters numerous soil-soil interfaces each reflecting and transmitting the sound wave. As a result of these reflections and transmissions, energy radiates back from the soil domain to the fluid domain at some distance from the MP. Figure 2.6 shows an example of a sound wave with multiple reflections and transmissions. The arrows in the figure represent sound waves. The sound waves with amplitudes $\mathcal{T}_{12}\mathcal{R}_{23}\mathcal{T}_{21}$ and $\mathcal{T}_{12}\mathcal{R}_{23}^{2}\mathcal{R}_{21}\mathcal{T}_{21}$ are examples of sound waves leaking back into the fluid domain from the soil domain.

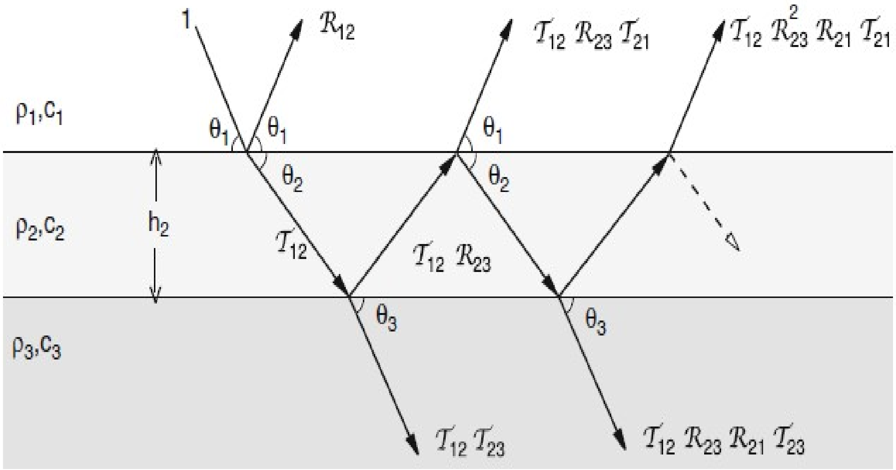

Figure 2.6: Multiple reflections and transmissions due to a layered structure of the ocean bottom (Jensen et al., 2011).

Tsouvalas (2015) showed that the geoacoustic model plays an important role in the noise prediction due to elastic waves travelling through the medium or on the boundaries. The shear rigidity of the soil is of great influence on the penetration depth of the Scholte waves in the water column close to the seabed (Tsouvalas, 2015). The larger the penetration depth of the Scholte waves, the higher the noise levels in the vicinity of the seabed (Tsouvalas, 2015). Although layering of the soil is important for the sound propagation, the properties and the depth of the upper layer mainly govern the noise levels (Tsouvalas, 2015).

2.3.2.2 Influence of the water depth

The main influence of the water depth can be attributed to the corresponding cut-off frequency. The cut-off frequency is the frequency below which no energy can propagate through the waveguide (Jensen et al., 2011). Depending on the sediment type, this cut-off frequency is below 50 Hz for water depths of approximately 25 meters (Bellmann et al., 2020). Offshore pile driving happens most often in shallow waters with the most dominant frequencies lying between 63 and 250 Hz (Bellmann et al., 2020).

2.3.2.3 Bathymetry

Bathymetry can play a significant role in the sound propagation over long ranges, however the sea can often be modelled as a flat surface for sound prediction over shorter ranges up to a few kilometers (T. Lippert et al., 2018). According to Scheckl-man et al. (2015) the average water depth is the main influencing factor for sound propagation over long ranges whereas variations in bathymetry cause merely localized effects.

2.3.3 BBC influencing factors

The main influencing factors for the noise mitigation effectiveness of a BBC are the used air volume (air fraction in the water), nozzle size, nozzle spacing, water depth (static pressure) and the currents (Bellmann et al., 2020; Bohne et al., 2019; Peng et al., 2021b). According to Bellmann et al. (2020) the air volume plays a significant role for the impedance difference between the seawater and the air-water mixture. The nozzle size and therefore bubble size is also of great influence and it is shown that a densely distributed air bubble curtain with small size bubbles has the best sound mitigation effect (Rustemeier et al., 2012).

2.4 Predicting sound propagation and mitigation

This section gives an overview of the available models for the prediction of sound propagation and mitigation. A distinction is made between first generation models (2.4.1), second generation models (2.4.2) and the state-of-the-art (2.4.3) based on the work of Tsouvalas (2020). Furthermore, an overview of air bubble curtain models are discussed in Section 2.4.4.

2.4.1 First generation models

Reinhall and Dahl (2011) were the first to develop a numerical model focusing on the prediction of noise propagation due to impact pile driving (Tsouvalas, 2020). It comprises a finite element (FE) model of the pile and a cylindrical water and soil domain in the vicinity of the pile. (Reinhall & Dahl, 2011). To model the sound propagation further away from the pile, the parabolic equation method is adopted in combination with perfectly matched boundary conditions truncating the FE domain (Reinhall & Dahl, 2011). In this study it is shown that the impact from the hammer onto the MP generates a radial expansion wave along the axial direction of the pile. As this wave propagates downward with supersonic speed the radial expansion causes compression waves in the form of a Mach cone wave under a certain angle radiated into the water column.

S. Lippert et al. (2013) also uses the idea of Reinhall and Dahl (2011) of an FE domain to model the pile and a soil-water region in the vicinity of the pile. However, in contrast to Reinhall and Dahl (2011), for the far field model S. Lippert et al. (2013) makes use of the wave number integration method.

In contrast to the numerical models described above, semi-analytical models were also developed to describe the propagation of underwater noise generated by offshore pile driving. Tsouvalas and Metrikine (2013) introduce a semi-analytical model where the hammer, the pile, the soil and the water are presented as a coupled problem. The hammer is represented by a time-force curve, the pile is described by thin shell theory based on the work of Kaplunov et al. (2012), the soil is represented by spring-dashpot systems in all directions and the water is described by a linear acoustic medium (Tsouvalas & Metrikine, 2013). The coupled problem is then solved in terms of modes using a mode matching technique. One advantage of the semi-analytical models as opposed to the numerical FE models is the increase in computational efficiency (Tsouvalas & Metrikine, 2013).

2.4.2 Second generation models

Pile driving sources in elastic media, such as soil, emit both compressional, shear and Scholte waves (Nealy et al., 2016; Peng et al., 2021b). The main limitation of the first generation models is that the latter two cannot be captured, because the seabed is described either as an acoustic medium or is represented by a spring-dashpot configuration (Tsouvalas, 2020). To overcome this problem Tsouvalas (2015) modelled the seabed as a three-dimensional elastic continuum. In Figure 2.7 the shear waves can be seen with a almost vertical inclination to the horizontal. Also, the effect of the Scholte waves can be seen in the fluid zone in the vicinity of the seabed.

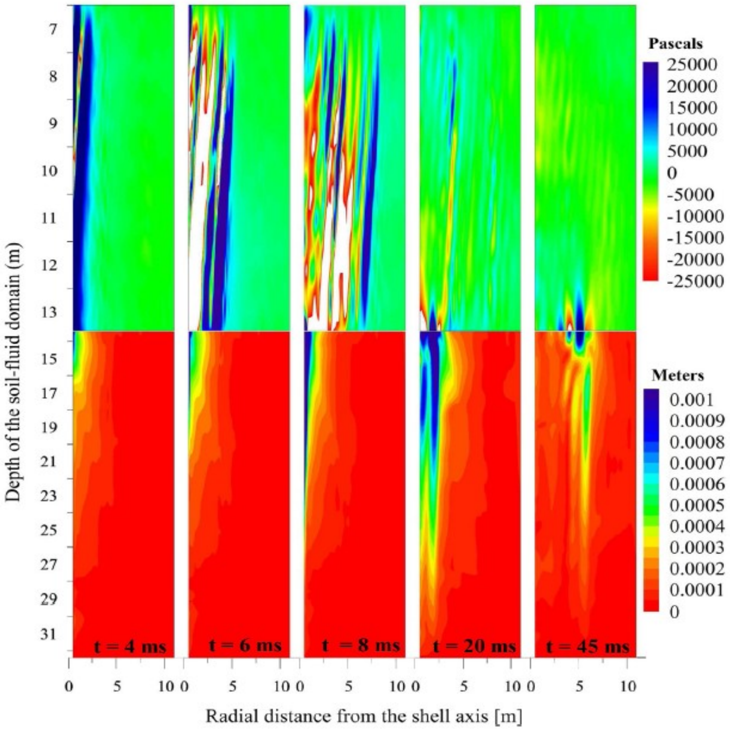

Figure 2.7: Representation of the compression wave field in the water domain and of the shear and Scholte waves in the soil domain (Tsouvalas & Metrikine, 2014).

2.4.3 State-of-the-art

Despite a plethora of state-of-the-art numerical models described in Tsouvalas (2020), this thesis will focus on the semi-analytical model referred to as SILENCE developed by Tsouvalas et al. (2019). SILENCE makes use of two modules for the prediction of noise propagation, a near field module or sound generation module and a far-from-source module or sound propagation module, which are coupled by a boundary integral at the interface. High-order shell theory are used for the description of the MP (Kaplunov et al., 2012). The soil is modelled as a three-dimensional elastic continuum and the entire coupled problem is solved in the frequency domain (Tsouvalas, 2020). Peng et al. (2021a) improved the model making it computationally more efficient, flexible and accurate as a result of using a direct boundary integral method and a more detailed description of the ring source in the soil domain.

2.4.4 Air bubble curtain models

Tsouvalas and Metrikine (2016) were among the first to implement an air bubble curtain underwater in sound propagation modelling software. The way this was done was by modelling the air bubble curtain as a frequency-dependent homogeneous medium. The bubbles are assumed to have a perfect vertical rise pattern from the seabed to the sea surface not drifting away by currents (Tsouvalas & Metrikine, 2016). S. Lippert et al. (2017) integrated two non-reflection perfectly absorbing surfaces surrounding the pile representing the sound attenuation of a double big bubble curtain (DBBC). Another method of modelling the air bubble curtain was developed by Bohne et al. (2019). In this study a more accurate description of the air bubble curtain model was given based on the local distribution of the effective wavenumber which depends partially on a probalistic distribution of the bubble sizes, the local air fraction and the mean bubble volume. Figure 2.8 shows the assumed Gaussian distribution of the local air fraction and the vertical liquid velocity.

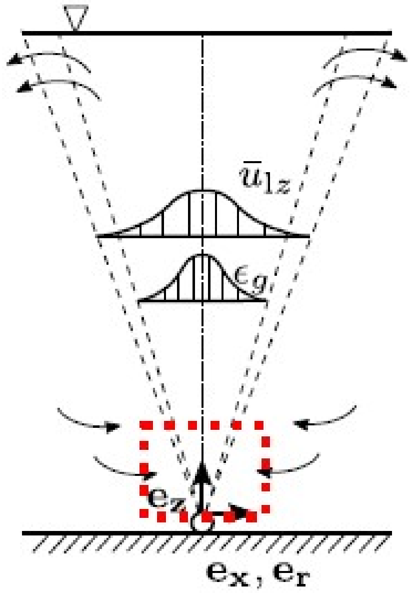

Figure 2.8: Local air fraction and vertical liquid velocity distribution according to Bohne et al. (2019, 2020).

A frequency- and depth dependent transmission coefficient for the amplitude of the transmitted wave was derived after which the transmission loss of the air bubble curtain is determined. A more detailed elaboration on the determination of the transfer coefficient function is given in Section 3.1. This transfer coefficient takes into account real BBC parameters such as nozzle size, air flow rate and water depth (Bohne et al., 2019). An improvement of the work of Bohne et al. (2019) was developed by the same author describing the bubble formation process above the nozzle of the air supply hose more accurately (Bohne et al., 2020). The enclosed red dotted region in Figure 2.8 shows the region of focus from Bohne et al. (2020). The model from Peng et al. (2021b) presents a computationally efficient model which implements the air bubble curtain in the noise prediction model for offshore pile driving. The model comprises a near field or sound generation module and a far field or sound propagation module. At the boundary between these modules the noise attenuation module represents the bubble curtain by means of a transfer function based on the work of Bohne et al. (2020) (Peng et al., 2021b). Due to computational efficiency the model can function well for parametric and sensitivity analyses of both the pile system and the air bubble curtain system separately as well as a combination of both (Peng et al., 2021b).

Chapter 3

Modelling the mitigation of noise

This chapter describes the modelling of noise mitigation by SILENCE BUBBLES. The air bubble curtain model (Bohne et al., 2020) which is integrated in SILENCE BUBBLES as the sound reduction module is described in Section 3.1. A detailed elaboration of the sound generation and propagation module of SILENCE are omitted in this chapter for sake of brevity and can be found in Appendix A. The predicted sound field by SILENCE is validated in Section 3.2. Section 3.3 describes the determination of the BBC parameters which are used for the sensitivity study.

3.1 Sound reduction module

Figure 3.1 shows the complete coupled model with the sound generation, sound reduction and sound propagation module.

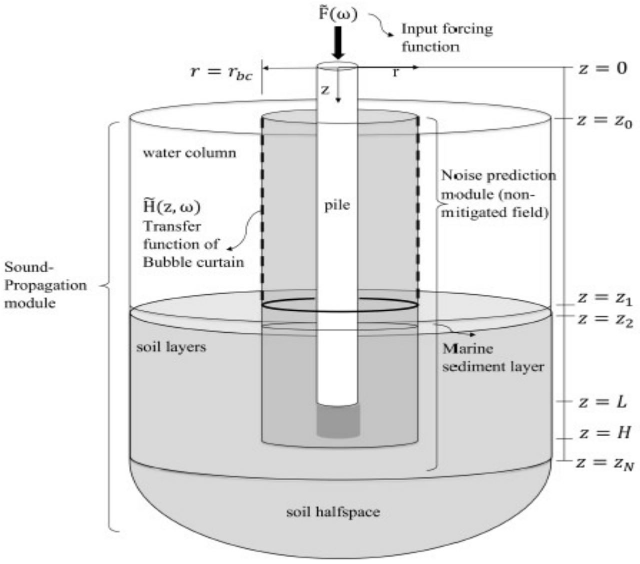

Figure 3.1: Complete coupled model with sound generation, sound reduction and sound propagation module (Peng et al., 2021a).

3.1.1 Local effective wavenumber distribution

Bohne et al. (2019) developed an air bubble curtain model comprising of a distribution of local effective wavenumbers to account for the acoustic interaction between air bubbles and incoming sound waves. The local effective wavenumber distribution is given by Equation 3.1 (Commander & Prosperetti, 1989).

$$k_{eff}^2(\omega, r, z) = \frac{\omega^2}{c_f^2} + 4\pi\omega^2 \int_0^\infty \frac{an(\mathbf{u}, r, z, a)}{\omega_0^2(z, a) - \omega^2 + 2i\beta(z, a)\omega} \mathrm{d}a, \tag{3.1}$$

where ω is the angular frequency given by $2\pi f$, c_f is the wavespeed in the fluid and a is the bubble radius. The unknown local bubble number density distribution $n(\mathbf{u}, r, z, a)$ is obtained by solving the fluid dynamic model of the air bubble curtain. The natural angular frequency $\omega_0(z, a)$ is defined by Commander and Prosperetti (1989) and the damping constant $\beta(z, a)$ of the linear bubble response by Kargl (2002) and are given as follows,

$$\omega_0 = \sqrt{\frac{p_0(z)}{\rho_f a^2}\left(3 - \frac{2\sigma}{p_0(z)a}\right)}, \tag{3.2}$$

$$\beta(z, a) = \frac{(\gamma_0 - 1)p_0(z)}{10\gamma_0\rho_f D} + \frac{2\mu}{\rho_f a^2}, \tag{3.3}$$

where $\sigma = 0.073$ N/m is the surface tension of the water, $\gamma_0 = 1.41$ represents the ratio of specific heats, $D = 1.9 \times 10^{-5}$ m^2/s is the gas thermal diffusivity and $\mu = 10^{-3}\mathrm{N} \cdot \mathrm{s/m}^2$ denotes the viscosity of the fluid (Peng et al., 2021b).

3.1.1.1 Fluid dynamic model of the air bubble curtain

The effective wavenumber distribution is based on a fluid dynamic model of rising bubbles in which the typical working fluid is air. Air comes out of the nozzles generating bubbles which in turn generate a buoyancy force dragging the surrounding liquid upwards (Bohne et al., 2020). The flow pattern of the bubbles can be subdivided into four regions. These four regions are depicted in Figure 3.2.

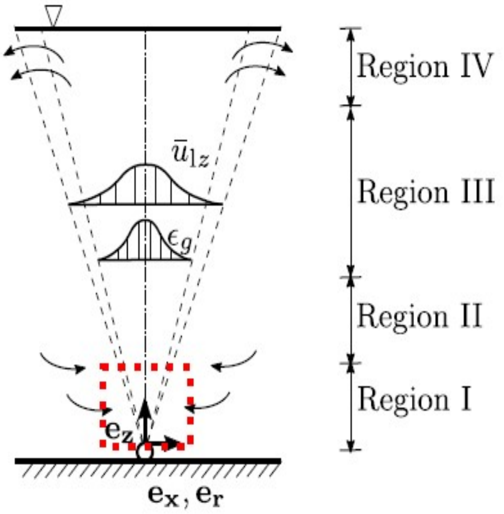

Figure 3.2: Flow pattern of the air bubble curtain with four regions (Bohne et al., 2020).

Region I describes the formation process of the bubbles with axisymmetric flow. Region II is stated as the transition regime where adjacent nozzles merge. In Region III the flow becomes symmetrical with respect to the y-direction and Region IV is mainly governed by the return flow and the surface waves (Bohne et al., 2020). The model introduced by Bohne et al. (2020) focused on a realistic approximation of the bubble formation process based on merging buoyant plumes. The bubble formation process is then later integrated over the entire water domain similar to the approach of Bohne et al. (2019). To solve the unknown bubble number density distribution $n(\mathbf{u}, r, z, a)$ the following partial differential equations are used where Equation (3.4) describes the momentum of balance for the gas-liquid mixture with high local gas fraction. Subsequently, the conservation of mass of the liquid phase is given by Equation (3.5) and lastly, Equation (3.6) represents the evolution of the bubble sizes in a turbulent bubbly flow outlined by the population balance equation (Bohne et al., 2020).

$$\nabla \cdot \left(\varepsilon_f \rho_f \bar{\mathbf{u}}_f \times \bar{\mathbf{u}}_f + \varepsilon_f \rho_f \overline{\delta \mathbf{u}_f \times \delta \mathbf{u}_f} \right) = \varepsilon_g \rho_g g \tag{3.4}$$

$$\nabla \cdot \left(\varepsilon_f \rho_f \bar{\mathbf{u}}_f \right) = 0 \tag{3.5}$$

$$\begin{aligned} \frac{\partial n(v_p)}{\partial t} + \nabla \cdot (n(v_p)\mathbf{u}_g) = \int_{v_p}^{\infty} r_1(v_p, v_q) n(v_q) \mathrm{d}v_q - \int_0^{v_p} \frac{n(v_q)}{v_p} v_q r_1(v_p, v_q) \mathrm{d}v_q + \\ \frac{1}{2} \int_{v_p}^{\infty} r_2(v_p, v_p - v_q) n(v') n(v_p - v_q) \mathrm{d}v_q - \int_{v_p}^{\infty} r_2(v_p, v_p - v_q') n(v_q) n(v_p) \mathrm{d}v_q \end{aligned} \tag{3.6}$$

For a complete derivation of these equations and how these equations are rewritten into Equation (3.7), the reader is referred to Bohne et al. (2020).

$$\frac{\mathrm{d}}{\mathrm{d}z} (\mathbf{m}(\mathbf{u}, z)) = \mathbf{q}(\mathbf{u}, z) \tag{3.7}$$

In Equation (3.7), the vector $\mathbf{u} = \left[u_{lzm}, b, \varepsilon_{gm1}, \varepsilon_{gm2}, \bar{v}_1, \bar{v}_2 \right]^T$ represents the vector of six unknowns where u_{lzm} is the centerline velocity, b is the half width of the air bubble curtain, ε_{gm1} and ε_{gm2} are the gas fractions of the small and large bubble, respectively, and $\bar{v}_{10}$ and $\bar{v}_{20}$ are the arithmetic mean bubble volumes of the small and large bubbles, respectively. Equation (3.7) is solved for $\mathbf{u}$ using a Forward Euler scheme making use of the following initial conditions.

$$u_{lzm0} = \sqrt{\frac{-2M_0(2\lambda^2 + 1)}{\gamma b_0^2 \rho_f \pi \left(2\varepsilon_{gm10}\lambda^2 + 2\varepsilon_{gm20}\lambda^2 - 2\lambda^2 - 1 \right)}} \tag{3.8}$$

$$b_0 = \sqrt{\frac{\dot{m}_0(\lambda^2 + 1)}{\lambda^2 \pi \rho_{g0} (\lambda^2 + 1)(\varepsilon_{gm10} u_{rel1}(\bar{v}_{10}) + \varepsilon_{gm20} u_{rel2}(\bar{v}_{20})) + \lambda^2 u_{lzm0} \pi \rho_{g0} (\varepsilon_{gm10} + \varepsilon_{gm20})}} \tag{3.9}$$

$$\varepsilon_{gm10} = 0.005 \tag{3.10}$$

$$\varepsilon_{gm20} = 0.495 \tag{3.11}$$

$$\bar{v}_{20} = \frac{4}{3}\pi(1.1447a_{prim})^3 \tag{3.12}$$

$$\bar{v}_{10} = \frac{\bar{v}_{20}}{30} \tag{3.13}$$

Once the vector $\mathbf{u}$ is known, the bubble number density distribution can be obtained. First, $n(\mathbf{u}, r, z, a)$ is subdivided into two parts where one part represents the small bubble fraction $n_1(\mathbf{u}, r, z, a)$ approximated by a lognormal distribution and the other part represents the large bubble fraction $n_2(\mathbf{u}, r, z, a)$ approximated by an exponential distribution as shown by Equations (3.14 - 3.16) (Bohne et al., 2020).

$$n(\mathbf{u}, r, z, a) = n_1(\mathbf{u}, r, z, a) + n_2(\mathbf{u}, r, z, a) \tag{3.14}$$

$$n_1(\mathbf{u}, r, z, a) = \frac{\varepsilon_{g1}(r, z)}{\bar{v}_1^2}\frac{2}{\pi}\frac{\bar{v}_1}{3v(a)}\exp\Bigg(-\frac{2}{9}\ln\left(\frac{v(a)}{\bar{v}_1}e^{\frac{9}{8}}\right)\Bigg), \tag{3.15}$$

$$n_2(\mathbf{u}, r, z, a) = \frac{\varepsilon_{g2}(r, z)}{\bar{v}_2^2}\exp\Bigg(-\frac{v(a)}{\bar{v}_2}\Bigg), \tag{3.16}$$

Subsequently, the gas fractions of both the small and large bubbles ε_{gi} are given by Equation (3.17) expressing the gas fractions into the known variables $\varepsilon_{gmi}(z)$ and b.

$$\varepsilon_{gi}(r, z) = \varepsilon_{gmi}(z)\exp\Bigg(-\frac{r^2}{\lambda^2 b^2}\Bigg), \tag{3.17}$$

This expression can be filled into Equations (3.15 & 3.16) solving for $n(\mathbf{u}, r, z, a)$. Subsequently, $n(\mathbf{u}, r, z, a)$ can be filled into Equation (3.1) solving for the effective wavenumber distribution.

3.1.2 Transfer function

Once the distribution of the local effective wavenumbers is known for the air bubble curtain, the transfer function can be determined (Bohne et al., 2019). A simplified approach is adopted assuming an incident plane sound wave field and plane wave propagation within the area of the air bubble curtain (Bohne et al., 2019). Also, it is assumed that for a constant z-coordinate, the air bubble curtain can be discretized into n layers with $n-1$ interfaces and that the incident sound wave only travels through the layer corresponding to that specific z-coordinate meaning $k_{eff}(x, z, \omega) = k_{eff}(x, \omega)$. A schematic representation of the discretized air bubble curtain is depicted in Figure 3.3.

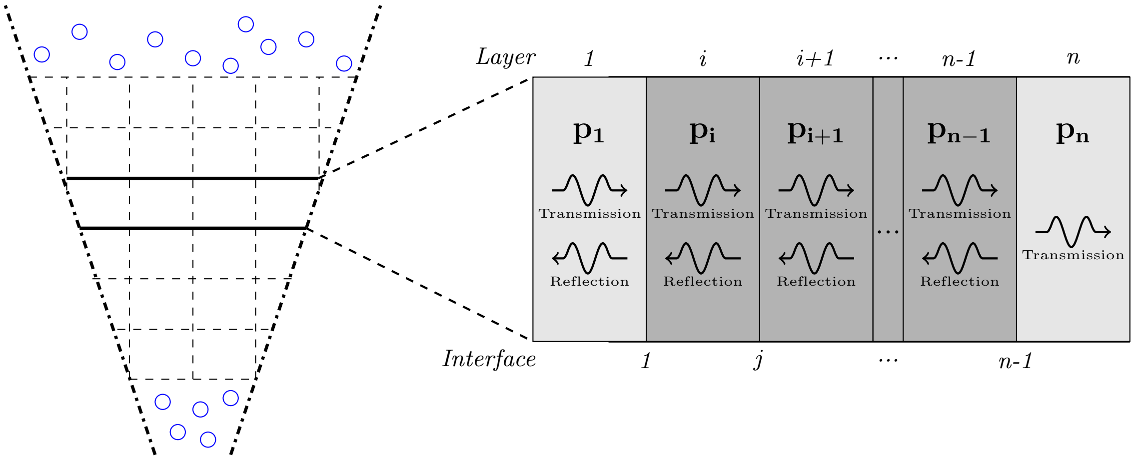

Figure 3.3: Schematic representation of the discretized air bubble curtain.

The incident sound wave travelling through the triangular shaped air bubble curtain is depicted left in the figure. A more detailed view of a horizontal layer i of the discretized air bubble curtain is depicted on the right where a the travelling sound wave encountering interfaces is schematized. The sound pressure and sound velocity in layer i are given by Equations (3.18 & 3.19), respectively.

$$P_i(x,\omega) = p_i^- e^{ik_i x} + p_i^+ e^{-ik_i x} \tag{3.18}$$

$$v_i(x,\omega) = \frac{k_i}{\omega \rho_i}\left(p_i^+ e^{-ik_i x} - p_i^- e^{ik_i x}\right) \tag{3.19}$$

At layer interface j the continuity conditions for the sound pressure and velocity have to be fulfilled (Commander & Prosperetti, 1989).

$$P_i(x_j,\omega) = P_{i+1}(x_j,\omega) \ \wedge \ v_i(x_j,\omega) = v_{i+1}(x_j,\omega) \tag{3.20}$$

For each interface j this leads to a set of two equations with two unknowns which are set equal to each other where the vector $\left[p_{i+1}^+, p_{i+1}^-\right]^T$ can be expressed in terms of the vector $\left[p_i^+, p_i^-\right]^T$ by means of the dot product of the inverse of matrix $\mathbf{A_{i+1}}$ with matrix $\mathbf{A_i}$.

$$\left(\mathbf{A_{i+1}}\right)^{-1} \cdot \mathbf{A_i} \cdot \mathbf{p_i} = \mathbf{p_{i+1}} \tag{3.21}$$

Repeating this for all interfaces yields a system of equations given in Equation (3.22). Assuming an incoming sound wave with an amplitude of $p_1^+ = 1$ and radiation conditions defining $p_n^- = 0$, the resulting set of equations becomes

$$\mathbf{A} \cdot \mathbf{p_1} = \mathbf{p_n}. \tag{3.22}$$

The amplitude of the reflected wave then yields

$$p_1^- = -\frac{a_{21}}{a_{22}} \tag{3.23}$$

and the amplitude of the transmitted wave is

$$p_n^+ = a_{11} + a_{12} p_1^-. \tag{3.24}$$

The complex transfer function is then defined by Peng et al. (2021a) as

$$\tilde{H}(z,\omega) = p_n^+. \tag{3.25}$$

This complex transfer function is coupled to SILENCE through a boundary integral equation. For a detailed derivation of the boundary integral equation, the reader is referred to Peng et al. (2021a). The transmission coefficient for the air bubble curtain over depth is defined by Bohne et al. (2020) as follows,

$$\tau_{\mathrm{BC}}(\omega) = \sum_{l=1}^{m} \tau_l \frac{\Delta z_l}{T}, \tag{3.26}$$

where $\tau_l = |p_n^+|^2$, Δz_l is the stepsize over the depth and T is the depth. The transmission loss of the air bubble curtain as a function of ω in logarithmic form is given by Equation 3.27. Figure 3.4 shows an example transmission loss function.

$$\mathrm{TL} = 10 \log \left(\frac{1}{\tau_{\mathrm{BC}}} \right). \tag{3.27}$$

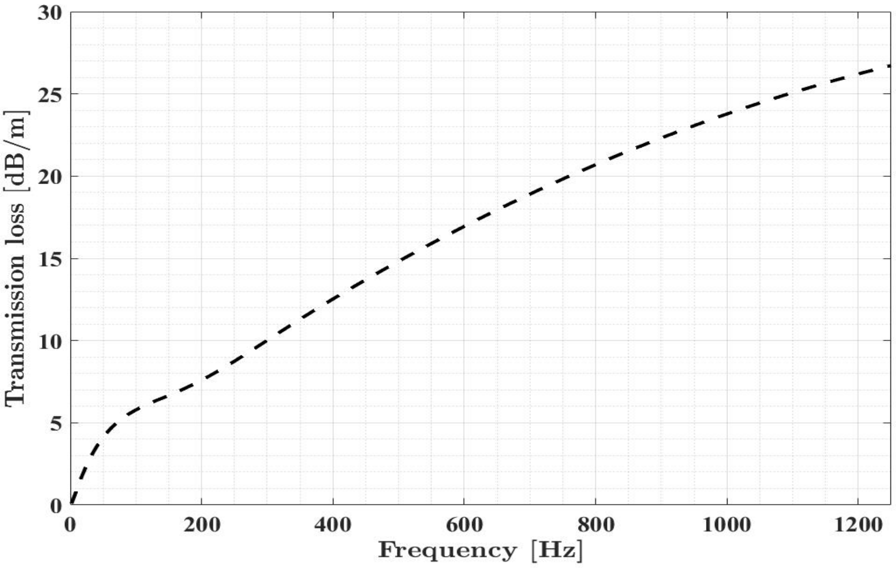

Figure 3.4: Transmission loss function for the air bubble curtain model.

3.2 Validation of SILENCE

In order to substantiate the correctness of the output of SILENCE it is validated and the simulated results are compared to actual measurement data made available by Van Oord. Furthermore, the goal of the validation is to check whether assumptions made on soil layering and parameters, hammer force and pile dimensions are sufficient.

3.2.1 Monitoring overview

For the validation, measurement data from the installation of **confidential** OWTGs at **confidential** has been made available by Van Oord. **confidential** MPs were installed with a BBC and **confidential** were installed while testing a new noise mitigation system. At these foundation sites, the following noise mitigation variants were tested and are depicted below in chronological order:

- No noise mitigation system used,
- Use of only the AdBm noise mitigation system,
- Use of both the AdBm and BBC,
- Use of only the BBC.

The fact that the same pile has measurement data available for both the unmitigated- and mitigated case makes the **confidential** piles described above practical for validation of both SILENCE and SILENCE BUBBLES as the technical-constructive and site-specific parameters stay constant. To meet the boundary condition of SILENCE of an assumed flat bathymetry (see Section 1.4), the surrounding bathymetry of the chosen benchmark pile has to be as flat as possible. Taking into account these factors, validation is performed based on the data of **confidential** of the **confidential**. The underwater noise resultant from **confidential** during installation at **confidential** was monitored by surrounding hydrophones placed at radial distances of 750 m and 1500 m from the pile as can be seen in Figure 3.5. The hydrophones measure each individual pressure-time signal as soon as the signal-to-noise ratio is larger than 6 dB.

Figure 3.5: Location of **confidential** and the positions of the surrounding hydrophones.

In Figure 3.5, the MP is marked in the center of the figure. The hydrophones MP1, MP2, MP3 and MP4 are placed at a distance of 750 m from the MP and the hydrophones MP5, MP6, MP7 and MP8 are placed at a distance of 1500 m from the MP. At all hydrophone locations two hydrophones were placed at 2 and 10 meters above the seabed. It is of importance that the sound path from the MP to the hydrophones is uniform in order to meet the assumption of the model as good as possible. Figure 3.6 depicts the surrounding bathymetry around **confidential** up to hydrophones MP1, MP2, MP3 and MP4.

Figure 3.6: Surrounding bathymetry around **confidential** and the locations of hydrophones MP1, MP2, MP3 and MP4.

It can be seen from Figure 3.6 that the bathymetry from the MP to hydrophones

MP1, MP3 and MP4 is in general uniform and that the variations in bathymetry along the sound path are small. MP2 has not been taken into account due to the varying bathymetry close to the MP as a result of the spudcans of the installation vessel.

3.2.2 Input data

Numerical analysis

For the numerical analysis, SILENCE takes two values as input, namely the number of frequency steps (N_f) and the time step size (Δt). The given number of frequency steps are determined by the distance the sound prediction model needs to cover based on the speed of sound in the fluid. In this case, the hydrophones are placed at a distance of 750 meters from the pile so the predicted sound field should be at least up to this distance. It is chosen to predict the sound field up to a distance of 900 meters. Furthermore, according to Bellmann (2014), the BBC shows an increasing reduction of sound levels up to a frequency of about 1 to 2 kHz after which the reduction decreases significantly. As it is computationally-wise not realistic to take into account all frequencies in the analysis it is deemed sufficient to analyse only the most reducible frequencies. Therefore, a maximum frequency (f_{max}) of 1250 Hz is chosen for this analysis. To achieve this maximum frequency, the time step is calculated with $\Delta t = \frac{1}{2f_{max}}$. The maximum time ($t_{max}$) is determined by dividing the covered distance by the sound speed of water and is 0.6 seconds. In this way the number of time steps can be calculated by $N_t = \frac{t_{max}}{\Delta t}$ and the number of frequency steps is then given by $N_f = \frac{N_t}{2}$. The frequency step size is given by $\Delta f = \frac{f_{max}}{N_f}$. A complete overview of the numerical analysis is given in Table 3.1.

Description	**Parameter**	**Value**	**Unit**
Number of frequency steps (input)	N_f	750	-
Time step size (input)	Δt	0.0004	s
Number of time steps	N_t	1500	-
Maximum duration	t_{max}	0.6	s
Maximum frequency	f_{max}	1250	Hz
Frequency step size	Δf	1.6667	Hz

Table 3.1: Numerical parameters for the frequency- and time analysis.

Force input parameters

The hammer force is approximated by a force-time curve as real hammer force data is not available. The force-time curve used in this study is based on the work of Glasbergen (2020) and S. Lippert et al. (2016) and is given by Equation 3.28.

$$F(t) = \begin{cases} 0 & t < t_b \\ \frac{F_p}{t_r}(t - t_b) & t_b \leq t < t_b + t_r \\ F_p e^{-\frac{t-(t_b+t_r)}{td}} & t_b + t_r \leq t < t_e \\ 0 & t \geq t_e \end{cases} \tag{3.28}$$

The force-time curve parameters are chosen such that the force generates almost all of the energy in frequencies up to 1250 Hz. The parameters are given in Table 3.2.

Parameter	**Value**	**Unit**
F_p	20	MN
t_b	0.0012	s
t_r	0.0024	s
t_d	0.002	s
t_e	0.02	s

Table 3.2: Input parameters for the force-time curve.

In Figure 3.7 and 3.8 the forcing function is depicted in the time- and frequency domain.

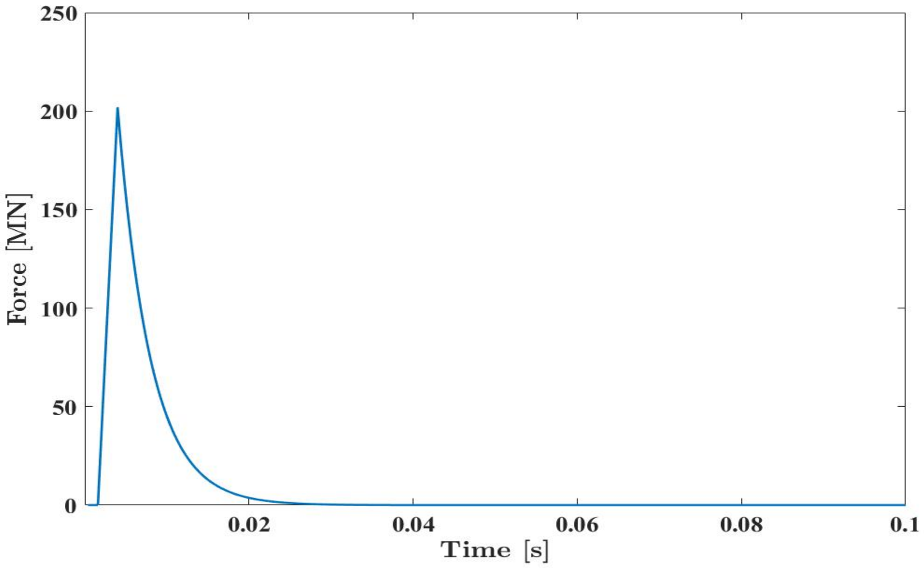

Figure 3.7: Forcing function in the time domain.

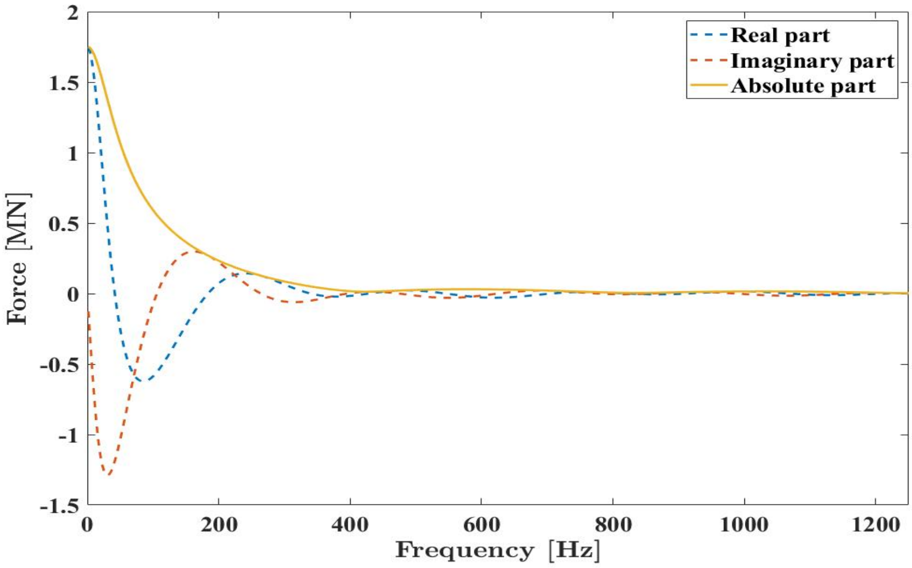

Figure 3.8: Forcing function in the frequency domain.

The final amplitude of the forcing function can be determined by iteratively changing the amplitude until the average energy along the radius of the pile is equal to the energy put into the system by the hammer force. The energy put into the system is given by the measurement data. The forcing function is discretized based on the numerical analysis parameters given in Table 3.1.

MP input parameters

The MP is built up out of 21 cylindrical sections welded together with a diameter ranging from 7.4 m at the bottom to 6.5 m at the top due to it's conically shaped form in the top of the pile. The thickness of the different sections ranges from 60 to 81 mm. The steel type used for the MP of **confidential** is S355. Due to a difference in penetration depth between the unmitigated and the mitigated case there is also a difference in diameter and thickness for both these cases. For the unmitigated case the penetration depth is such that the diameter and thickness of the MP sections covering the fluid-soil domain is constant. For the mitigated case, the penetration depth is deeper and therefore the diameter and thickness are not constant over the fluid-soil domain anymore. Therefore, an average of the diameter and thickness over the sections in the soil-fluid domain is taken.

$$D = \frac{1}{N}\sum_{n=1}^{N} D_n = 7.175 \approx 7.2 \ \text{ m}, \ \text{where N is the number of sections} \tag{3.29}$$

$$t = \frac{1}{N}\sum_{n=1}^{N} t_n = 0.065 \approx 0.07 \ \text{ m}, \ \text{where N is the number of sections} \tag{3.30}$$

An overview of all the input parameters of the MP for both the unmitigated and the mitigated case are given in the Table 3.3.

		Unmitigated case		Mitigated case	
Description	**Parameter**	**Value**	**Unit**	**Value**	**Unit**
Density	ρ	7850	kg/m^3	7850	kg/m^3
Young's modulus	E	210	GPa	210	GPa
Poisson's ratio	ν	0.30		0.30	
Pile length	L	**confidential**	m	**confidential**	m
Penetration depth	L_p	**confidential**	m	**confidential**	m
Pile diameter	D	**confidential**	m	**confidential**	m
Thickness	t	**confidential**	m	**confidential**	m

Table 3.3: MP input parameters based on data of **confidential** of **confidential**.

Site-specific input parameters

The basic model setup with respect to the site-specific input parameters consists of a water column overlying roughly **confidential** layers of **confidential** and **confidential**. The lowest astronomical tide (LAT) is given in survey reports provided by Van Oord and is stated to be **confidential** meter. At the day and time of installation the tidal difference was roughly four meter above LAT for the unmitigated case and roughly two meters above LAT for the mitigated case (Rijkswaterstaat, n.d.). The soil profile and the corresponding densities at the site of **confidential** at the **confidential** are depicted in Table 3.9. A cross section of the soil profile from the engineering report is provided in Appendix B.

Figure 3.9: Soil profile.

A simplification of the soil profile has been made to comply with the maximum number of soil layers possible for SILENCE BUBBLES. The corresponding soil parameters are based on data provided by Van Oord in combination with literature. The top layer is modelled as a 2.5 meter thick clay layer avoiding numerical issues. To represent the bottom four layers, an average of the densities is taken. Subsequently, the compressional wave speed, the compressional attenuation and the shear attenuation are obtained from Table 4.18 from Ainslie (2010). As data from Van Oord is not sufficient to determine the Poisson's ratio, literature from Hamilton (1980) is consulted. The shear wave speed and the Young's modulus are then determined via the following formulae (Aziman et al., 2016). Both the compressional and shear wave speed magnitudes are deemed reasonable as they lie within the range given by Aziman et al. (2016).

$$E = 3\rho(1 - 2\nu)c_p^2 \tag{3.31}$$

$$c_s = \sqrt{\frac{E}{2\rho(1+\nu)}} \tag{3.32}$$

The parameters for the fluid layers of both the unmitigated and mitigated case are given in Table 3.4 and the simplified soil stratification and it's corresponding parameters are given in Table 3.10. The soil profile is equal for both the mitigated and unmitigated case.

		Unmitigated case		**Mitigated case**	
Description	**Parameter**	**Value**	**Unit**	**Value**	**Unit**
Depth	$z_2 - z_1$	**confidential**	m	**confidential**	m
Fluid density	ρ_f	1000	kg/m^3	1000	kg/m^3
Fluid wave speed	c_f	1500	m/s	1500	m/s

Table 3.4: Fluid layer parameters for both the unmitigated and the mitigated case.

Figure 3.10: Simplified soil profile.

3.2.3 Validation results

Input energy

The cumulative energy along the pile is plotted to determine the input energy inserted into the MP by the hammer. The inserted energy by the hammer into the MP is 1750 kJ indicated by the red dotted line in Figure 3.11. The amplitude of the force is determined by an iterative process where the average energy over the air domain has to match the inserted energy by the hammer. An average over the air domain and not the entire domain is taken as the MP does not lose energy to surrounding air and therefore is an adequate representation of the energy in the MP.

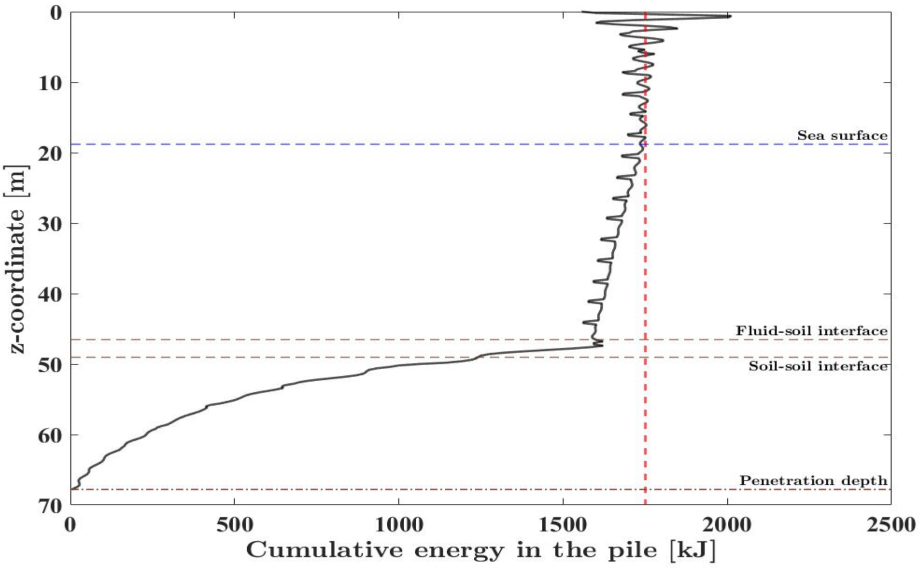

Figure 3.11: Cumulative energy along the pile for the unmitigated scenario.

Arrival time

The arrival times at several radial locations are checked to see if they are in good correspondence with the expected arrival time. An estimation of the arrival times for different radial distances based on compressional wavespeed in the fluid ($t_j = r_j/c_f$) gives $t_1 = 250/1500 = 0.167$ s, $t_2 = 500/1500 = 0.333$ s and $t_3 = 750/1500 = 0.5$ s. Looking at Figure 3.12 it can be seen that the arrival times are in good correspondence to the rough estimations made above.

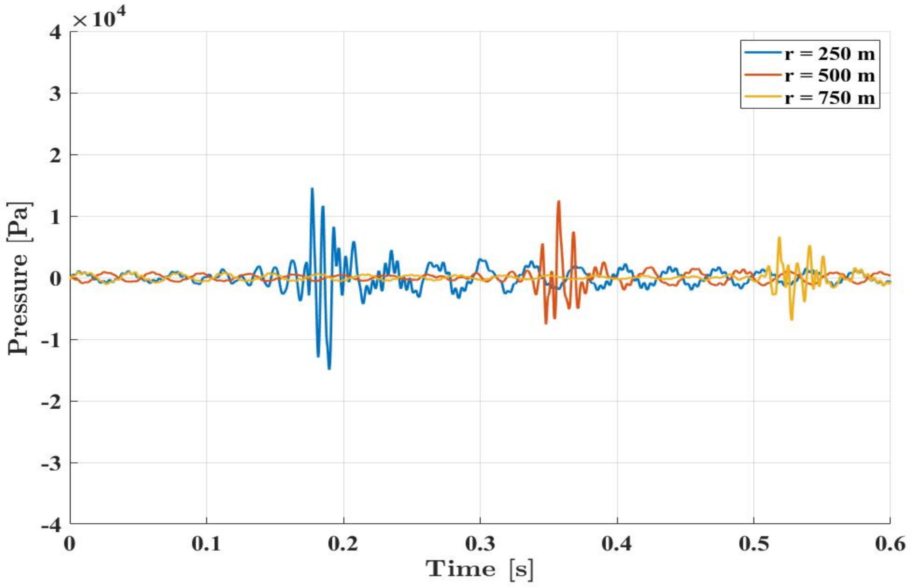

Figure 3.12: Pressure-time signal at different radial distances from the MP.

Sound exposure and peak pressure level

The modelling results with respect to SEL and $L_{p,pk}$ are compared to the measurement data. Figure 3.13 shows the simulated SEL and $L_{p,pk}$ in blue and red respectively. The measured SEL at $r = 750$ m is indicated by the black dot and the measured $L_{p,pk}$ is indicated by the black triangle. The measured SEL and $L_{p,pk}$ were averaged over the hydrophones MP1, MP3 and MP4. This is done by averaging over the term within the logarithm given by Equations (2.6 & 2.7) for all three hydrophones to stay on the linear scale. Both SEL and $L_{p,pk}$ stay within the accuracy of 2 and 3 dB respectively stated by Peng et al. (2021b). A deviation of 1.54 dB and 0.61 dB can be noticed from the measured mean for the SEL and $L_{p,pk}$, respectively.

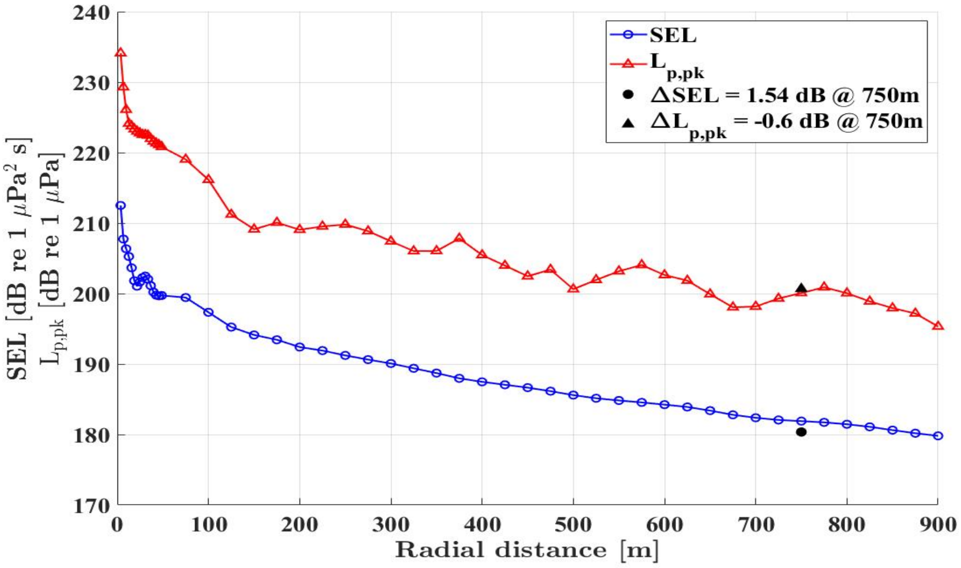

Figure 3.13: Sound exposure and peak pressure level for the unmitigated scenario.

Spectral analysis of the sound exposure level

A spectral analysis of the SEL was performed to validate the frequency content. First, a pressure time recording is transformed from the time to the frequency domain by means of the Fourier transform. Subsequently, the frequency content is determined by binning the frequencies in one-third octave bandwidths in the following manner (Peng et al., 2021b),

$$\mathrm{SEL}_{1/3-\mathrm{Octave}} = 10\log_{10}\sum_{i=m}^{n}\left(\frac{|\tilde{p}_i(\omega)|^2}{p_0^2}\right). \tag{3.33}$$

Figure 3.14 shows the simulated and the measured spectral analysis of the SEL. It has to be taken into account that the measured SEL 1/3-Octave is the average of all blows without the use of a noise mitigation system due to lack of measurement data. It can be seen that for both lines the trend increases up to a frequency of 125 Hz and decreases for frequencies above 125 Hz. This is expected as the dominant frequency for underwater noise due to the installation of large MPs is around 100 Hz.

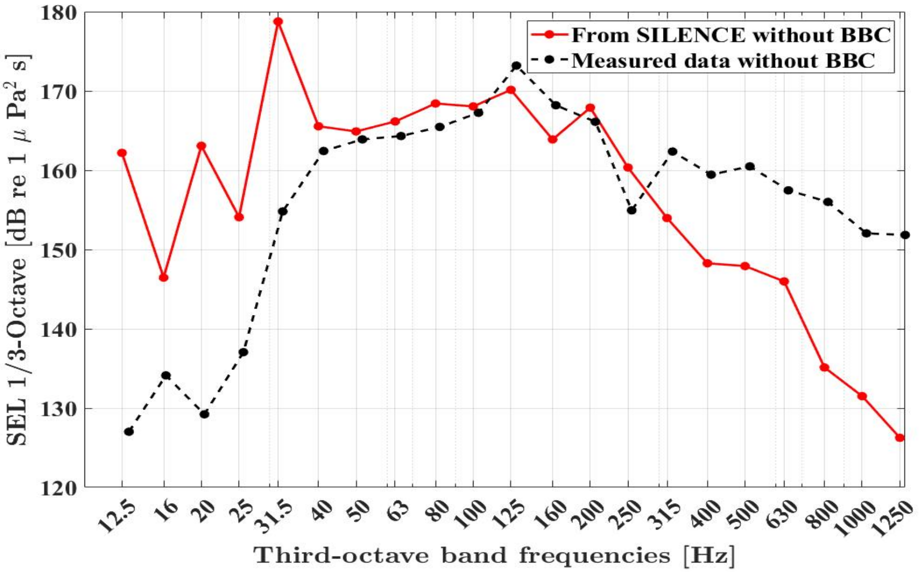

Figure 3.14: SEL per one third octave band for the unmitigated scenario.

3.3 Input parameters for SILENCE BUBBLES

The air supply hoses used at **confidential** had a nozzle diameter between 1 to 2 mm and a nozzle spacing between 20 to 30 cm. The diameter and spacing for **confidential** are averaged to 1.5 mm and 25 cm respectively as it is not clearly specified which diameter and spacing were used at this site. The gas velocity at the nozzles has not been measured during the project and is therefore unknown. For an accurate determination of the gas velocity at the nozzle pressure distribution and losses have to be calculated over the length of the air supply hose which is outside the scope of this thesis. Therefore, the base case gas velocity is determined by iteration based on the best agreement with the measurement data of the SEL at

$r = 750$ m. This yields a base case gas velocity of 108 m/s. Figure 3.15 shows the SEL and $L_{p,pk}$ for the following BBC parameters. These base case parameters are used for the sensitivity study described in Section 4.1.

- Nozzle diameter: 0.0015 m,
- Nozzle spacing: 0.25 m,
- Gas velocity at the nozzle: 108 m/s.

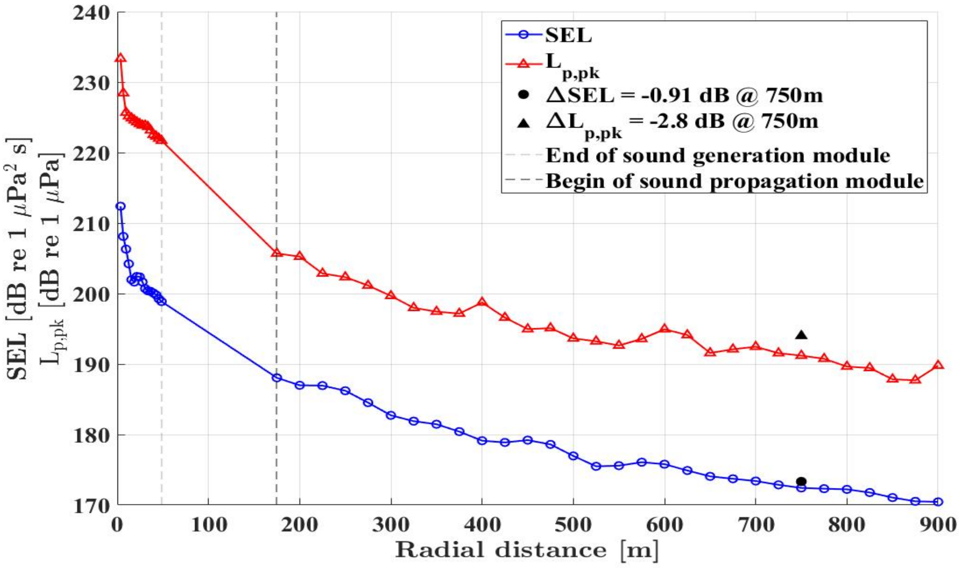

Figure 3.15: SEL and $L_{p,pk}$ for the mitigated base case scenario.

The modelled SEL 1/3-Octave is also compared to the measurement data. Figure 3.16 shows both the modelled and measured SEL 1/3-Octave. From the figure it can be seen that the spectral sound levels are generally lower over the entire frequency range in comparison to the case without a BBC. Also, the higher frequencies ($>$ 400 Hz) are mitigated better by the BBC than the lower frequencies ($<$ 400 Hz). This is in line with Bellmann (2014) which states that a BBC shows an increase in transmission loss for higher frequencies (see Figure 3.4).

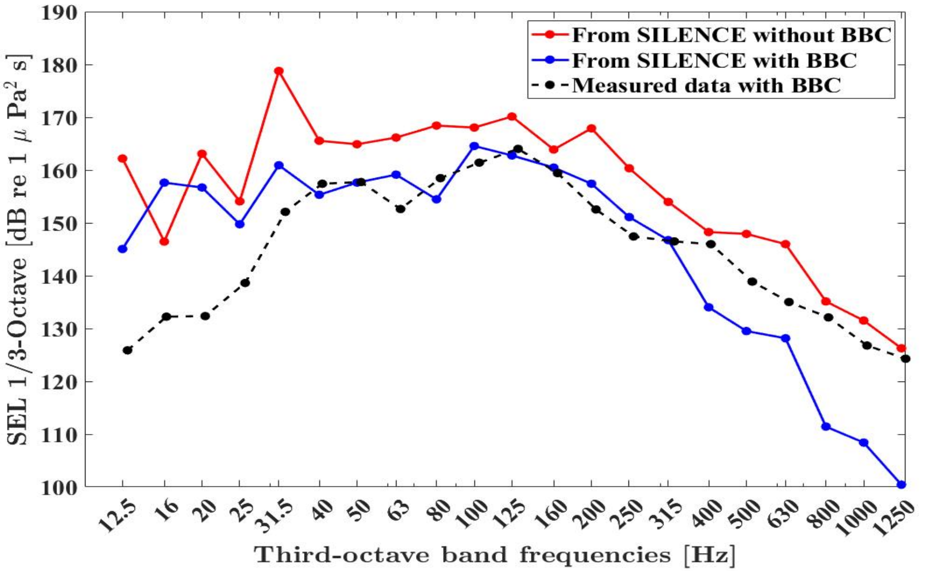

Figure 3.16: SEL per one third octave band for the mitigated base case scenario.

Chapter 4

Optimizing a BBC configuration

This chapter describes a sensitivity study to the different BBC parameters and to the position of the BBC to the MP in Section 4.1. Second, a parametric study is performed to provide insight in the effect of different soil configurations on the performance of a BBC in Section 4.2. Lastly, the optimization of the design of a BBC configuration is discussed in Section 4.3.

4.1 Sensitivity analysis

This section describes the model sensitivity to the BBC parameters defined in Section 3.3 as well as the significance of the radial position of the BBC by means of the full block method. With the full block method, the waterborne path is fully blocked at the position of the BBC and the influence of solely the soil is examined (Peng et al., 2021a).

BBC parameters

The model sensitivities with respect to the BBC parameters were determined by adding 20 % and subtracting 20% of the determined base case parameters (see Section 3.3) while the other parameters were kept constant. In reality, all BBC parameters are dependent on each other, meaning that changing one parameter affects the other parameter. However, for a theoretical approximation of the model sensitivity to each BBC parameter, it is deemed reasonable to analyse them independently. In this way, an idea about the significance of the BBC parameters is obtained. Figures 4.1a and 4.1b and Table 4.1 show the model sensitivities for the gas velocity and the nozzle diameter, respectively. The model sensitivity for the nozzle spacing is absent as the sound reduction module in SILENCE BUBBLES has no dependency on nozzle spacing (Peng et al., 2021b).

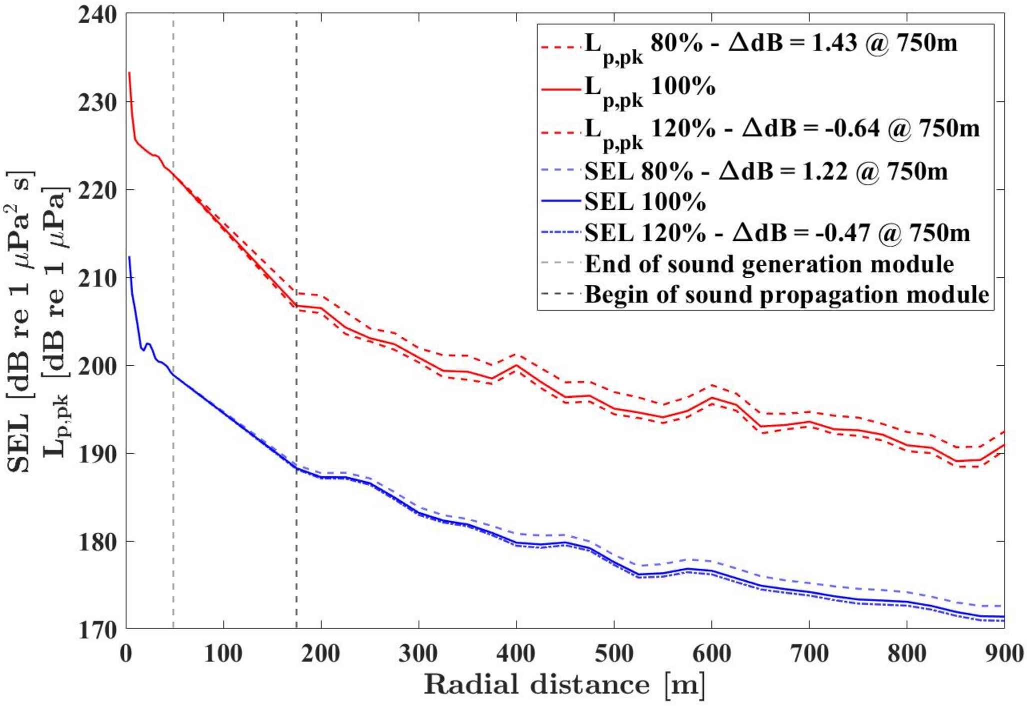

(a)

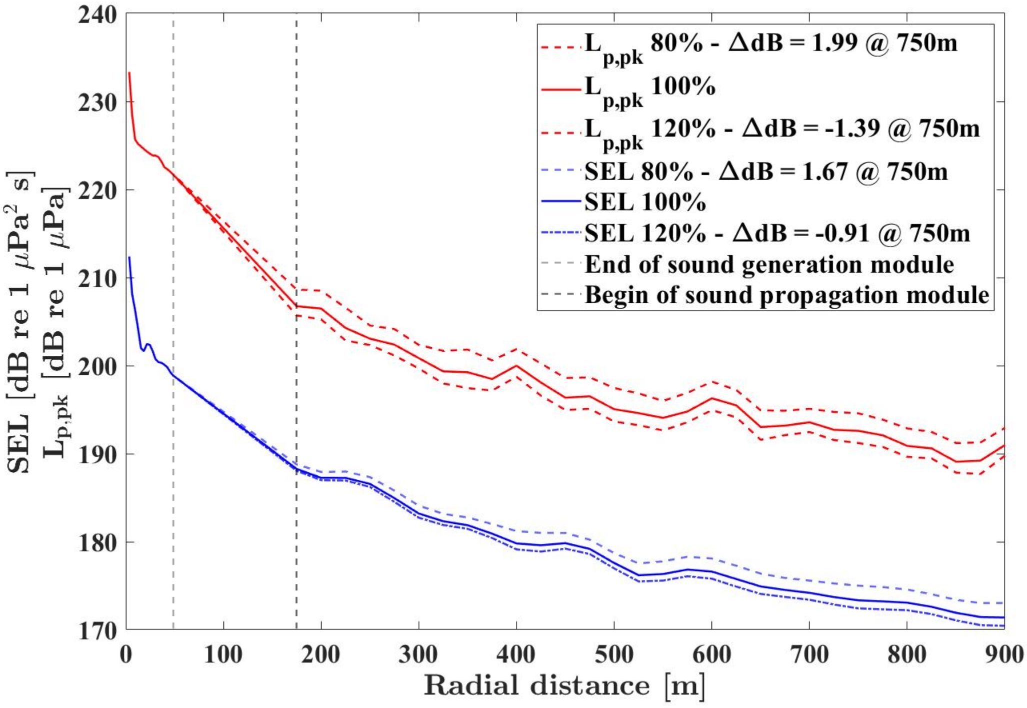

(b)

Figure 4.1: Sensitivity of the model for (a) gas velocity at the nozzle and (b) the nozzle diameter.

	Value	**ΔSEL @ 750m**	**$\Delta L_{p,pk}$ @ 750m**
Gas velocity (80%)	86.4 m/s	1.22 dB	1.43 dB
Gas velocity (120%)	129.6 m/s	-0.47 dB	-0.64 dB
Nozzle diameter (80%)	0.0012 m	1.67 dB	1.99 dB
Nozzle diameter (120%)	0.0018 m	-0.91 dB	-1.39 dB

Table 4.1: Model sensitivities in ΔdB at a radial distance of 750 meters.

Looking Figure 4.1 and Table 4.1, a significant model sensitivity can be observed for both the gas velocity at the nozzle and the nozzle diameter. The model is more sensitive to a decrease than an increase in gas velocity and nozzle diameter for both ΔSEL and $\Delta L_{p,pk}$. These findings show that both the gas velocity at the nozzle and the nozzle diameter have to be taken into account in the optimization study in Section 4.3.

Radial distance of the BBC

The signficance of the radial distance to the mitigation performance of a BBC is investigated in this section to establish whether or not it should be included in the optimization study. For this purpose, a full block is applied for varying radial distances from the MP. The radial distances used were chosen based on common values from literature for single and double BBCs (Bellmann, 2014). The minimal and maximal are set equal to the water depth and the outer diameter of a double BBC configuration, respectively. Figure 4.2 shows the SEL at $r = 750$ m measured at two meters from the seabed after application of the full block at several radial distances from the MP.

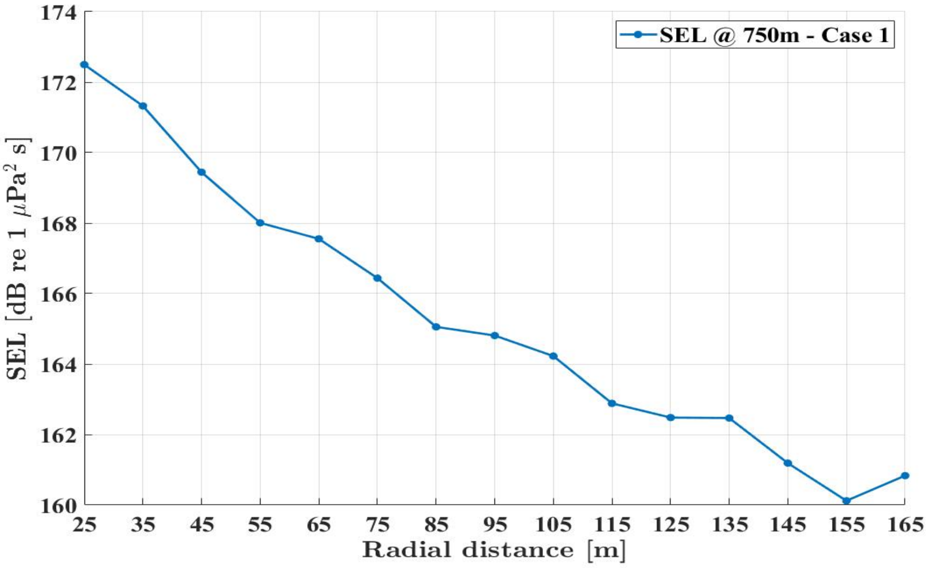

Figure 4.2: SEL at $r = 750$ m for varying radial distance of the full block at two meters above the seabed.

Figure 4.2 shows a decreasing trend in SEL for a full block applied further away from the MP. The maximum difference in SEL is around 12 dB over a distance of 130 meters. The radial position of the BBC is therefore important for the mitigation performance of the BBC and should therefore be part of the optimization study in Section 4.3.

4.2 Mitigation performance of a BBC for different soil configurations

This section describes a parametric study of three different soil configurations to examine their effect on the mitigation performance of a BBC. First, a top layer thickness of two and a half meters (TLT2.5) will be examined in detail. Second, a top layer thickness of ten meters (TLT10) will be addressed in a more concise manner. The soil configurations, hereafter referred to as Case 1 (Top clay), Case 2 (Top sand) and Case 3 (Top mud), and their corresponding parameters are depicted in Table 4.2. The first case has a top clay layer equal to the validated case (see Section 3.2). The second case is a top sand layer with a higher compressional wave speed and higher shear rigidity. The parameters for the top sand layer are equal to the underlying sand layer making it effectively one layer (see Table 3.10). The third case is a top muddy layer with a low compressional wave speed and low shear rigidity. The parameters for Case 3 (Top mud) are based on a marine sediment layer used in Peng et al. (2021a). The three cases were chosen such that a wide range of compressional and shear wave speeds could be addressed.

	Case 1: Top clay		**Case 2: Top sand**		**Case 3: Top muddy**	
Parameter	**Value**	**Unit**	**Value**	**Unit**	**Value**	**Unit**
ρ_s	**conf.**	kg/m^3	**conf.**	kg/m^3	1800	kg/m^3
c_p	**conf.**	m/s	**conf.**	m/s	1604	m/s
c_s	**conf.**	m/s	**conf.**	m/s	81	m/s
α_p	**conf.**	dB/m	**conf.**	dB/m	0.033	dB/m
α_s	**conf.**	dB/m	**conf.**	dB/m	0.068	dB/m

Table 4.2: Examined soil configurations for TLT2.5 and TLT10.

4.2.1 Top layer thickness of two and a half meters

The acoustic response and the mitigation performance of a BBC for all three cases for TLT2.5 is addressed in this section. It is important to note that the input energy into the MP for each case is set equal to 1750 kJ in the same way as is done in Section 3.2.3. Figure 4.3 shows the input energies.

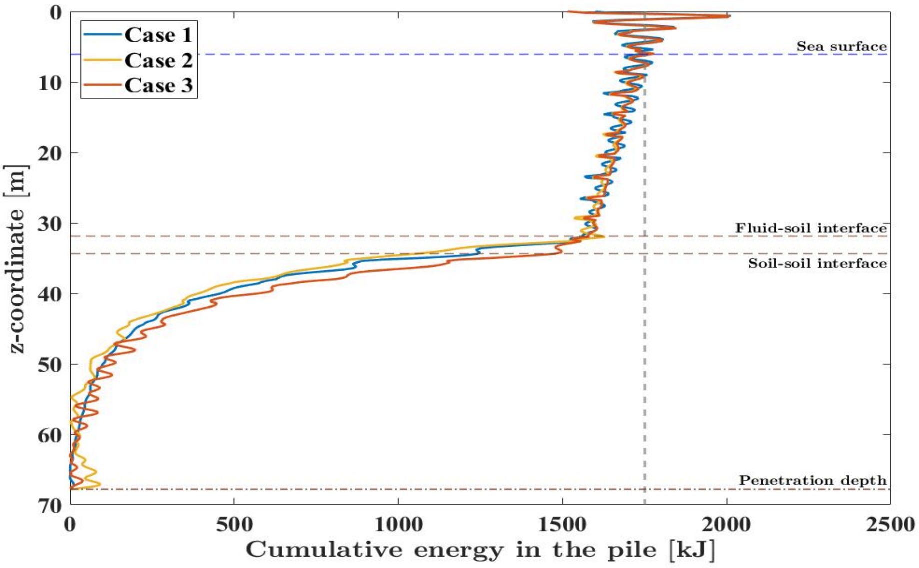

Figure 4.3: Cumulative energy along the pile for all cases for a TLT2.5.

Figure 4.3 shows similar cumulative energies for each case in the air domain above the sea surface similar to the procedure described in Section 3.2.3. A generally higher cumulative energy can be observed for Case 3 (Top mud) in comparison to Case 1 (Top clay) and 2 (Top sand) in the upper soil layer. This means that for Case 3 (Top mud) less energy is dissipated by the MP into the upper soil layer.

The acoustic response in the fluid domain for different soil configurations

A study into the acoustic response of the fluid domain for all three soil configurations was performed. Figures 4.4a and 4.4b show the pressure signal over time for all three cases at $r = 48.7$ m for 0.2 meters and two meters above the seabed, respectively.

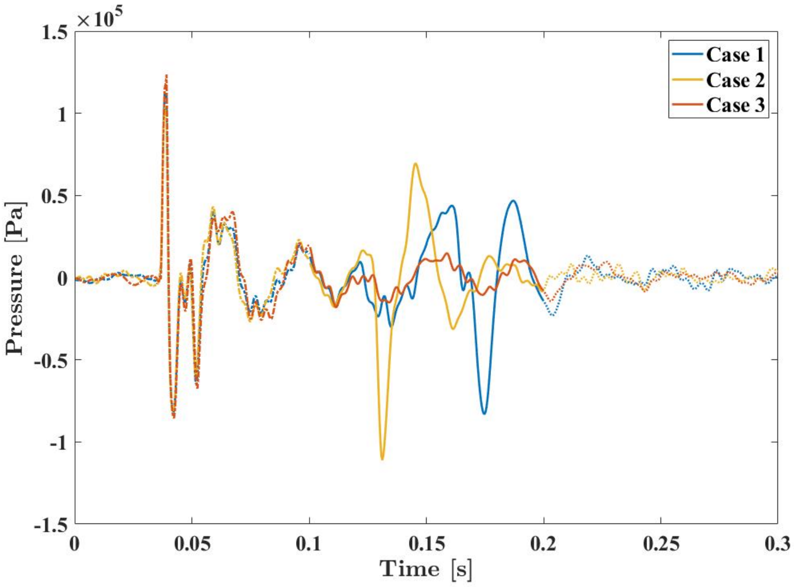

(a)

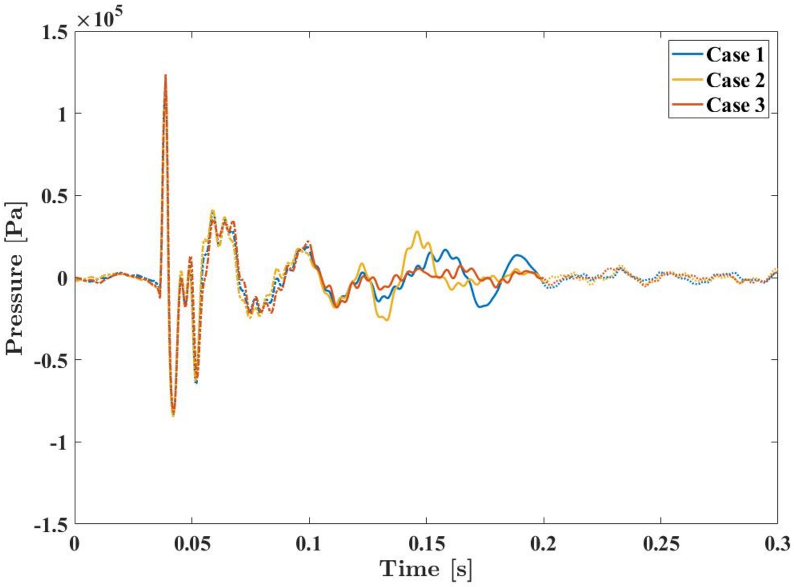

(b)

Figure 4.4: Pressure signal in the time domain at $r = 48.7$ m at (a) 0.2 meters above the seabed and (b) 2 meters above the seabed.

Figure 4.4a shows a clear distinction between two sets of travelling waves. The first set of waves ($t \leq 0.06$ s) shows the arrival of the Mach cone wave. It can be seen that this first set of waves is almost identical for all three cases. This is due to the fact that the fluid domain is equal for all cases. Looking at the second set of waves ($0.125 \leq t \leq 0.2$ s) a large difference in the acoustic responses can be observed. Case 2 (Top sand) shows large amplitudes up to $|1.2 \cdot 10^5|$ Pa, Case 1 (Top clay) shows amplitudes up to $|0.8 \cdot 10^5|$ Pa and Case 3 (Top mud) shows significantly smaller amplitudes up to $|0.3 \cdot 10^5|$ Pa. This is ascribed to the influence of Scholte waves. As can be seen from Figure 4.4b this influence is significantly smaller further away from the seabed, but present. Scholte waves are determined by the shear rigidity of the top layer (Tsouvalas, 2015) whereas their travelling speed is determined by the shear wave speed of the top layer. This explains the later arrival time of the Scholte waves for Case 1 (Top clay).

To examine the composition of the sound waves entering the fluid domain from the soil domain in more detail and further away from the MP, the sound generation module in SILENCE was extended to a radial distance of $r = 213.7$ m. The sound generation module captures the propagation of the sound field over a larger number of points over depth and over the width therefore providing a more detailed representation of the propagated sound field. The results of the larger near field are compared to the results of the smaller near field to substantiate the correctness of the results. The results show good agreement with the smaller near field results and can be found in Appendix C.

Figures 4.5a and 4.5b show the radial and vertical energy just above the seabed from $r = 48.7$ m up to $r = 213.7$ m, respectively.

(a) Radial energy just above the seabed.

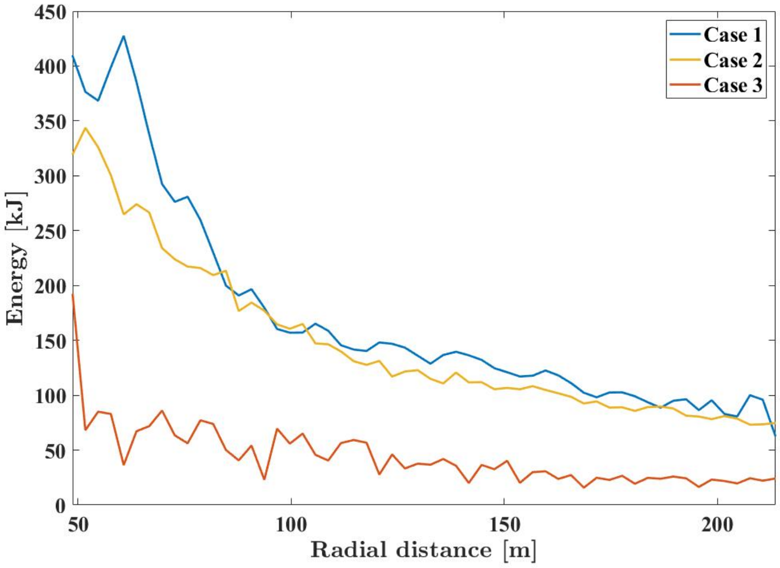

(b) Vertical energy just above the seabed.

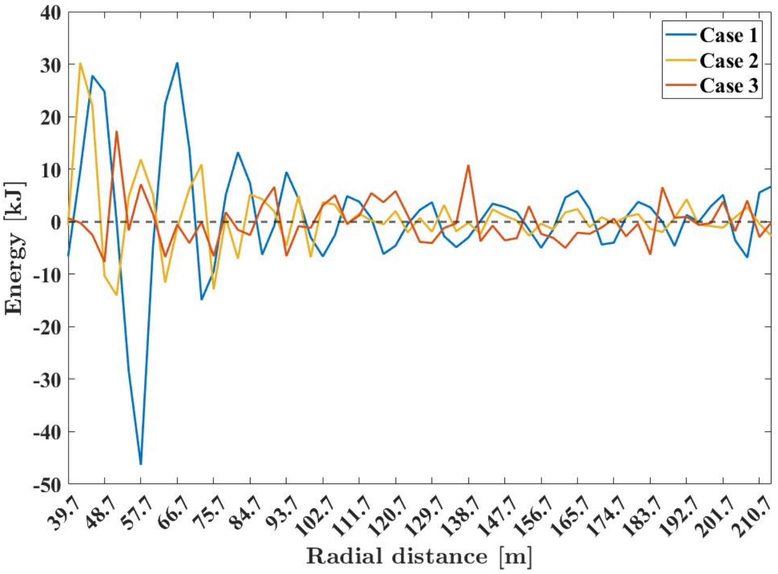

Figure 4.5: Radial (a) and vertical (b) energy at 0.2 meters above the seabed.

The radial energies shown in Figure 4.5a are ascribed to the Scholte waves. The radial energy for Case 3 (Top mud) is significantly less in comparison to Case 1 (Top clay) and 2 (Top sand). A decrease in radial energy over distance is visible for all cases due to the attenuation of the Scholte waves (Tsouvalas, 2015).

Looking at the vertical energies in Figure 4.5b, a clear trend for each case is not visible. Large peaks are noticeable for $r < 75$ m for Case 1 (Top clay) alternated by large troughs. Case 2 (Top sand) and 3 (Top mud) show these peaks as well, however, with a smaller frequency, amplitude, and less distinctive troughs. This can be explained by the fact that Case 1 (Top clay) is more susceptible to constructive and destructive interference of the Scholte waves and the reflections and transmissions in the upper soil layer (see Figure 4.6). Furthermore, more distinct peaks are visible for Case 3 (Top mud) further away from the MP. This can be explained by the low presence of shear rigidity for Case 3 (Top mud) and therefore the low presence of shear and Scholte waves in the upper soil layer. This results in more energy dissipation into the soil domain in the form of compressional waves. As a result, reflections and transmissions in the upper soil layer have larger amplitudes.

The significant differences in the energy profiles are dedicated to the different soil characteristics and their corresponding working mechanisms that cause energy to leak into the fluid domain. The soil characteristics are summarized below and their working mechanisms are schematized in Figure 4.6.

- **Case 1: Top clay layer**
  - Medium to high shear rigidity
  - Impedance mismatch with the underlying soil layer
- **Case 2: Top sand layer**
  - High shear rigidity

  - No impedance mismatch with underlying soil layer

- **Case 3: Top muddy layer**
  - Low shear rigidity
  - Large impedance mismatch with underlying soil layer

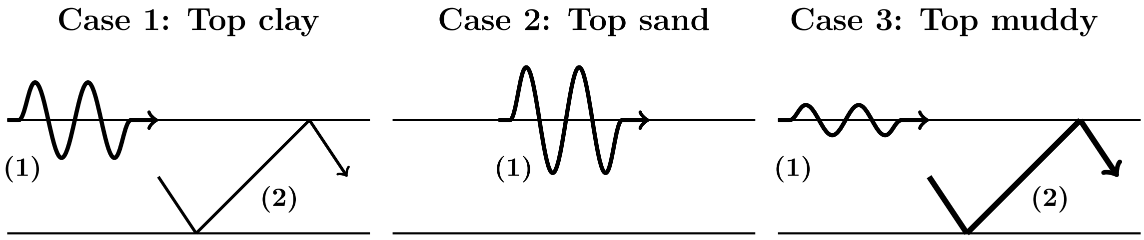

Figure 4.6: Principal working mechanisms for each case where (1) represents the Scholte waves and (2) represents the multiple reflections and transmissions in the upper soil layer.

Case 1 (Top clay) has both the reflections and transmission due to the impedance mismatch at the soil-soil interface as well as Scholte waves at the fluid-soil interface. Case 2 (Top sand) has only Scholte waves at the fluid-soil interface as the top layer is the same as the underlying layer making it effectively one layer. Case 3 (Top mud) has a small contribution of Scholte waves due to a low shear rigidity of the top layer, but a large impedance mismatch at the soil-soil interface.

The acoustic response in the soil domain for different soil configurations

A study into the acoustic response of the soil domain for all three soil configurations was performed. Figure 4.7 shows the normalized energy in the soil domain for all cases for two different radial distances from the MP, namely $r = 24.7$ m and $r = 39.7$ m.

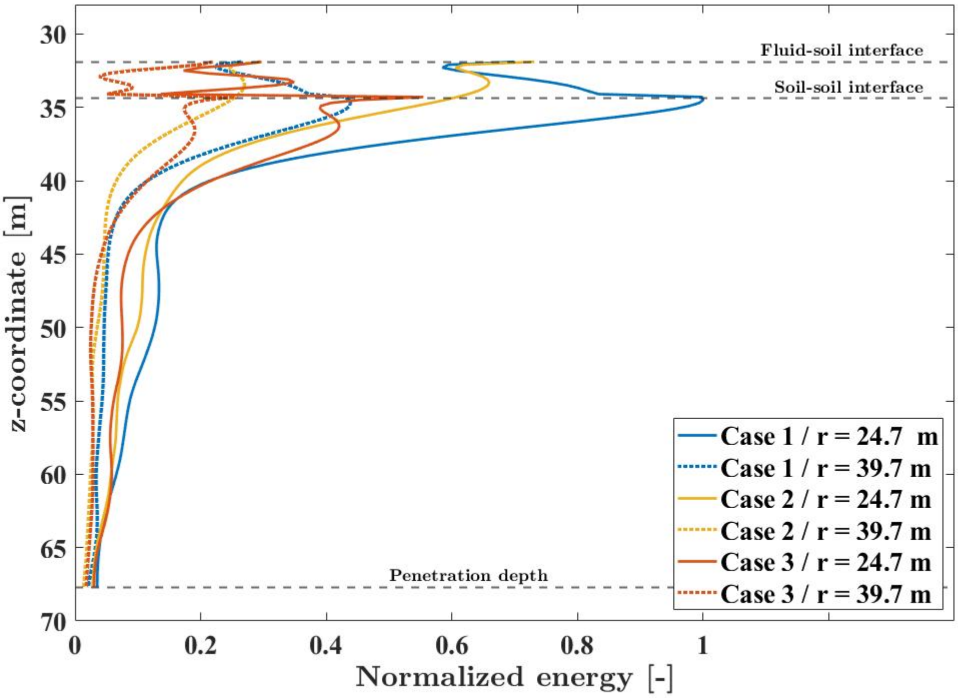

Figure 4.7: Normalized energy in the soil domain for all cases for two different radial distances from the MP, namely $r = 24.7$ m and $r = 39.7$ m.

Looking at Figure 4.7, it can be noticed that the soil configurations which do have an impedance mismatch at the soil-soil interface (Case 1 (Top clay) and 3 (Top mud)) have large peaks of energy at this interface. Case 3 (Top mud), which has the largest impedance mismatch, shows the largest relative peak at this interface. Looking at Case 2 (Top sand), this peak is not visible as the energy line goes through the interface, due to the absence of the impedance mismatch. Furthermore, it can be seen that the energy which is dissipated in the upper soil layer is lowest for Case 3 (Top mud), followed by Case 2 (Top sand), followed by Case 1 (Top clay) for both radial distances. Also, the relative loss of energy between the two radial distances seems lowest for Case 3 (Top mud). A difference between relative loss of energy for Case 2 (Top sand) and 3 (Top mud) is not clearly visible.

Mitigation performance of the BBC for different soil configurations

After the principal working mechanisms have been identified for each soil configuration it was studied how these principal working mechanisms effect the performance of the BBC. The BBC parameters used are equal to the base case parameters from Section 3.3. The SEL and $L_{p,pk}$ for the unmitigated and mitigated scenario are shown in Figures 4.8 and 4.9, respectively.

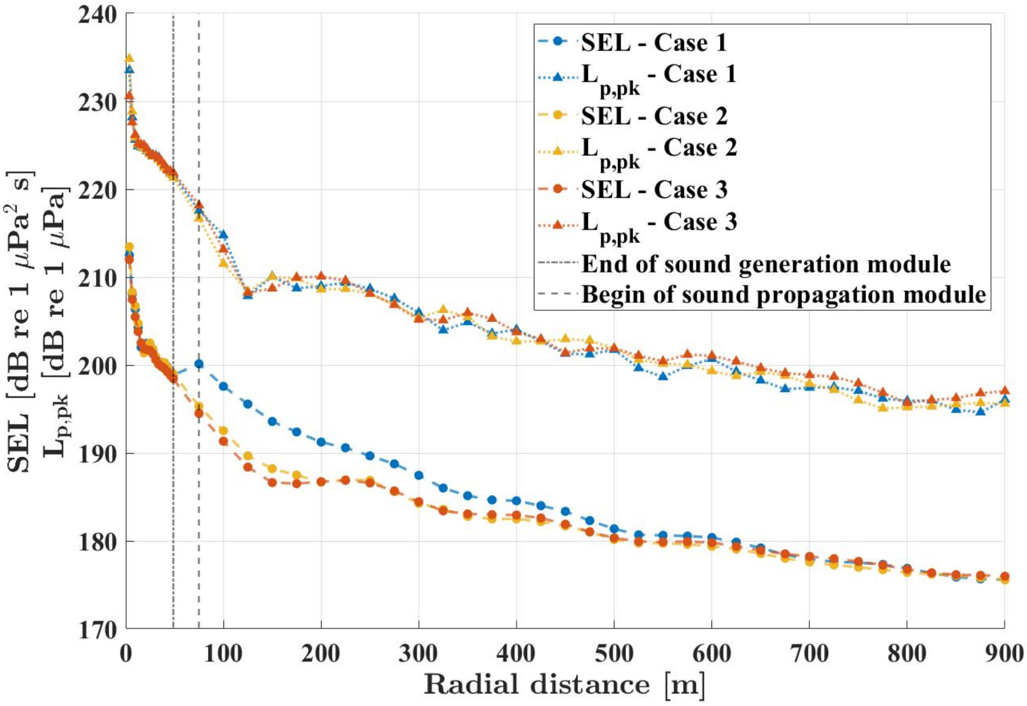

Figure 4.8: SEL and $L_{p,pk}$ for all three cases for the unmitigated scenario at two meters above the seabed.

Looking at the unmitigated scenario in Figure 4.8, $L_{p,pk}$ follows a similar trend for all cases. The SEL follows a similar trend for Cases 2 (Top sand) and 3 (Top mud) with a minor difference between $75 \leq r \leq 200$ m. Case 1 (Top clay) shows a larger SEL of about 5 dB at the beginning of the sound propagation at $r = 75$ m. After $r = 600$ m all SEL converge to well-nigh similar values with a maximum difference of 0.5 dB for each case.

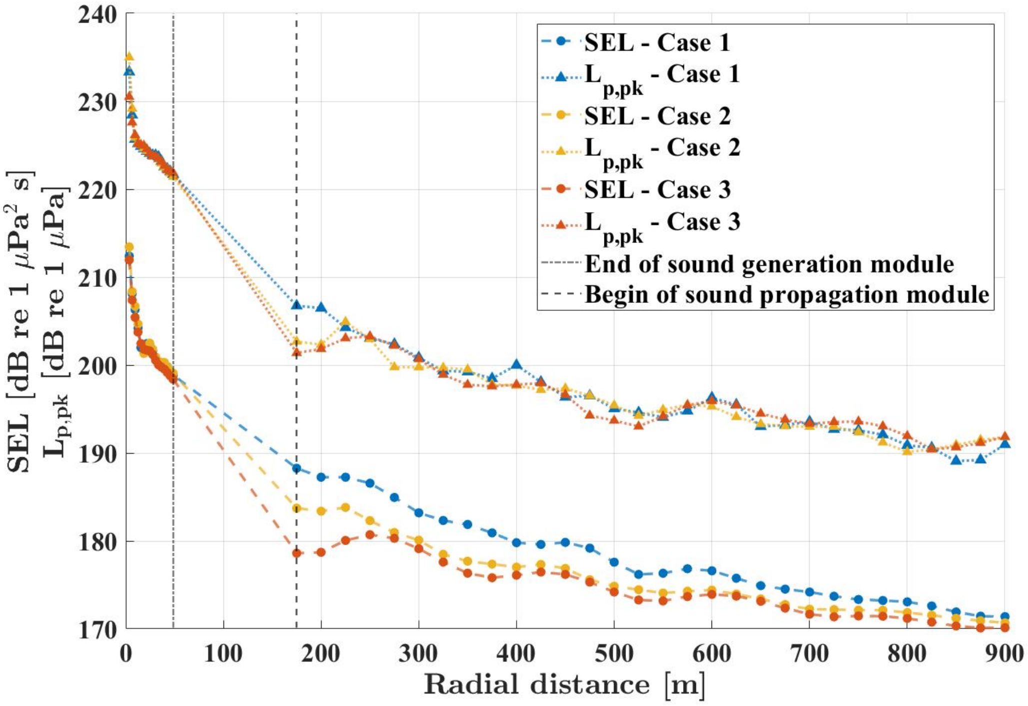

Figure 4.9: SEL and $L_{p,pk}$ for all three cases for the mitigated scenario measured at a point two meters above the seabed.

The mitigated scenario in Figure 4.9 shows a significant difference of about 5 dB between each case at the beginning of the sound propagation module. Over radial distance, a converging trend is visible. The mitigated SEL at $r = 750$ m are slightly further apart in comparison to the unmitigated scenario with differences of around 1.2 dB between each case. The frequency content in terms of SEL 1/3-Octave was studied to investigate where these differences between the mitigated and unmitigated field come from. Figure 4.10 shows the SEL 1/3-Octave at two meters above the seabed before the BBC at a radial distance of $r = 100$ m.

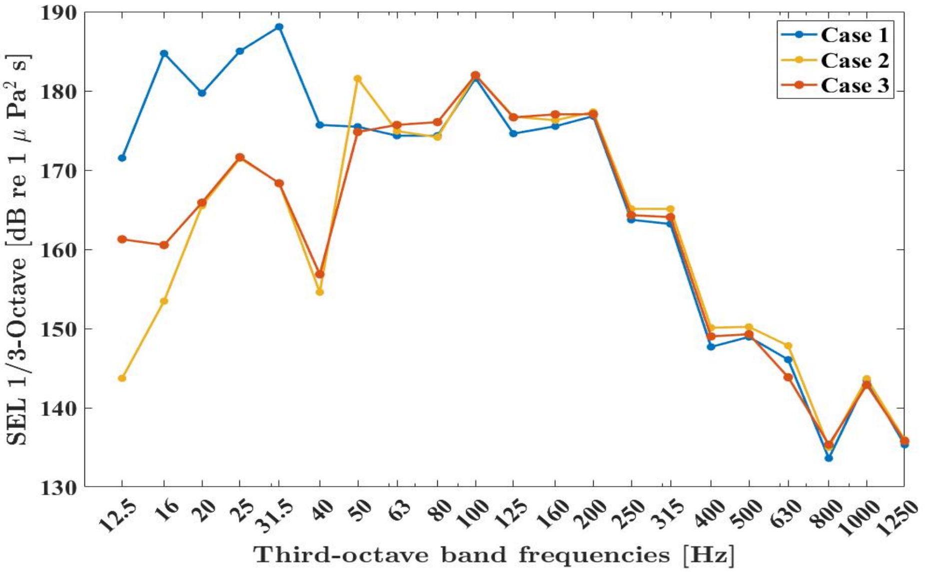

Figure 4.10: SEL 1/3-Octave for all cases just before the BBC (r = 100 m) at 2 meters above the seabed.

It can be noticed that the energies for higher frequencies (f > 50 Hz) are quite similar for all cases. The difference lies in the low frequency regime where Case 1 (Top clay) shows a significantly higher SEL 1/3-Octave in comparison to the other two cases. Case 3 (Top mud) shows a higher SEL 1/3-Octave in comparison to Case 2 (Top sand) for frequencies lower than f < 20 Hz. To assess the mitigation performance by the BBC, the frequency spectra after the BBC at r = 175 m were examined (Figure 4.11). A quantitative analysis of the frequency content directly after the BBC is not possible. The first point of analysis for a BBC located at r = 105 m is at r = 175 m. At this point, energy leakage after the BBC has already influenced the frequency content.

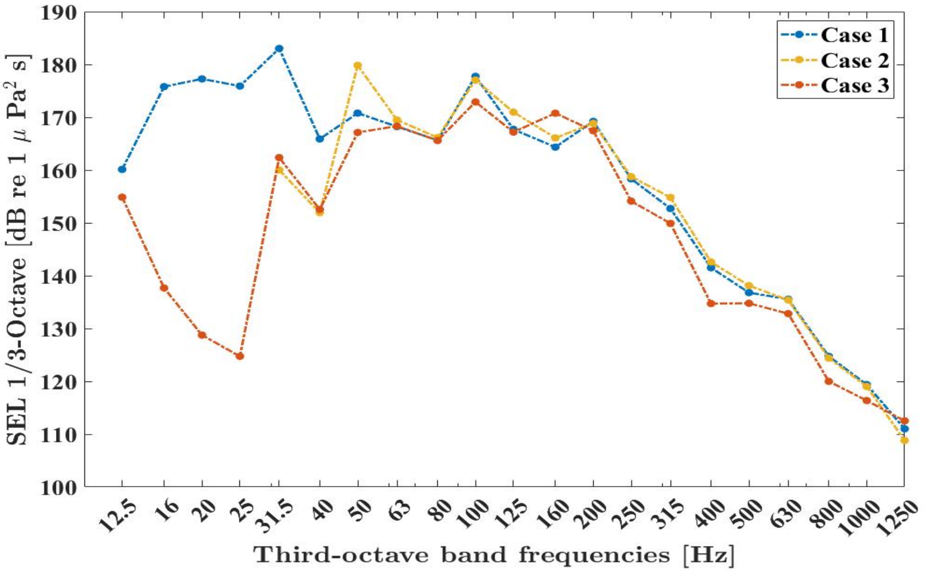

Figure 4.11: SEL 1/3-Octave for all cases after the BBC (r = 175 m) at two meters above the seabed.

Figure 4.11 shows similar energies for the high frequencies ($f \geq 50$ Hz). For frequencies higher than $f = 200$ Hz a slightly lower SEL 1/3-Octave is visible for Case 3 (Top mud) in comparison to Case 1 (Top clay) and 2 (Top sand). Furthermore, for Case 2 (Top sand) no energy can be observed for the frequency regime below $f \leq 35$ Hz. Case 3 (Top mud) shows significantly lower SEL 1/3-Octave compared to Case 1 (Top clay) for the same frequency regime except for $f = 12.5$ Hz. The results for the low-frequency regime for Case 2 (Top sand) and 3 (Top mud) are deemed non-physical and as a result the total SEL for the mitigated scenario in Figure 4.10 was underestimated. A further explanation as to why these results are deemed non-physical is given in Section 4.4.

However, how the order of SEL for each case relates to each other is thought to be correct, as the order can be explained by the difference in energy leakage in the range between BBC ($r = 105$ m) and the first point of analysis ($r = 175$ m) for each case. Figures 4.12a and 4.12b show the radial and vertical energy, respectively, just above the seabed for all three cases in this range. Table 4.3 shows the total sum of radial and vertical energy over the specified range for each case. It can be seen that the dominant energy is ascribed to the Scholte waves which is highest for Case 1 (Top clay), followed by Case 2 (Top sand), and subsequently Case 3 (Top mud). By looking at Figure 4.10, the mitigation performance is expected to be worst for Case 1 (Top clay) due to the high energies at the low frequencies, followed by Case 3 (Top mud), followed by Case 2 (Top sand). Despite a slightly better performance of the BBC for Case 2 (Top sand), it is expected that the radial energy is dominant for the determination of SEL at $r = 175$ m resulting in higher SEL for Case 2 (Top sand) in comparison to Case 3 (Top mud).

(a) Radial energy just above the seabed.

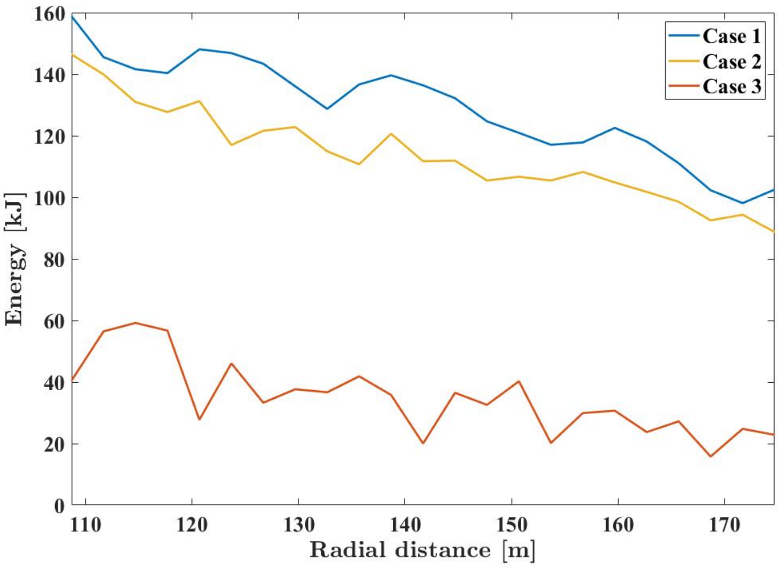

(b) Vertical energy just above the seabed.

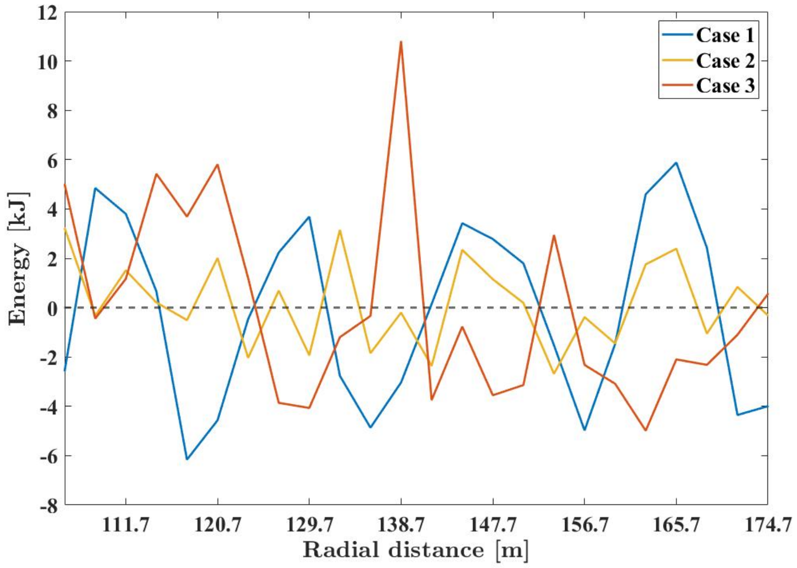

Figure 4.12: (a) Radial and (b) vertical energy just above the seabed for all three cases between $105 \leq r \leq 175$ m.

	Case 1 (Top clay)	**Case 2 (Top sand)**	**Case 3 (Top mud)**
Total radial energy	2969 kJ	2614 kJ	796 kJ
Total vertical energy	81 kJ	37 kJ	118 kJ

Table 4.3: Total radial and vertical energy just above the seabed for $105 \leq r \leq 175$ m

A clear overview of the SEL 1/3-Octave for each case before the BBC, after the BBC for the unmitigated scenario, and after the BBC for the mitigated scenario is given in Figure 4.13. It can be observed that mitigation for Case 1 (Top clay) (Figure 4.13a) occurs for all frequencies. For frequencies above 800 Hz a higher mitigation performance of the BBC is visible. Furthermore, low energy for Case 3 (Top mud) (Figure 4.13c) between $12.5 < f < 31.5$ Hz and no energy for Case 2 (Top sand) (Figure 4.13b) for $f < 31.5$ Hz is visible. As stated before, these results for Case 2 (Top sand) and 3 (Top mud) are deemed non-physical and a further explanation is given in Section 4.4.

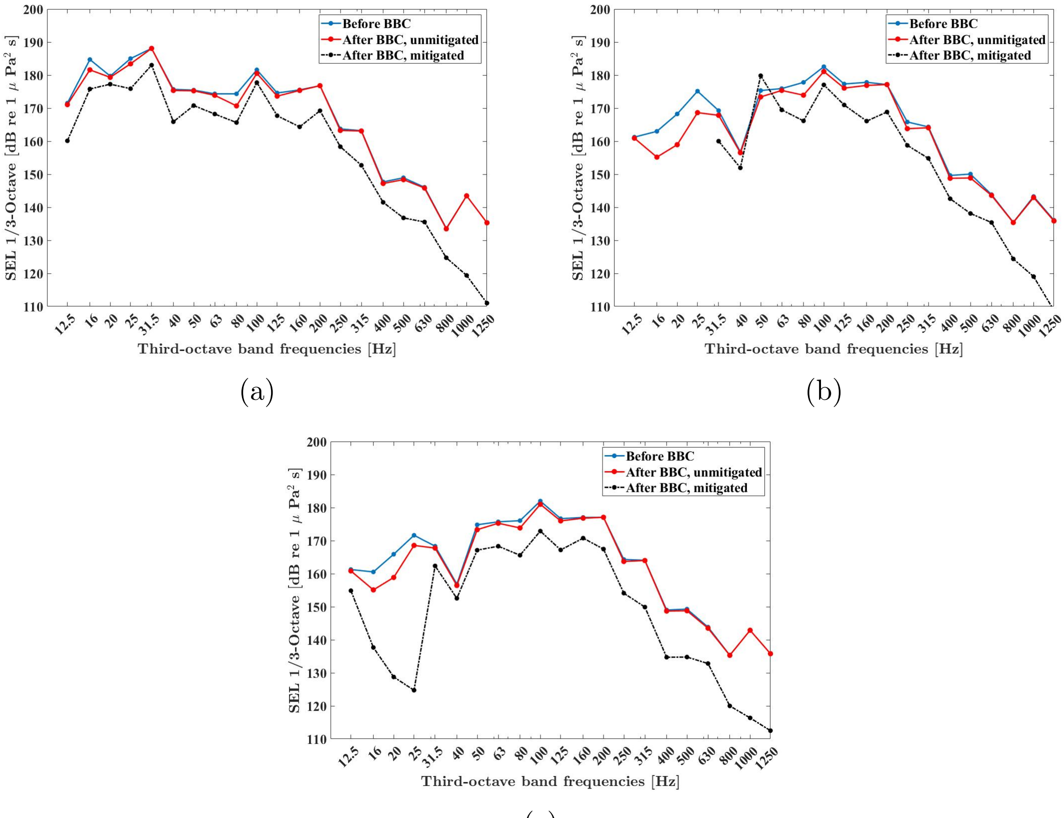

(a)

(b)

(c)

Figure 4.13: SEL 1/3-Octave before the BBC, after the BBC for the unmitigated scenario and after the BBC for the mitigated scenario for (a) Case 1 (Top clay), (b) Case 2 (Top sand), and (c) Case 3 (Top mud).

4.2.2 Top layer thickness of ten meters

First, the input energies into the MP are shown in Figure 4.14.

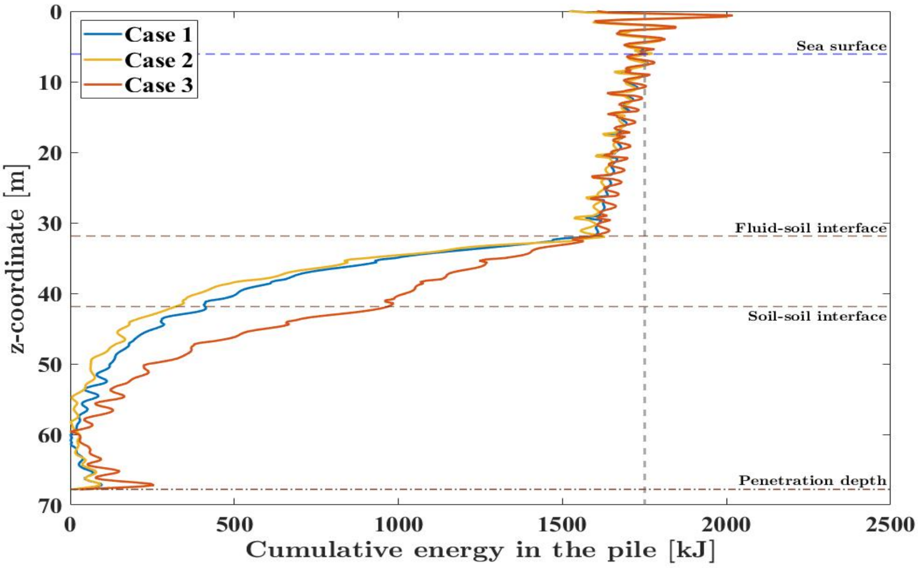

Figure 4.14: Cumulative energy along the pile for all cases for TLT10.

Figure 4.14 shows similar energies in the air domain for all three cases. Furthermore, it can be observed that the cumulative energy in the upper soil layer is significantly higher for Case 3 (Top mud) with difference of around 600 kJ at the soil-soil interface in comparison with Case 1 (Top clay) and 2 (Top sand). This indicates that less energy is dissipated into this soil layer from the MP. At $z = 60$ m the energies are close to similar for each case. A more rapid decrease in energy can be observed for Case 3 (Top mud) from the soil-soil interface to $z = 60$ m.

The acoustic response in the soil domain for different soil configurations

Figure 4.7 shows the normalized energy in the soil domain for all cases for TLT10 for two different radial distances from the MP, namely $r = 24.7$ m and $r = 39.7$ m.

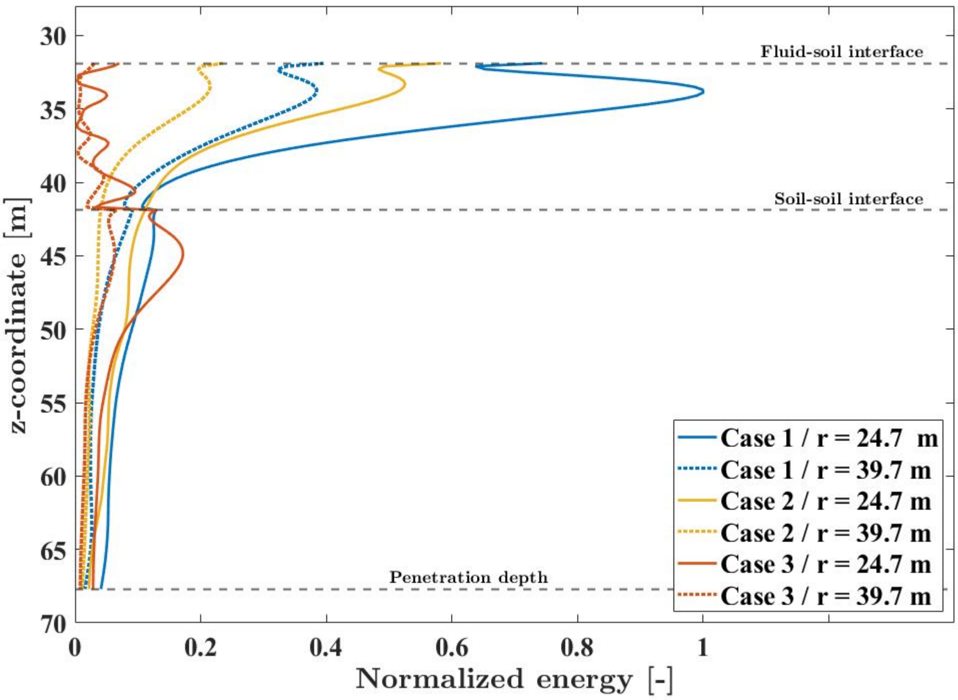

Figure 4.15: Normalized energy in the soil domain for all cases for TLT10 for two different radial distances from the MP, namely $r = 24.7$ m and $r = 39.7$ m.

It can be seen from Figure 4.15 that the energy dissipated into the upper soil layer is significantly lower for Case 3 (Top mud) in comparison to Case 1 (Top clay) and 2 (Top sand). Furthermore, the relative energy loss between the two distances is less for Case 3 (Top mud) in comparison to Case 1 (Top clay) and 2 (Top sand). For Case 1 (Top clay), minor peaks are visible at the soil-soil interface for both radial distances. Case 3 (Top mud) shows relatively large peaks at the soil-soil interface. Also, it can be noticed that the energy in the soil at a radial distance of $r = 24.7$ m between the soil-soil interface and around $z = 48$ m is largest for Case 3 (Top mud). Figure 4.16 shows a comparison between the normalized energy of TLT2.5 and TLT10 for all cases for a radial distance of $r = 9.7$ m.

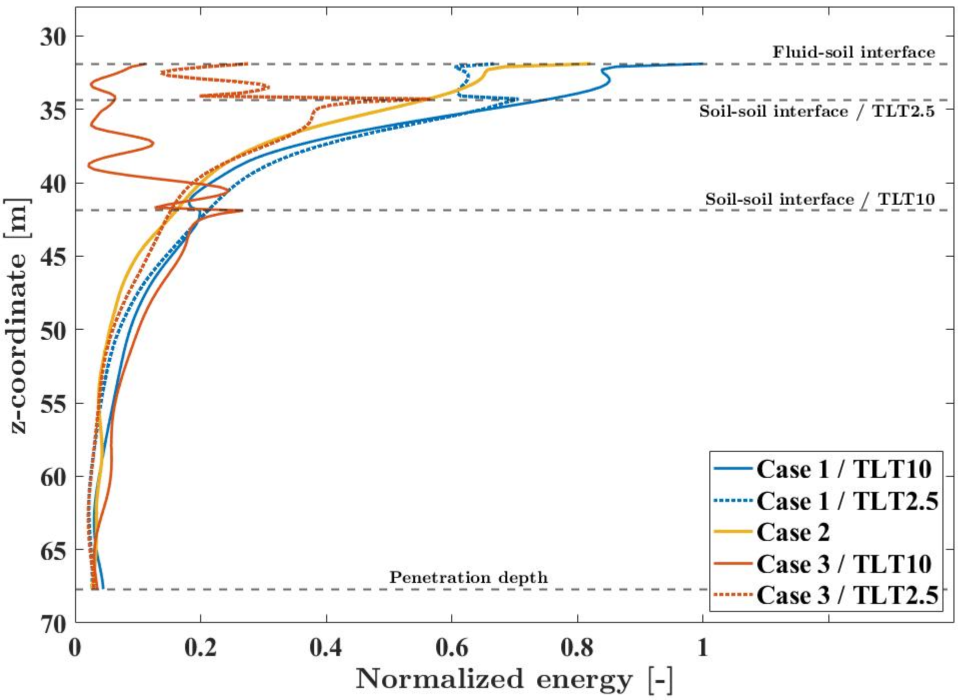

Figure 4.16: Normalized energy in the soil domain for all cases for TLT2.5 and TLT10 for a radial distance from the MP of $r = 9.7$ m.

It can be seen from Figure 4.16 that the energy distribution over the length of the MP is different for each case for TLT2.5 and TLT10. Looking at Case 3 (Top mud), the normalized energy in the soil region up to around $z = 40.5$ m is lower for TLT10, after which the normalized energy for TLT10 is higher. Looking at Case 1 (Top clay), the energy levels up to $z = 35.5$ m are higher for TLT10. A peak in energy is visible for both Case 1 (Top clay) and 3 (Top mud) at both soil-soil interfaces.

Mitigation performance of the BBC for different soil configurations

The numerical instabilities also occurred for the cases for TLT10. For this reason, the results of the mitigated field were omitted and the focus was set on the unmitigated results of the overall SEL and the SEL 1/3-Octave before the BBC. Figure 4.17 shows the SEL and $L_{p,pk}$ for all three cases for a TLT10.

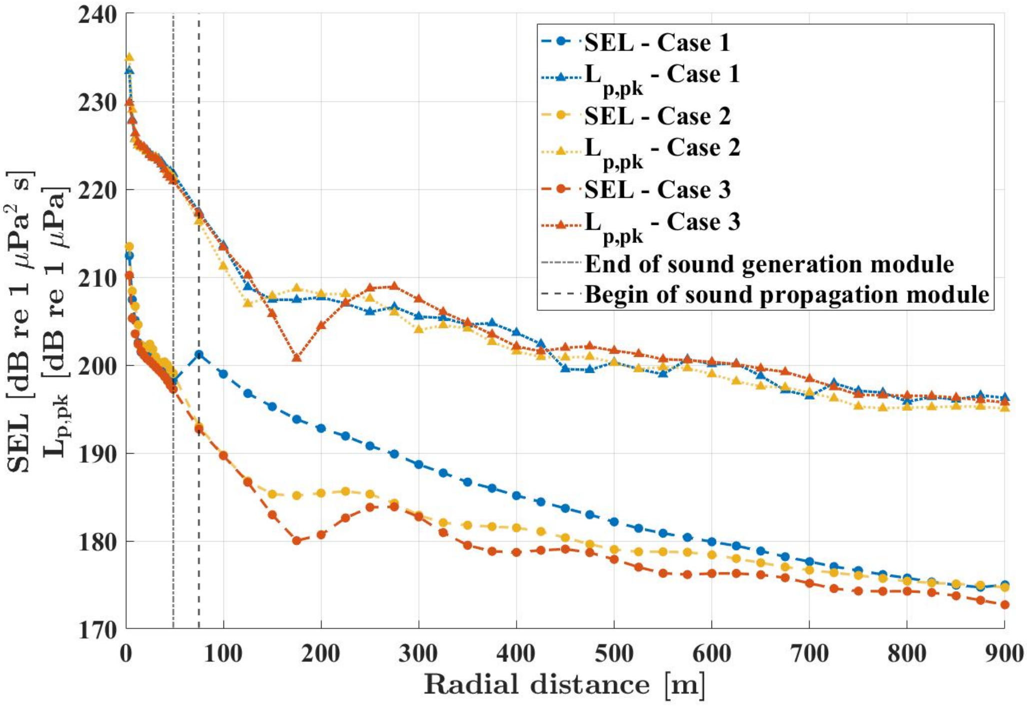

Figure 4.17: SEL and $L_{p,pk}$ for all three cases for the unmitigated scenario at two meters above the seabed.

Looking at the unmitigated scenario in Figure 4.17, $L_{p,pk}$ follows a similar trend for Case 1 (Top clay) and 2 (Top sand). Case 3 (Top mud) shows a trough at $r = 175$ m after which it follows a similar trend to Case 1 (Top clay) and 2 (Top sand). The SEL show larger differences. Case 1 (Top clay) shows larger SEL with a difference of around 8 dB compared to Case 2 (Top sand) and 3 (Top mud) at the beginning of the sound propagation module. From the beginning of the sound propagation module to $r = 900$ m, a faster decrease in SEL can be observed for Case 1 (Top clay) in comparison to the other two cases. Case 2 (Top sand) and 3 (Top mud) show a more oscillatory pattern where the SEL for Case 2 (Top sand) is generally larger than Case 3 (Top mud). At $r = 750$ m, the difference in SEL is around 0.5 dB between Case 1 (Top clay) and 2 (Top sand) and about 1.8 dB between Case 2 (Top sand) and 3 (Top mud).

A comparison of the SEL between the different two top layer thicknesses is shown in Figure 4.18. Furthermore, SEL is integrated over the time domain giving an averaged value. This levels out the influence of local constructive or destructive peaks in the pressure signal providing a more general view on the energy.

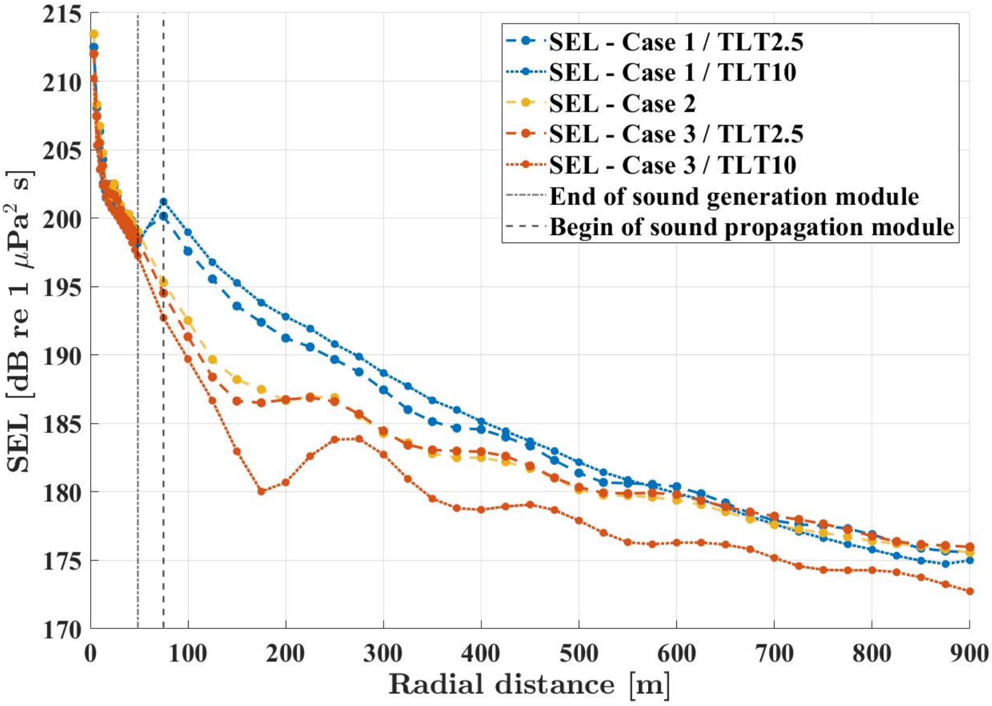

Figure 4.18: SEL for all cases with different top layer thickness for the unmitigated scenario at two meters above the seabed.

As Case 2 (Top sand) is effectively one layer, only one line is plotted. Case 1 (Top clay) shows a larger peak for a TLT10 with a difference of about 1 dB at the beginning of the sound propagation module compared to a TLT2.5. Further away from the MP, a steeper decrease for a TLT10 is visible which results in lower SEL at $r = 750$ m with a difference of around 0.9 dB. A TLT10 for Case 3 (Top mud) results in lower SEL for all radial distances with a difference of around 3.4 dB at $r = 750$ m. A significantly larger bump is visible for Case 3 (Top mud) with TLT10 between $200 \leq r \leq 300$ m in comparison to a TLT2.5.

A comparison of the two top layer thicknesses for the unmitigated SEL 1/3-Octave is shown in Figure 4.19 for a point before the BBC at a radial distance of $r = 100$ m and two meters above the seabed.

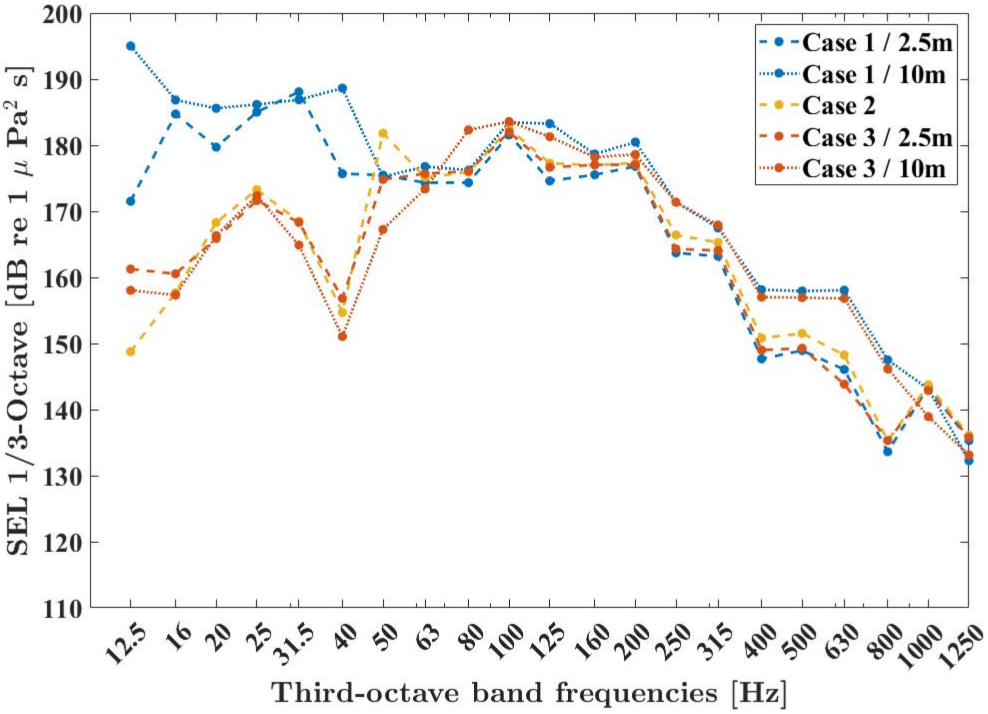

Figure 4.19: SEL 1/3-Octave for all cases with different top layer thicknesses before the BBC at $r = 100$ m at two meters above the seabed.

It can be observed that the SEL 1/3-Octave for Case 1 (Top clay) are higher for all frequencies for a TLT10 compared to a TLT2.5 except for $f = 31.5$ and $f = 900$ Hz. Case 3 (Top mud) with a TLT10 shows higher SEL 1/3-Octave for $f = 20$ Hz, $f = 25$ Hz, and $80 \leq f \leq 800$ Hz compared to a TLT2.5.

4.3 Optimization of a BBC configuration

This section describes the optimization process for a BBC curtain configuration for all three cases focusing solely on TLT2.5. Based on findings in Section 4.1 the following parameters are taken into account for the optimization.

- Radial distance of the BBC
- Gas velocity at the nozzle
- Nozzle diameter

The optimization process for each case consists of five steps which are depicted in Figure 4.20.

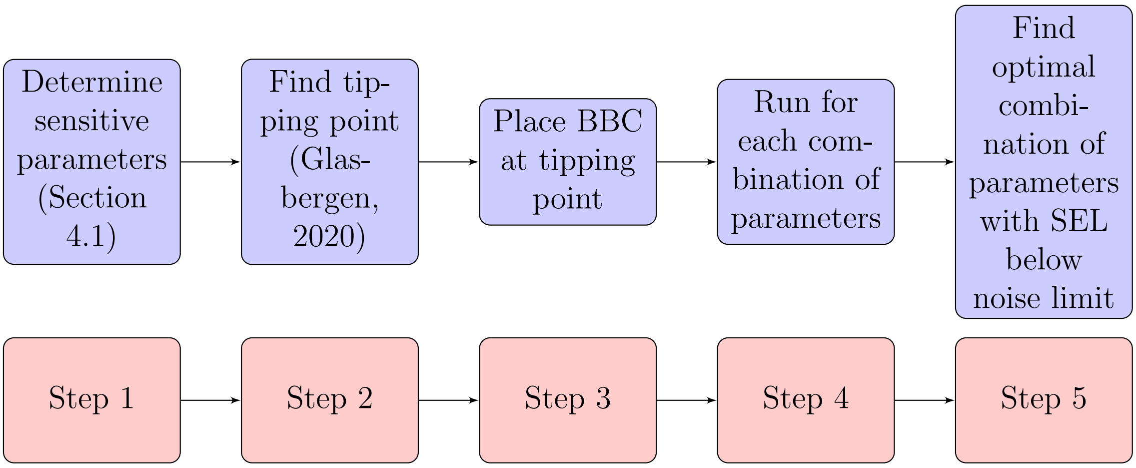

Figure 4.20: Optimization process for a BBC configuration

The first step is to determine the sensitive parameters of the BBC. This has been done in Section 4.1. Second, the tipping point has to be sought. The tipping point is the point after which no significant energy leakage from the soil occurs. This is determined by placing a full block at varying distances from the MP as shown in Figure 4.21 and looking for a tipping point at which no major difference in SEL reduction at $r = 750$ m is observed.

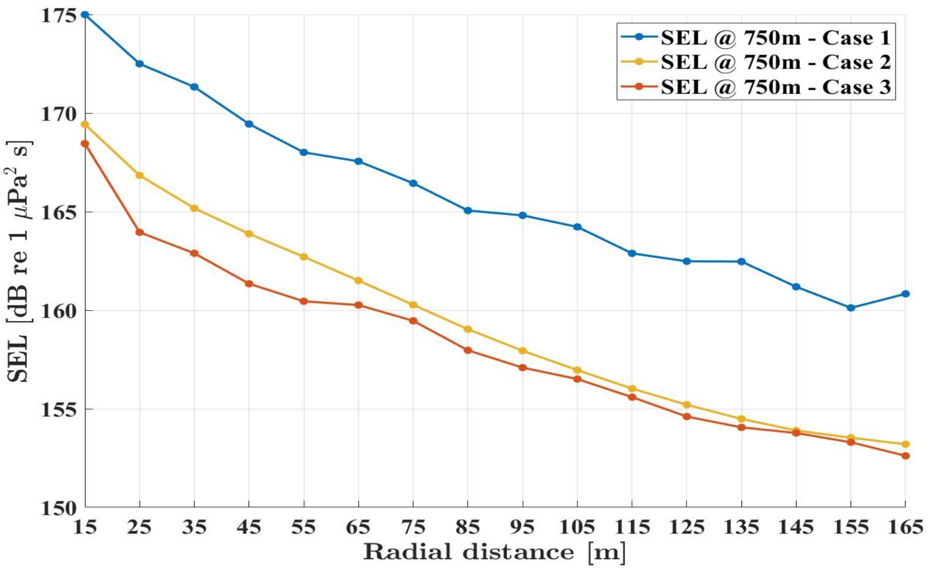

Figure 4.21: SEL at $r = 750$ m at two meters above the seabed for varying radial positions of the full block.

As can be seen from Figure 4.21, no tipping point is observed for radial distances between $15 \leq r \leq 165$ m. Therefore, a robust approach was chosen for determining the optimal combination of parameters. A complete analysis for each combination of the radial distance (65 m $\leq r \leq$ 165 m), gas velocity at the nozzle (70 m/s $\leq u_{gn} \leq$ 130 m/s) and nozzle diameter (0.001 m $\leq d_n \leq$ 0.002 m) was performed. The radial distances and nozzle diameters were chosen based on common values from literature for a single or double BBC (Bellmann, 2014). Since the pressure losses in air supply hoses and related gas velocities at the nozzle have not yet been studied extensively, the range of gas velocities is based on personal communication with academic personnel from TU Delft. This range of gas velocities is deemed reasonable for offshore conditions.

The results are presented as if compliance with a set noise limit at 750 meters is required as is also the case for real projects. An example SEL noise limit will be set at 172 dB re 1 μPa^{2}s based on the noise limit of The Netherlands (see Table 1.1). The results for Case 1 (Top clay), Case 2 (Top sand), and Case 3 (Top mud) together with the set noise limit are presented in Figure 4.22a, 4.22b, and 4.22c, respectively. The gas velocities corresponding to each line are shown right in the figure.

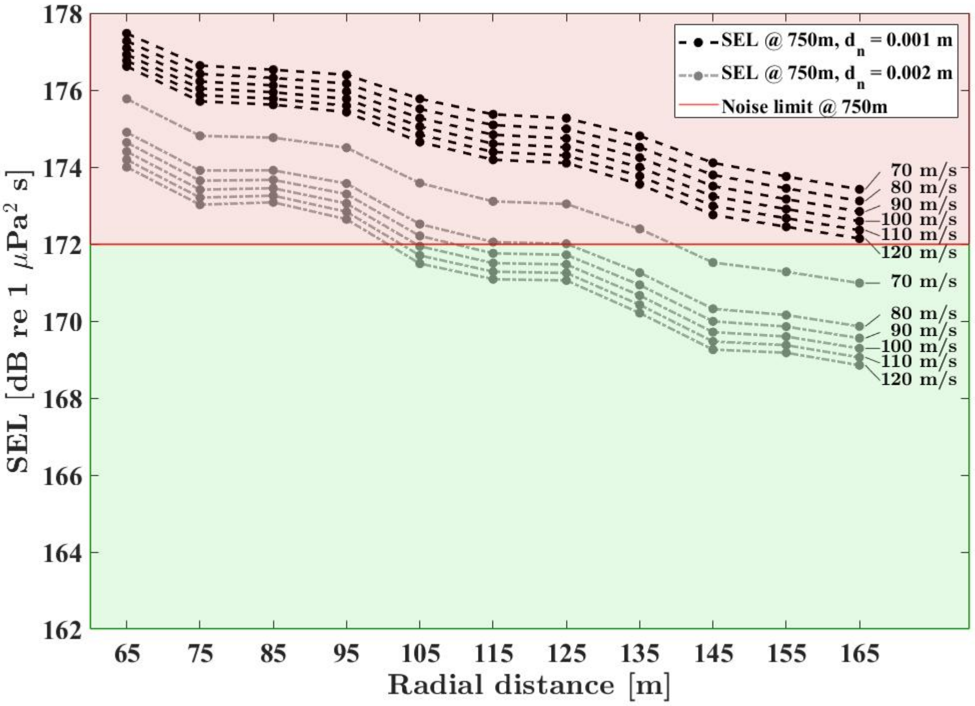
SEL [dB re 1 μPa^2 s]
178
176
174
172
170
168
166
164
162
65
75
85
95
105
115
125
135
145
155
165
Radial distance [m]
SEL @ 750m, d_n = 0.001 m
SEL @ 750m, d_n = 0.002 m
Noise limit @ 750m
70 m/s
80 m/s
90 m/s
100 m/s
110 m/s
120 m/s
70 m/s
80 m/s
90 m/s
100 m/s
110 m/s
120 m/s

(a)

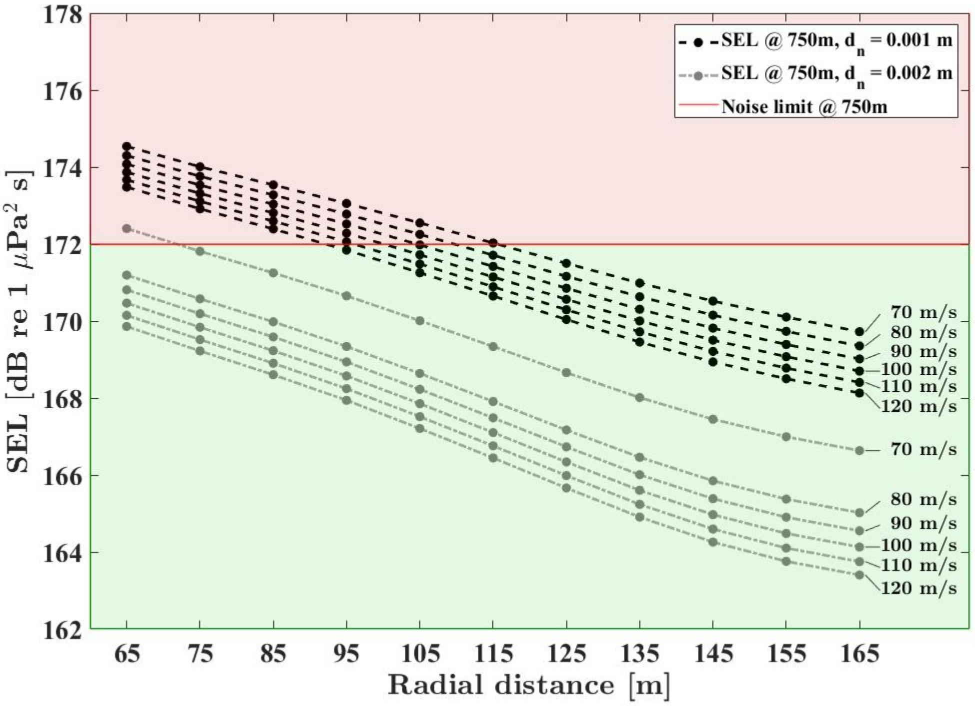
SEL [dB re 1 μPa^2 s]
178
176
174
172
170
168
166
164
162
65
75
85
95
105
115
125
135
145
155
165
Radial distance [m]
SEL @ 750m, d_n = 0.001 m
SEL @ 750m, d_n = 0.002 m
Noise limit @ 750m
70 m/s
80 m/s
90 m/s
100 m/s
110 m/s
120 m/s
70 m/s
80 m/s
90 m/s
100 m/s
110 m/s
120 m/s

(b)

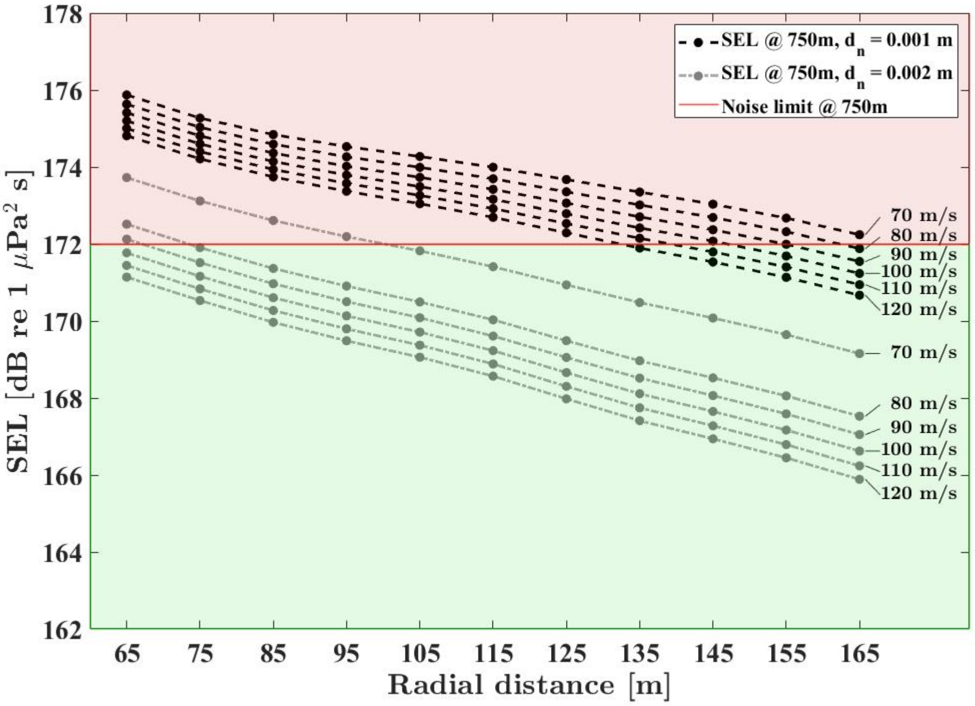

(c)

Figure 4.22: Optimization for (a) Case 1 (Top clay), (b) Case 2 (Top sand) and (c) Case 3 (Top mud).

It can be seen that all three cases have a distinct optimization profile. Furthermore, Figures 4.22a, 4.22b and 4.22c show a non-linear response of SEL to increasing gas velocity. For each case, the SEL decreases for the full range with increasing gas velocity, but this decrease in SEL becomes smaller for higher gas velocities. The range of SEL reduction by the BBC as a percentage of the optimal SEL reduction by a full block for each distance is given in Table 4.4. The minimum and maximum as a percentage of the optimal SEL are determined by Equations (4.1 & 4.2), respectively,

$$\Delta \mathrm{SEL}_{\mathrm{min}} = \frac{\mathrm{SEL}_{\mathrm{ref}} - \mathrm{SEL}_{\mathrm{opt},i}}{\mathrm{SEL}_{\mathrm{ref}} - \mathrm{SEL}_{\mathrm{min},i}}, \tag{4.1}$$

$$\Delta \mathrm{SEL}_{\mathrm{max}} = \frac{\mathrm{SEL}_{\mathrm{ref}} - \mathrm{SEL}_{\mathrm{opt},i}}{\mathrm{SEL}_{\mathrm{ref}} - \mathrm{SEL}_{\mathrm{max},i}}, \tag{4.2}$$

where $\mathrm{SEL}_{\mathrm{ref}}$ is a reference value and i is the radial distance varying from 65 to 165 meter. It can be seen in Table 4.4 that the overall SEL reduction for all cases lies between 20 - 60%. A larger range of maximum reduction potential is seen for Cases 1 (Top clay) and 2 (Top sand) with 8 and 10 % reduction potential, respectively. Case 3 (Top mud) has a range of 5 % maximum reduction potential.

	Case 1: Top clay		**Case 2: Top sand**		**Case 3: Top mud**	
Distance	**Δ**min	**Δ**max	**Δ**min	**Δ**max	**Δ**min	**Δ**max
65 m	24 %	48 %	30 %	55 %	21 %	45 %
75 m	25 %	51 %	30 %	55 %	23 %	46 %
85 m	23 %	47 %	31 %	54 %	23 %	46 %
95 m	24 %	49 %	31 %	55 %	24 %	46 %
105 m	26 %	54 %	32 %	56 %	24 %	47 %
115 m	27 %	52 %	33 %	56 %	25 %	47 %
125 m	27 %	51 %	34 %	58 %	25 %	47 %
135 m	30 %	56 %	35 %	59 %	26 %	48 %
145 m	31 %	57 %	36 %	60 %	27 %	49 %
155 m	31 %	54 %	37 %	61 %	27 %	50 %
165 m	34 %	58 %	38 %	63 %	28 %	50 %

Table 4.4: Minimum and maximum percentage of SEL reduction of the BBC for all three cases in comparison to the optimal reduction by a full block for several radial distances.

4.4 Nota bene

It should be noted that the results regarding the mitigated scenarios have to be handled with a critical view. Looking at the frequency spectra after the BBC shown in Figures 4.11 and 4.13 it can be noticed that Case 2 (Top sand) shows no energy for the low frequency regime ($f < 31.5$ Hz). This is non-physical and caused most likely by a numerical instability during the calculation of the energy for the low frequencies. Case 3 (Top mud) shows significantly lower energies for frequencies between $12.5 < f < 31.5$ Hz compared to the SEL 1/3-Octave before and after the BBC for the unmitigated scenario (see Figure 4.17). This is also deemed non-physical as the performance of the BBC is low for this frequency regime. In addition, energies are present for these low frequencies for the unmitigated case. Therefore, these low energies are most likely a results of numerical instability during calculation. This means that for Case 2 (Top sand) and 3 (Top mud) all total SEL for the mitigated field shown in Figures 4.9, 4.21, and 4.22 are overestimated. A quantitative analysis on the performance of the BBC and the optimization is therefore limited. A qualitative analysis, however, will be discussed in Section 6.1. The percentages in Table 4.4 are relative to the full block which experiences the same underestimation as the mitigated field and is therefore deemed reasonable for quantitative analysis.

Chapter 5

An alternative coupling approach for integrating an air bubble curtain model

This chapter will describe a mode-coupling approach for integrating an air bubble curtain model in an ideal fluid waveguide. The determination of the local effective wavenumber distribution is similar to the approach described in Section 3.1.1, however, the bubble formation process is determined by a lognormal distribution as described in Bohne et al. (2019). For sake of simplicity, the fluid dynamic model is subsequently altered to have a depth-independent effective wavenumber distribution and half width. By means of mode-coupling theory the simplified air bubble curtain model will be coupled to the ideal fluid waveguide and the transmission loss right after the air bubble curtain will be determined. This coupling approach, hereafter referred to as the 2D approach, will be compared to the coupling approach presented in Bohne et al. (2019, 2020) and Peng et al. (2021b), hereafter referred to as the 1D approach. In Section 5.1, the determination of the local effective wavenumber distribution based on Bohne et al. (2019) will be described. Second, the simplified air bubble curtain will be discussed in Section 5.6. Subsequently, mode coupling theory for a ideal fluid waveguide will be elaborated and the simplified air bubble curtain will be implemented.

5.1 Local effective wavenumber distribution

The effective wavenumber distribution as a function of ω, z and r used in Bohne et al. (2019) is based on the work of Commander and Prosperetti (1989) and is given by Equation 5.1.

$$k_{eff}^2(\omega, r, z) = \frac{\omega^2}{c_f^2} + 4\pi\omega^2 \int_0^\infty \frac{an(x,z,a)}{\omega_0^2(z,a) - \omega^2 + 2i\beta(z,a)\omega} \,\mathrm{d}a. \tag{5.1}$$

In Equation 5.1, ω is the angular frequency given by $2\pi f$. The natural angular frequency $\omega_0(z,a)$ is defined by Commander and Prosperetti (1989) and the damping constant $\beta(z,a)$ is defined by Kargl (2002), a is the range of bubble radii and $n(x,z,a)$ is the bubble number density distribution which can be written as,

$$n(x,z,a) = f(x,z,a)N(x,z), \tag{5.2}$$

where $f(x, z, a)$ is the probability density function of the bubble sizes approximated by a lognormal distribution given by Equation 5.3.

$$f(a, \mu, \sigma) = \frac{1}{a\sigma\sqrt{2\pi}} e^{(-\ln a - \mu)^2 / 2\sigma^2} \tag{5.3}$$

The lognormal distribution was fitted to measurement data with a good fit for $\mu = -6.70$ and $\sigma = 0.67$ for a bubble radii range of $a_{min} = 0.0040$ to $a_{max} = 0.013$ (Bohne et al., 2019). $N(x, z)$ is the total number of bubbles which is given as,

$$N(x, z) = \frac{\epsilon(x, z)}{\bar{\nu}(x, z)} \tag{5.4}$$

in which $\epsilon(x, z)$ is the local air fraction over the width and height of the air bubble curtain and $\bar{\nu}(x, z)$ is the mean bubble volume of the bubble population which is given by Equation 5.5,

$$\bar{\nu}(x, z) = \int_0^\infty \frac{4}{3}\pi a^3 f(x, z, a) \, \mathrm{d}a. \tag{5.5}$$

5.1.1 Fluid dynamics of an air bubble curtain

The fluid dynamic equations describing a complex turbulent two-phase bubbly flow for determining the local air fraction of the air bubble curtain are described by Equations (5.6 - 5.8) (Sokolichin et al., 2004). Equations (5.6 - 5.8) describe the momentum flux, liquid mass flux and gas mass flux, respectively (Bohne et al., 2019),

$$\frac{\mathrm{d}}{\mathrm{d}z} \int_{\infty}^{\infty} (1 - \epsilon_g) \gamma \rho_l \bar{u}_{lz}^2 \, \mathrm{d}x = \int_{\infty}^{\infty} \epsilon_g \rho_l g \, \mathrm{d}x, \tag{5.6}$$

$$\frac{\mathrm{d}}{\mathrm{d}z} \int_{-\infty}^{\infty} (1 - \epsilon_g) \rho_l \bar{u}_{lz} \, \mathrm{d}x = 2\alpha \rho_l u_{lzm}, \tag{5.7}$$

$$\frac{\mathrm{d}}{\mathrm{d}z} \int_{-\infty}^{\infty} \epsilon_g \rho_g (\bar{u}_{lz} + u_{rel}) \, \mathrm{d}x = 0, \tag{5.8}$$

where the liquid fraction in the bubbly medium is represented by $(1 - \epsilon_g)$ where ϵ_g is the gas fraction, γ is the amplification factor, ρ_l is the density of the liquid phase, g is the gravitational constant, $\bar{u}_{lz}$ is the vertical liquid velocity, α is the entrainment coefficient, u_{lzm} is the vertical centerline liquid velocity and u_{rel} is a constant relative velocity (Bohne et al., 2019). The vertical liquid velocity $\bar{u}_{lz}$ and the gas fraction ϵ_g are approximated by Gaussian profiles,

$$\bar{u}_{lz}(u_{lzm}, b, x) = u_{lzm} e^{-x^2/b^2}, \tag{5.9}$$

$$\epsilon_g(\epsilon_{gm}, b, x) = \epsilon_{gm} e^{-x^2/(\lambda^2 b^2)}, \tag{5.10}$$

where ϵ_{gm} is the centerline gas fraction, b is the half width of the Gaussian function and λ is the spreading coefficient. By defining the initial gas mass flow as a system parameter, Equation 5.8 can be rewritten as,

$$\dot{m}_0 = \int_{\infty}^{\infty} \epsilon_g \rho_g (u_{lz} + u_{rel}) \, \mathrm{d}x. \tag{5.11}$$

After integration it can be solved for b,

$$b(\epsilon_{gm}, u_{lzm}, \rho_g) = \frac{\dot{m}_0}{\epsilon_{gm} \sqrt{\pi} \lambda \rho_g \left(\left(u_{lzm} / \sqrt{(\lambda^2 + 1)} \right) + u_{rel} \right)}. \tag{5.12}$$

Equations (5.6, 5.7 & 5.12) can subsequently be summarized in vector form in the following manner,

$$\frac{\mathrm{d}}{\mathrm{d}z}(\mathbf{m}(\mathbf{u}, z)) = \mathbf{b}(\mathbf{u}, z). \tag{5.13}$$

In Equation 5.13, the vector $\mathbf{m}$ represents the momentum and liquid flux, the vector $\mathbf{b}$ represents the source term and the vector $\mathbf{u} = [u_{lzm}, \epsilon_{gm}]^T$ representing the unknown variables, the centerline velocity and gas fraction, respectively. (Bohne et al., 2019).

In order to solve the linear system of equations given by Equation (5.13) the Forward Euler method is used. The following initial conditions are derived and are solved by means of iteration (Bohne et al., 2019),

$$b_0 = \frac{\dot{m}_0}{\epsilon_{gm0} \sqrt{\pi} \lambda \rho_{g0} \left(\left(u_{lzm0} / \sqrt{(\lambda^2 + 1)} \right) + u_{rel} \right)}, \tag{5.14}$$

$$u_{lmz0} = \frac{\sqrt{2 M_0} (2\lambda^2 + 1)^{1/4}}{\pi^1/4 \sqrt{\left(\sqrt{(4\lambda^2 + 2)} - 2\epsilon_{gm0} \lambda \right) \gamma b_0 \rho_l}}. \tag{5.15}$$

M_0 is the initial momentum flow and is written as,

$$M_0 = \frac{4 \Delta y_n \dot{m}_0^2}{\pi \rho_{g0} d_n^2}, \tag{5.16}$$

with the nozzle diameter d_n, the nozzle spacing Δy_n and the initial gas density at the nozzle ρ_{g0}. The initial centerline gas fraction is assumed to be 0.95 as gas is highly concentrated in close proximity to the nozzle around the middle axis (Bohne et al., 2019). For validation, the modelled centerline velocity is compared to the modelling results of Bohne et al. (2019), see Figure 5.1.

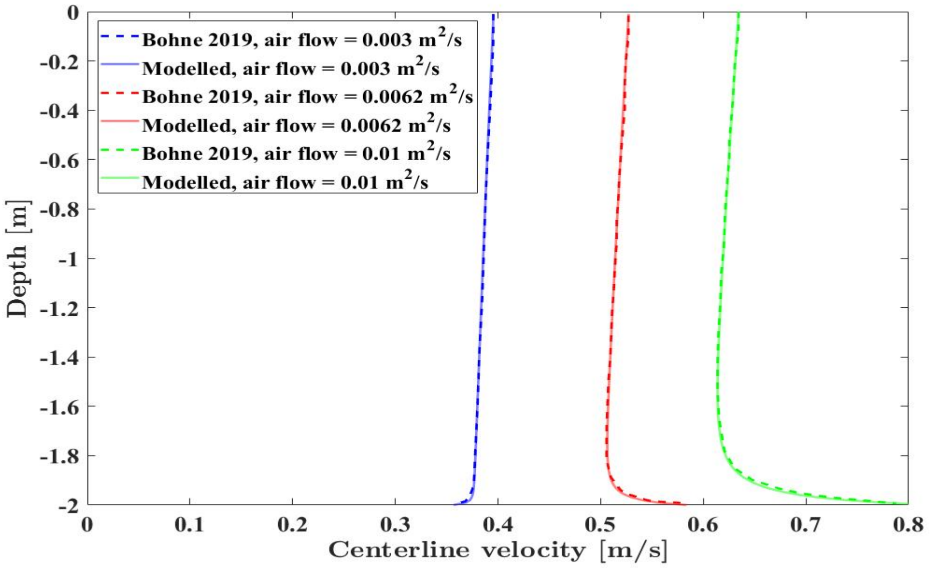

Figure 5.1: Comparison of the modelled centerline velocity to the modelled centerline velocity of Bohne et al. (2019)

Once the system of linear equations for the unknown variables (5.13) is solved for the centerline velocity and gas fraction, the Gaussian distribution of the vertical liquid velocity $\bar{u}_{lz}$ and gas fraction ϵ_g is known over the depth by means of Equations (5.9 & 5.10). Subsequently, the gas fraction distribution can be used to solve for the total number of bubbles $N(x,z)$ from Equation (5.4) and the bubble number density distribution can be solved by implementing the total number of bubbles in Equation (5.2). All variables in Equation (5.1) are now known to solve for the effective wavenumber distribution.

5.2 Validation of the transmission coefficients

By means of the transfer matrix described in Section 3.1.2 the transmission coefficient function is given by Commander and Prosperetti (1989) as,

$$\tau(z,\omega) = |p_n^+|^2. \tag{5.17}$$

Bohne et al. (2019) defined a transmission coefficient for the air bubble curtain given in Equation (5.18).

$$\tau_{bc}(\omega) = \sum_{l=1}^{m} \tau_l \frac{\Delta z_l}{T} \tag{5.18}$$

The transmission loss of the air bubble curtain is subsequently given in Equation (5.19).

$$TL = 10 \log \left(\frac{1}{\tau_{bc}} \right) \tag{5.19}$$

The modelling results for the transmission coefficient function is compared to the modelling results from Bohne et al. (2019) in Figures 5.2.

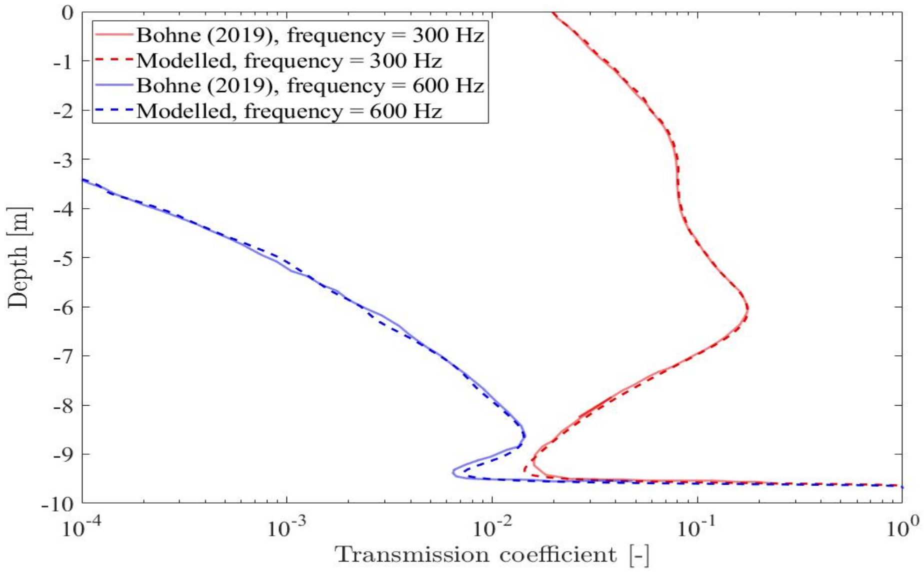

Figure 5.2: Comparison of the modelled transmission coefficients to the modelled transmission coefficients of Bohne et al. (2019)

The transmission coefficient function is validated in order to substantiate the correctness of the effective wavenumber distribution and the transfer matrix. Once the effective wavenumber distribution is obtained it can be simplified to a depth and width independent wavenumber distribution (Section 5.6). The simplified effective wavenumber distribution is subsequently implemented in an ideal fluid waveguide.

5.3 Point source in an ideal fluid waveguide

To narrow down the scope of this thesis a point source is modelled in an ideal fluid waveguide based on Jensen et al. (2011). The pressure in the field will be expressed in the modal domain, so that in a later stage the mode-coupling approach can be applied to integrate the air bubble curtain model in the ideal fluid waveguide. The ideal fluid waveguide consists of one fluid layer with a pressure release boundary condition at the surface and a rigid bottom boundary condition at the bottom (Jensen et al., 2011). The fluid density ρ_f and the wavespeed c_f are assumed constant over the entire domain. Figure 5.3 shows a schematic of an ideal fluid waveguide with a point source at the source depth z_s.

The mathematical derivation of a point source in a cylindrical geometry is described by Jensen et al. (2011) and is given by Equation (5.20),

$$\frac{1}{r}\frac{\partial}{\partial r}\left(r\frac{\partial p}{\partial r}\right)+\rho_f(z)\frac{\partial}{\partial z}\left(\frac{1}{\rho_f(z)}\frac{\partial p}{\partial z}\right)+\frac{\omega^2}{c_f^2(z)}p=-\frac{\delta(r)\delta(z-z_s)}{2\pi r}. \tag{5.20}$$

The unforced solution of Equation (5.20) is sought in the form $p(r,z)=\Phi(r)\Psi(z)$ by means of separation of variables. After substituting the expression for $p(r,z)$ in Equation (5.20) the following equation is found (Jensen et al., 2011),

$$\frac{1}{\Phi}\left[\frac{1}{r}\frac{\mathrm{d}}{\mathrm{d}r}\left(r\frac{\mathrm{d}\Phi}{\mathrm{d}r}\right)\right]+\frac{1}{\Psi}\left[\rho_f(z)\frac{\mathrm{d}}{\mathrm{d}z}\left(\frac{1}{\rho_f(z)}\frac{\mathrm{d}\Psi}{\mathrm{d}z}\right)+\frac{\omega^2}{c_f^2(z)}\Psi\right]=0. \tag{5.21}$$

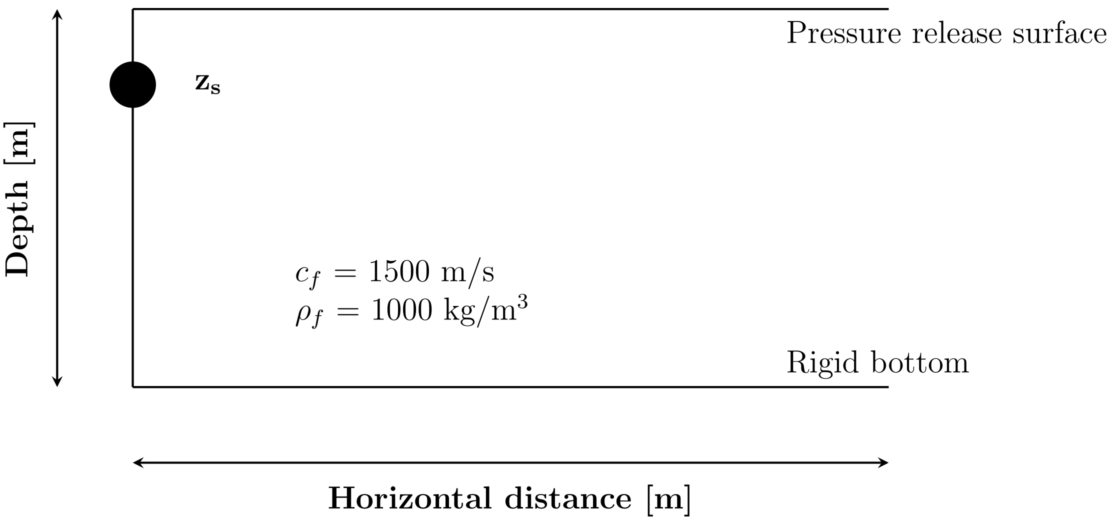

Figure 5.3: Schematic of the ideal fluid waveguide

This equation can be satisfied only if both components, dependent on r and z respectively, are equal to a separation constant k_{rm}^2 obtaining the modal equation for the z-component,

$$\rho_f(z)\frac{\mathrm{d}}{\mathrm{d}z}\left[\frac{1}{\rho_f(z)}\frac{\mathrm{d}\Psi_m(z)}{\mathrm{d}z}\right]+\left[\frac{\omega^2}{c_f^2(z)}-k_{rm}^2\right]\Psi_m(z)=0. \tag{5.22}$$

In the same way, the modal equation can be obtained for the r-component $\Phi(r)$. The modal equations can be solved for the ideal fluid waveguide by imposing the following boundary conditions Jensen et al. (2011),

$$\Psi(0)=0, \tag{5.23}$$

$$\left.\frac{\mathrm{d}\Psi}{\mathrm{d}z}\right|_{z=D}=0. \tag{5.24}$$

A summation of all modes of the vertical and horizontal eigenfunctions multiplied will form a complete set given by Equation (5.25) (Jensen et al., 2011),

$$p(r,z)=\sum_{m=1}^{\infty}\Phi_m(r)\Psi_m(z). \tag{5.25}$$

Substituting Equation (5.25) into Equation (5.20) yields,

$$\begin{aligned}\sum_{m=1}^{\infty}\Bigg\{&\frac{1}{r}\frac{\mathrm{d}}{\mathrm{d}r}\left(r\frac{\mathrm{d}\Phi_m(r)}{\mathrm{d}r}\right)\Psi_m(z)\\&+\Phi_m(r)\left[\rho_f(z)\frac{\mathrm{d}}{\mathrm{d}z}\left(\frac{1}{\rho_f(z)}\frac{\mathrm{d}\Psi_m(z)}{\mathrm{d}z}\right)+\frac{\omega^2}{c_f^2(z)}\Psi_m(z)\right]\Bigg\}=-\frac{\delta(r)\delta(z-z_s)}{2\pi r}.\end{aligned} \tag{5.26}$$

Looking at Equation (5.22), it can be noticed that the term in the square brackets is equal to $k_{rm}^2\Psi_m(z)$ yielding the following equation,

$$\sum_{m=1}^{\infty}\left\{\frac{1}{r}\frac{\mathrm{d}}{\mathrm{d}r}\left(r\frac{\mathrm{d}\Phi_m(r)}{\mathrm{d}r}\right)\Psi_m(z)+k_{rm}^2\Phi_m(r)\Psi_m(z)\right\}=-\frac{\delta(r)\delta(z-z_s)}{2\pi r}. \tag{5.27}$$

By making use of the orthogonality property given by Equation (5.28 and multiplying Equation (5.27) by the operator given by Equation (5.29) only the nth term remains in the sum of Equation (5.27) yielding Equation (5.30) (Jensen et al., 2011).

$$\int_0^D \frac{\Psi_m(z)\Psi_n(z)}{\rho_f(z)}\,\mathrm{d}z=0, \quad \text{for} \quad m\neq n, \tag{5.28}$$

$$\int_0^D (\cdot)\frac{\Psi_n(z)}{\rho_f(z)}\mathrm{d}z, \tag{5.29}$$

$$\frac{1}{r}\frac{\mathrm{d}}{\mathrm{d}r}\left[r\frac{\mathrm{d}\Psi_n(r)}{\mathrm{d}r}\right]+k_{rn}^2\Phi_n(r)=-\frac{\delta(r)\delta(z-z_s)}{2\pi r\rho_f(z_s)}. \tag{5.30}$$

The solution of Equation (5.30) can be given in terms of a Hankel function of the first kind due to the radiation condition that energy should be radiating outward as $r\to\infty$ (Jensen et al., 2011),

$$\Phi_n(r)=\frac{i}{4\rho_f(z_s)}\Psi_n(z_s)H_0^{(1)}(k_{rn}r). \tag{5.31}$$

Substituting this into Equation (5.25) yields the following expression for the pressure in the modal domain,

$$p(r,z)=\frac{i}{4\rho_f(z_s)}\sum_{m=1}^{\infty}\Psi_m(z_s)\Psi_m(z)H_0^{(1)}(k_{rm}r). \tag{5.32}$$

To determine the pressure field in the frequency domain for the ideal fluid waveguide the eigenfunctions $\Psi_m(z)$ need to be determined. This is done by solving the ordinary differential equation given by Equation (5.22) for constant density ρ_f and wavespeed c_f and subsequently filling them in into the boundary conditions given by Equation (5.23 & 5.24). The general solution for the ordinary differential equation is defined by

$$\Psi_m(z)=A\sin(k_z z)+B\cos(k_z z), \tag{5.33}$$

where the vertical wavenumber k_z is given by

$$k_z=\sqrt{\left(\frac{\omega}{c_f}\right)^2-k_r^2}. \tag{5.34}$$

The pressure release boundary condition at $z=0$ implies that $B=0$ while the rigid bottom boundary condition at $z=D$ gives

$$Ak_z\cos(k_z D)=0. \tag{5.35}$$

In order to obtain a non-trivial solution the term in the cosine must be equal to 0 leading to,

$$k_z = \left(m - \frac{1}{2}\right)\frac{\pi}{D}, \quad \text{for} \quad m = 1, 2, ... \tag{5.36}$$

This can be substituted in Equation (5.34) to obtain an expression for the radial wavenumbers given by Equation (5.37) (Jensen et al., 2011).

$$k_{rm} = \sqrt{\left(\frac{\omega}{c_f}\right)^2 - \left[\left(m - \frac{1}{2}\right)\frac{\pi}{D}\right]^2} \tag{5.37}$$

The vertical eigenfunctions belonging to the vertical wavenumbers are defined as follows

$$\Psi_m(z) = \sqrt{\frac{2\rho}{D}}\sin(k_{zm}z), \tag{5.38}$$

where the amplitude A is normalized for sake of simplicity. The expression for the radial wavenumbers and the vertical eigenfunctions can be substituted in the definition for the pressure given by Equation (5.32) to obtain

$$p(r, z) = \frac{i}{2D}\sum_{m=1}^{\infty}\sin(k_{zm}z_s)\sin(k_{zm}z)H_0^{(1)}(k_{rm}r). \tag{5.39}$$

In Figure 5.4 an example of the transmission loss in the frequency domain for an ideal fluid waveguide is shown. The source frequency $f_s = 300$ Hz, the depth $D = 25$ m and the radial distance $R = 750$ m.

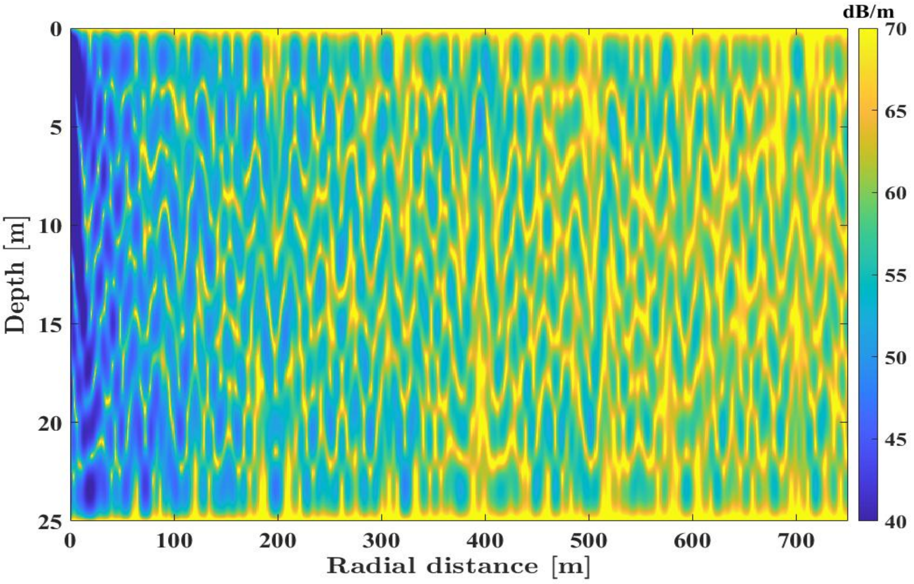

Figure 5.4: Example of transmission loss in an ideal fluid waveguide for a source frequency $f_s = 300$ Hz. Source depth is at $z_s = 5$ m.

5.4 1D approach

The 1D approach is similar to the coupling approach described in Section 3.1.2 where the fluid domain is coupled to the bubbly domain and subsequently coupled to the fluid domain again. By means of the transfer matrix ($\mathbf{A}$), the transfer function ($\tilde{H}(z,\omega)$) can be obtained for the simplified air bubble curtain and can be implemented in the ideal fluid waveguide.

5.5 2D approach

The 2D approach is based on the theory of mode-coupling. Modal analyses are primarily suitable for range-independent environment (Jensen et al., 2011). However, with the placement of the air bubble curtain model at a certain distance from the source, range-dependency is included as the density ρ_f and the effective wavespeed c_f are not constant over the entire radial domain. Range-dependency in modal analyses can be achieved by dividing the range into $N-1$ segments and assuming that the properties in those specific segments are range-independent as illustrated in Figure 5.5 (Jensen et al., 2011).

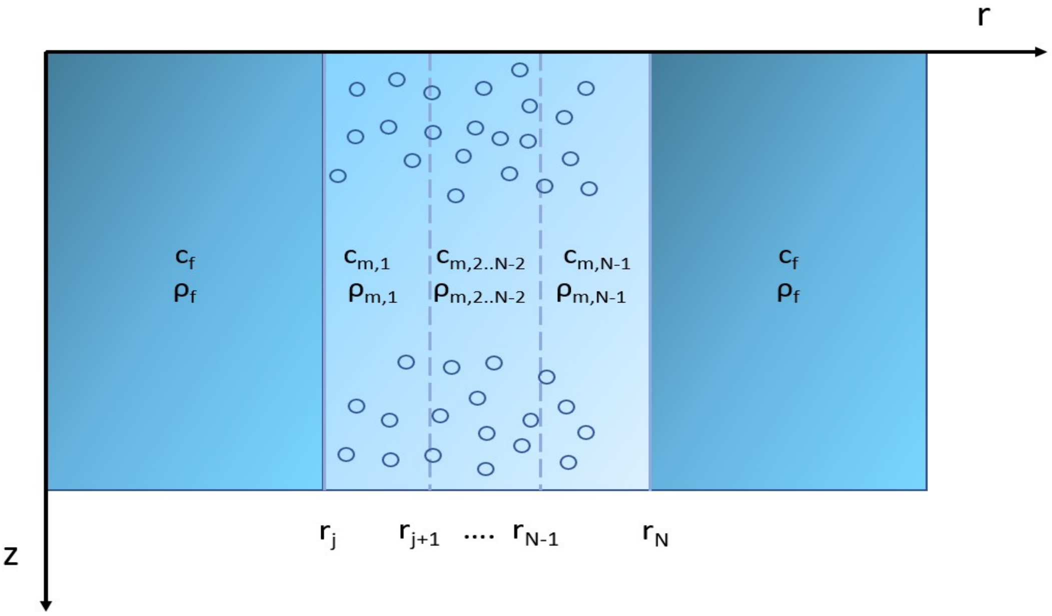

Figure 5.5: Schematic of range dependent air bubble curtain in ideal fluid waveguide

The definition for the pressure for each segment is formulated by Evans (1983) as

$$p^j(r,z) = \sum_{m=1}^{M} \left[a_m^j \hat{H}1_m^j(r) + b_m^j \hat{H}2_m^j(r) \right] \Psi_m^j(z) \tag{5.40}$$

where $\hat{H}1,2$ are the ratios of Hankel functions expressed by their large-argument asymptotic representation given by Equations (5.41 & 5.42) (Jensen et al., 2011).

$$\hat{H}1_m^{j+1}(r) \simeq H1_m^{j+1}(r) = \sqrt{\frac{r_j}{r}} e^{ik_{rm}^{j+1}(r-r_j)}, \tag{5.41}$$

$$\hat{H}2_m^{j+1}(r) \simeq H2_m^{j+1}(r) = \sqrt{\frac{r_{j+1}}{r}}\, e^{ik_{rm}^{j+1}(r_{j+1}-r)}. \tag{5.42}$$

Next, at the interface j continuity of pressure is imposed for M discrete depth points

$$\sum_{m=1}^{M} \left[a_m^{j+1} + b_mj + 1H2_m^{j+1}(r_{j+1})\right] \Psi_m^{j+1}(z) = \sum_{m=1}^{M} \left[a_m^j H1_m^j(r_j) + b_m^j\right] \Psi_m^j(z). \tag{5.43}$$

and an operator similar to the one described by Equation (5.29) is applied,

$$\int_0^D (\cdot) \frac{\Psi_l^{j+1}(z)}{\rho_{f,j+1}(z)} \mathrm{d}z. \tag{5.44}$$

Because of the orthogonality property

$$\int_0^D \frac{\Psi_m^{j+1}(z)\Psi_l^{j+1}(z)}{\rho_{j+1}} \mathrm{d}z = \delta_{lm}, \tag{5.45}$$

with δ_{lm} being the Kronecker delta, only the sum on the right of Equation (5.45) remains, resulting in the following equation.

$$a_l^{j+1} + b_l^{j+1} H2_m^{j+1}(r_{j+1}) = \sum_{m=1}^{M} \left[a_m^j H1_m^j(r_j) + b_m^j\right] \tilde{c}_{lm}, \quad \text{for} \quad l = 1, ..., M, \tag{5.46}$$

where

$$\tilde{c}_{lm} = \int_0^D \frac{\Psi_l^{j+1}(z)\Psi_m^j(z)}{\rho_{j+1}} \mathrm{d}z. \tag{5.47}$$

Equation (5.46) can be written in matrix notation, where the vectors have lengths corresponding to the number of modes, as

$$\mathbf{a}^{j+1} + \mathbf{H}_2^{j+1}\mathbf{b}^{j+1} = \widetilde{\mathbf{C}}^j \Big(\mathbf{H}_1^j \mathbf{a}^j + \mathbf{b}^j\Big). \tag{5.48}$$

In Equation (5.48), $\mathbf{H}_1^j$ and $\mathbf{H}_2^{j+1}$ denote the diagonal matrices with entries $H1_m^j(r_j)$ and $H2_m^{j+1}$ respectively and the matrix $\tilde{\mathbf{C}}$ is the matrix with entries $\tilde{c}_{lm}$. Vectors $\mathbf{a}$ and $\mathbf{b}$ have entries a_l and b_l, respectively.

Similar to Equation (5.43), continuity of radial particle velocity is imposed at the interface j where the radial particle velocity is defined by Jensen et al. (2011) as

$$\frac{1}{\rho_j}\frac{\partial p^j(r,z)}{\partial r} \simeq \frac{1}{\rho_j} \sum_{m=1}^{M} k_{rm}^j \left[a_m^j H1_m^j(r) - b_m^j H2_m^j(r)\right] \Psi_m^j(z). \tag{5.49}$$

Applying the operator

$$\int_0^D (\cdot)\ \Psi_l^{j+1}(z)\ \mathrm{d}z \tag{5.50}$$

leads to the following formulation of the imposed continuity of pressure

$$a_l^{j+1} - b_l^{j+1} H2_m^{j+1}(r_j) = \sum_{m=1}^{M} \left[a_m^j H1_m^j(r_j) - b_m^j \right] \hat{c}_{lm}, \quad \text{for} \quad l = 1, ..., M, \tag{5.51}$$

which can be written in terms in matrix notation similar to Equation (5.48) in the following manner:

$$\mathbf{a}^{j+1} - \mathbf{H}_2^{j+1} \mathbf{b}^{j+1} = \widehat{\mathbf{C}}^j \left(\mathbf{H}_1^j \mathbf{a}^j - \mathbf{b}^j \right). \tag{5.52}$$

Both imposed continuities can be rewritten in matrix notation to obtain an expression for $\mathbf{a}^{j+1}$ and $\mathbf{b}^{j+1}$,

$$\begin{bmatrix} \mathbf{a}^{j+1} \\ \mathbf{b}^{j+1} \end{bmatrix} = \begin{bmatrix} \mathbf{R}_1^j & \mathbf{R}_2^j \\ \mathbf{R}_3^j & \mathbf{R}_4^j \end{bmatrix} \begin{bmatrix} \mathbf{a}^j \\ \mathbf{b}^j \end{bmatrix}, \tag{5.53}$$

where

$$\begin{aligned} \mathbf{R}_1^j &= \frac{1}{2} \left(\widetilde{\mathbf{C}}^j + \widehat{\mathbf{C}}^j \right) \mathbf{H}_1^j, \\ \mathbf{R}_2^j &= \frac{1}{2} \left(\widetilde{\mathbf{C}}^j - \widehat{\mathbf{C}}^j \right), \\ \mathbf{R}_3^j &= \frac{1}{2} \left(\widetilde{\mathbf{C}}^j - \widehat{\mathbf{C}}^j \right) \left(\mathbf{H}_2^{j+1} \right)^{-1} \mathbf{H}_1^j, \\ \mathbf{R}_4^j &= \frac{1}{2} \left(\widetilde{\mathbf{C}}^j + \widehat{\mathbf{C}}^j \right) \left(\mathbf{H}_2^{j+1} \right)^{-1}. \end{aligned} \tag{5.54}$$

To solve this set of linear equations two boundary conditions have to be imposed, one at $r = 0$ and one at $r \to \infty$ (Jensen et al., 2011). The pressure at $r = 0$ is equal to the pressure from the source at $r = r_1$,

$$a_m^1 = \frac{i}{4\rho_f(z_s)} \Psi_m(z_s) H_0^{(1)}(k_{rm}^1 r_1) + b_m^1 \frac{H_0^{(1)}(k_{rm}^1 r_1)}{H_0^{(2)}(k_{rm}^1 r_1)}, \quad \text{for} \quad m = 1, ..., M. \tag{5.55}$$

The radiation condition is satisfied by requiring that $b_m^N = 0$ for all modes.

5.6 Air bubble curtain implementation

In this section the implementation of the air bubble curtain for both approaches is described. First, the effective wavenumber distribution ($k_{eff}(\omega, r, z)$) as a function of depth and width and the width ($b(z)$) as a function of depth have to be determined. The depth of the ideal fluid waveguide is set at 25 meters. For this depth the effective wavenumber distribution is calculated with the approach described in Section 5.1 resulting in a triangular shaped effective wavenumber distribution. This is transformed into a rectangular shaped bubble curtain as a triangular shaped air bubble curtain would require separate eigenfunction definitions for every layer over the vertical. This implies very low local depths which cannot carry real propagating modes due to the cut-off frequency. The width and the radial wavenumber distribution at the top of the air bubble curtain near the sea surface are taken and are applied over the entire air bubble curtain. Figure 5.6 shows the modification from the original to the simplified air bubble curtain model.

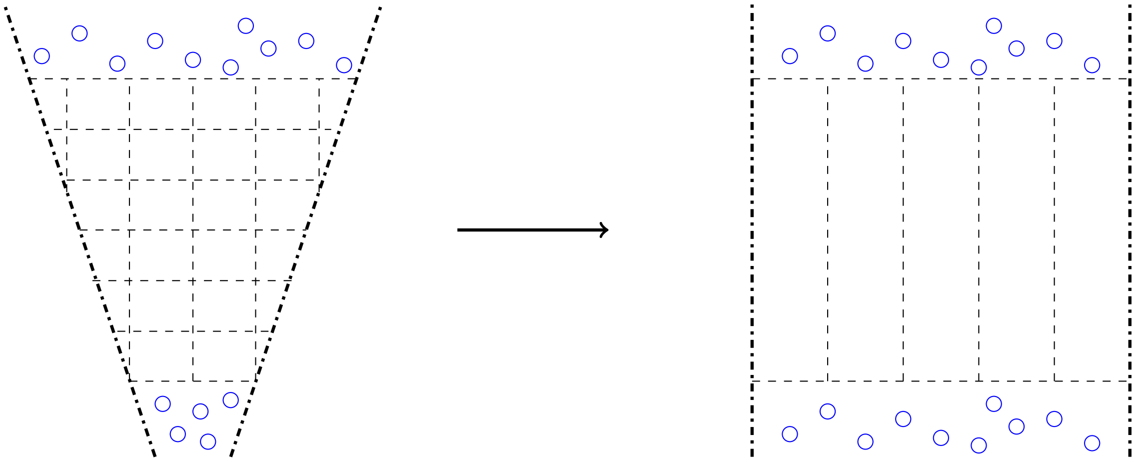

Figure 5.6: Simplification from triangular shaped, depth and width dependent air bubble curtain to rectangular shaped, depth independent air bubble curtain

Since the definition for the eigenfunctions in the ideal fluid waveguide is based solely on real propagating modes only the real part of the complex effective wavenumber distribution of the air bubble curtain is taken into account. The main attribution of noise mitigation therefore shifts from the complex attenuation to reflection and transmission due to the differences in wavenumbers between the layers of the air bubble curtain. Figure 5.7 shows the location of the implemented simplified air bubble curtain illustrated by the white rectangle in an ideal fluid waveguide.

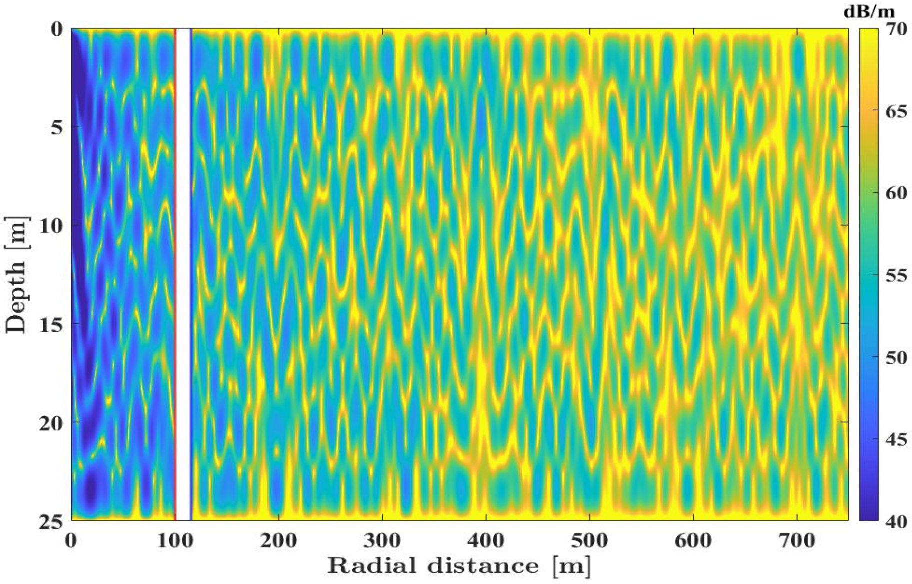

Figure 5.7: Example of transmission loss in an ideal fluid waveguide for a source frequency $f_s = 300$ Hz. Source depth $z_s = 5$ m. The white rectangle at around 100 m indicates the implemented air bubble curtain. The air bubble curtain is not to scale for sake of clarification.

The red vertical line in Figure 5.7 indicates the location of the pressure vector directly before the air bubble curtain ($\mathbf{p}_{\text{before}}$) and the blue vertical line indicates the location of the pressure vector directly after the air bubble curtain ($\mathbf{p}_{\text{after}}$). The pressure vector directly after the air bubble curtain is obtained by the following equation

$$\mathbf{p}_{\text{after}} = \mathbf{p}_{\text{before}} \cdot \tilde{\mathbf{H}}(z, \omega), \tag{5.56}$$

where $\tilde{\mathbf{H}}(z, \omega)$ is the vector containing the transfer coefficients. The pressure vector after the air bubble curtain for the 2D approach is a direct result of the mode-coupling approach. Subsequently, the averaged transmission loss over the depth after the air bubble curtain for the two approaches is calculated in the following manner

$$TL = 10 \log_{10} \left(\sum_{i=1}^{N} \frac{|p_i|^2}{N} \right), \tag{5.57}$$

where N is the number of discrete points over the depth and p_i is the pressure.

5.7 1D versus 2D approach

In this section the 1D and 2D approach are compared. Figure 5.8 shows the transmission loss for three cases, namely directly before the air bubble curtain, directly after the air bubble curtain with the 1D approach and directly after the air bubble curtain with the 2D approach for a depth of 25 meters.

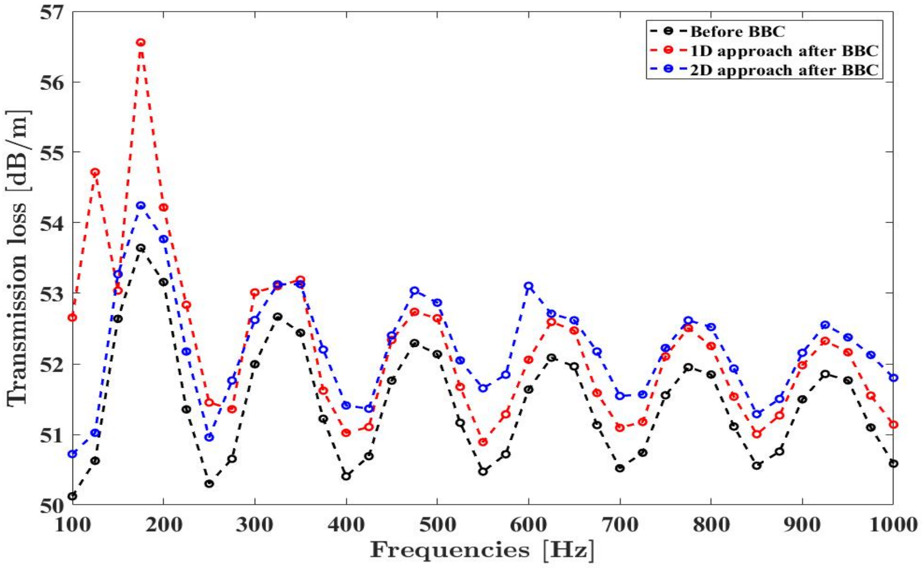

Figure 5.8: Transmission loss for the 1D approach, 2D approach and for the free space before the air bubble curtain. Depth = 25m, air bubble curtain width = 9.4m. Source depth $z_s = 5$ m.

It can be seen from Figure 5.8 that the transmission loss for all three cases is sinus shaped. This is due to the pressure distribution in the ideal fluid waveguide for different frequencies at the specific location of the air bubble curtain for a specific location of the point source. Furthermore, the 2D approach is more conservative for the low frequency regime below $f < 300$ Hz. For higher frequencies, the 1D approach becomes the more conservative approach. The ΔTL is shown in Figure 5.9 for both approaches. This is calculated by the following equations,

$$\Delta \mathrm{TL} = \mathrm{TL}_{\mathrm{1D}} - \mathrm{TL}_{\mathrm{Before}}, \tag{5.58}$$

$$\Delta \mathrm{TL} = \mathrm{TL}_{\mathrm{2D}} - \mathrm{TL}_{\mathrm{Before}}, \tag{5.59}$$

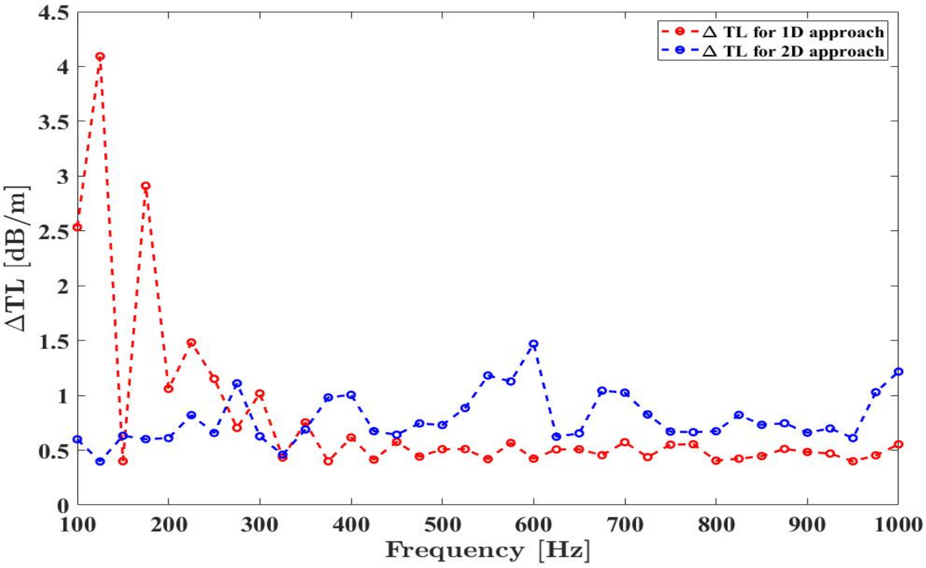

Figure 5.9: ΔTL for the 1D approach and 2D approach. Depth = 25m, air bubble curtain width = 9.4m. Source depth $z_s = 5$ m.

High distinct peaks are visible for $f = 100$ Hz, $f = 125$ and $f = 175$ Hz. The depth of the ideal fluid waveguide is increased to see what the effect is of including more modes for the 2D approach as there are more real propagating modes (see Equation (5.37)). This will not have any effect on the 1D approach as the transfer function is independent on the depth. Figure 5.10 shows the transmission loss for the case before the air bubble curtain, directly after the air bubble curtain with the 1D approach and directly after the air bubble curtain with the 2D approach for a depth of 50 meters. Figure 5.11 shows the ΔTL for both approaches calculated with Equations (5.58 & 5.59).

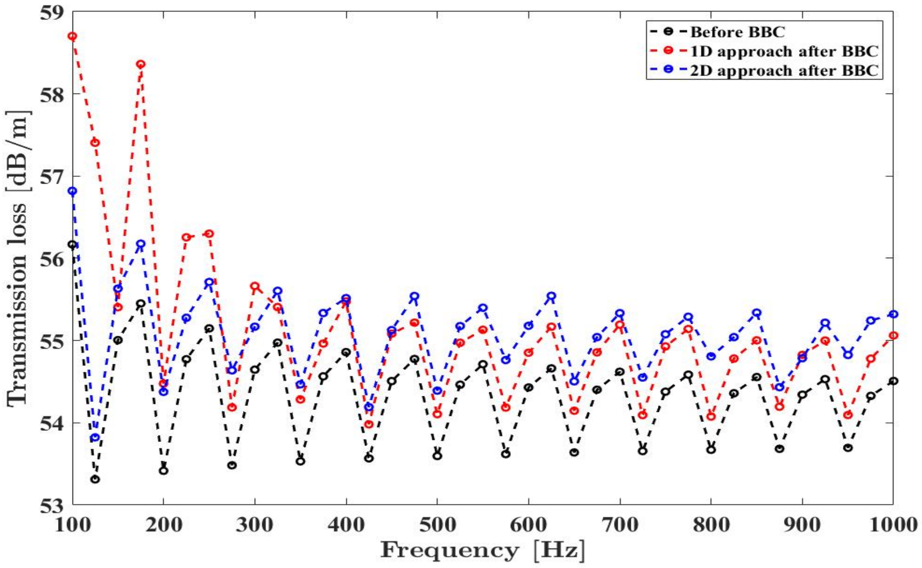

Figure 5.10: Transmission loss for the 1D approach, 2D approach and for the free space before the air bubble curtain. Depth = 50m, air bubble curtain width = 9.4m. Source depth $z_s = 10$ m.

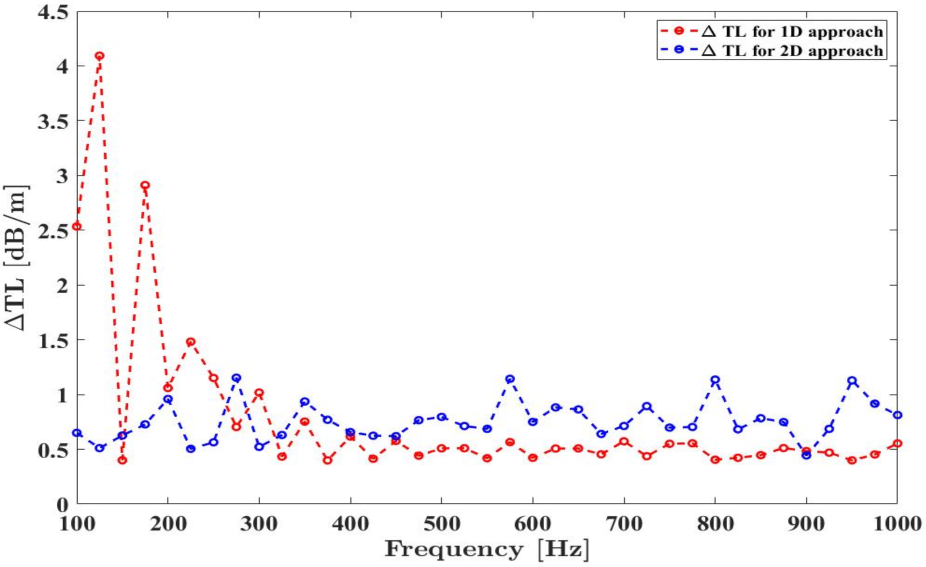

Figure 5.11: ΔTL for the 1D approach and 2D approach. Depth = 50m, air bubble curtain width = 9.4m. Source depth $z_s = 10$ m.

The ΔTL for a depth of 50 meters is more conservative for frequencies below $f < 300$ Hz. For higher frequencies, the 2D approach becomes the more dominant approach with higher transmission losses compared to the 1D approach similar to Figure 5.9. The difference in transmission loss for the low frequencies ($f \leq 300$ Hz) for both Figures 5.9 and 5.11 is significantly higher compared to higher frequencies ($f > 300$ Hz).

Chapter 6

Discussion

The focus of this thesis has been twofold with the overarching theme; "Noise mitigation by a BBC". On the one hand, a study into the optimization of a BBC configuration is performed. On the other hand, an alternative two-dimensional (2D) coupling approach is examined for coupling an air bubble curtain model to a non-mitigated field. This chapter provides a discussion on both subjects where the optimization study is addressed in Section 6.1 and the 2D coupling approach is addressed in Section 6.2. For both subjects, one main research question and two sub-questions were defined.

6.1 Optimizing mitigation by a BBC

The aim was to define a framework for optimizing a BBC configuration for varying soil configurations using the predictive sound propagation and mitigation model SILENCE BUBBLES. The main research question (1, shown in bold) and the two-sub questions (1a, 1b) were defined as follows.

1. **How can the effectiveness of a BBC configuration be optimized with respect to noise mitigation for a variety of scenarios using the predictive modelling software SILENCE BUBBLES?**
    (a) What is the model sensitivity to different BBC parameters and how can this sensitivity be determined by SILENCE BUBBLES?
    (b) What is the effect of different soil configurations on the performance of a BBC?

Prior to working with SILENCE BUBBLES, the sound prediction model SILENCE was validated based on site-specific data of **confidential** at **confidential** made available by Van Oord. The results of this validation were compared to the measurement data. Both the modelled SEL and $L_{p,pk}$ showed good agreement to the measurement data with a deviation of 1.5 dB for SEL and 0.6 dB for $L_{p,pk}$ at 750 meters from the MP (see Figure 3.13).

Validation of SILENCE BUBBLES based on available BBC parameters was not possible. SILENCE BUBBLES accounts for the radial distance of the BBC as well as real BBC parameters such as nozzle diameter and gas velocity at the nozzle. The model is independent of nozzle spacing. The radial distance and the nozzle diameter were obtained from the noise prognosis report for **confidential**. However, the gas velocity at the nozzle was not measured and was therefore unknown. It was outside the scope of this thesis to predict the gas velocities at the nozzles. Therefore the gas velocity was determined iteratively by comparing the modelled SEL to the measured SEL. The gas velocity with the best corresponding SEL was chosen as the base case gas velocity for the sensitivity study. A gas velocity at the nozzle of 108 m/s gave the best comparison to the measured SEL. Based on personal communication with academic staff from TU Delft, it was established that this velocity was within the expected range of gas velocities for a real BBC. The base case BBC parameters are,

- Nozzle diameter: 0.0015 m,
- Gas velocity at the nozzle: 108 m/s.

These base case parameters served as the starting point for the sensitivity study. The sensitivity for each parameter was determined by adding and subtracting 20% of the base case parameters while the other parameter was kept constant. In reality, all BBC parameters are dependent on each other, however, for the purpose of obtaining a theoretical model sensitivity to each BBC parameter, it was deemed reasonable to analyse them independently. It is observed that the model is sensitive to both nozzle diameter and gas velocity at the nozzle with a range of about 2.6 and 1.7 dB, respectively. Furthermore, the model is more sensitive to a decrease than an increase in gas velocity and nozzle diameter for both ΔSEL and $\Delta L_{p,pk}$. This could indicate that a plateau in reduction is reached for increasing BBC parameters. Bellmann et al. (2020) studied the SEL 1/3-Octave reduction for increasing gas velocities, however, these results did not show a clear trend of reaching a plateau. Furthermore, the effect on the SEL at $r = 750$ m for varying radial distances of the BBC was examined. It became clear that the radial distance, nozzle diameter and gas velocity have significant influence on the outcome of SEL at $r = 750$ m and have to be taken into account for the opimization study. Nozzle spacing was omitted in the sensitivity study as the sound reduction module is not dependent of nozzle spacing due to its definition in Peng et al. (2021b). Bohne et al. (2020) states that the nozzle spacing influences the merging of buoyant plumes and therefore the density of bubbles close to the nozzle. This is acknowledged by looking at the results from Rustemeier et al. (2012) where larger nozzle spacing leads to less merging of the bouyant plumes and vice versa. It is therefore suggested that integration of the nozzle spacing in the sound reduction module can have its value for a more complete view on the influence of the BBC parameters on the effectiveness of a BBC. Implementation into SILENCE BUBBLES is necessary to identify its significance for the SEL reduction of the BBC.

To provide more insight on the effect of different soil configurations on the mitigation effectiveness of a BBC configuration, a qualitative analysis was performed for three different soil configurations. The different soil configurations are depicted in Table 6.1.

	Case 1: Top clay		**Case 2: Top sand**		**Case 3: Top mud**	
Parameter	**Value**	**Unit**	**Value**	**Unit**	**Value**	**Unit**
ρ_s	*conf.*	kg/m^3	*conf.*	kg/m^3	1800	kg/m^3
c_p	*conf.*	m/s	*conf.*	m/s	1604	m/s
c_s	*conf.*	m/s	*conf.*	m/s	81	m/s
α_p	*conf.*	dB/m	*conf.*	dB/m	0.033	dB/m
α_s	*conf.*	dB/m	*conf.*	dB/m	0.068	dB/m

Table 6.1: Examined soil configurations for a TLT2.5 and a TLT10.

First, a study into the acoustic responses of the fluid domain for all three cases was conducted up to a distance of $r = 210$ m. This showed a different acoustic response for each soil configuration due to different energy leakage profiles. Two main working mechanisms were identified that cause these differences namely, the influence of Scholte waves and reflections and transmissions in the upper soil layer. The soil characteristics responsible for these phenomena are the shear rigidity of the top soil layer and the impedance mismatch at the soil-soil interface. The principal working mechanisms corresponding to each case are depicted in Figure 6.1.

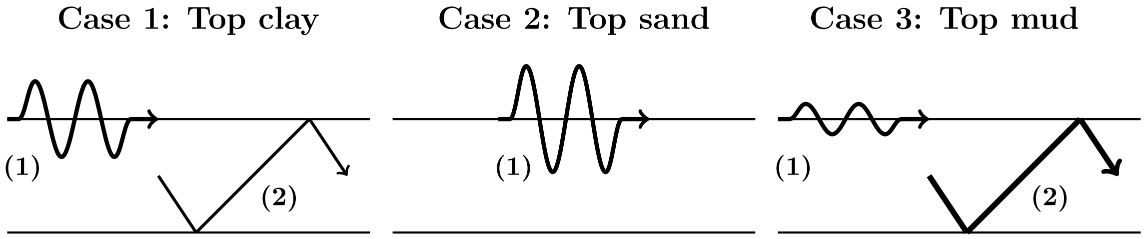

Figure 6.1: Principal working mechanisms for each case where (1) represents the Scholte waves and (2) represents the multiple reflections and transmissions in the upper soil layer.

These different working mechanisms influence the effectiveness of a BBC in twofold. On the one hand, the intrinsic mitigation performance of the BBC is affected by the composition of the propagated sound field in the fluid domain before the BBC. This composition is different for each case (see Figure 4.10). On the other hand, by looking at Figures 4.5 and 4.8, the distribution of energy leaking from the soil domain into the fluid domain over the radial distance is different for each case. This has influence on the SEL at $r = 750$ m.

Focusing on the composition of the propagated sound field before the BBC, Figure 4.10 shows higher low frequency content ($f < 50$ Hz) for Case 1 (Top clay) due to local constructive interference of the Scholte waves, reflections and transmission in the upper soil layer and the Mach wave. Both Scholte waves and reflections and transmissions in the upper soil layer mainly consist of low frequency content (Jensen et al., 2011; Tsouvalas, 2015). Case 2 (Top sand) and 3 (Top mud) show much less local constructive interference due to an absence of reflections and transmissions for Case 2 (Top sand) and small influence of Scholte waves for Case 3 (Top mud). This means that the intrinsic performance is lowest for Case 1 (Top clay). Case 2 (Top sand) shows less energy for frequencies below 20 Hz and higher energy for 50 Hz. It is therefore expected that the intrinsic performance is better for Case 2 (Top sand), followed by Case 3 (Top mud).

Focusing on the distribution of energy over radial distance, Figures 4.5 and 4.8 show that the distribution of energy over the radial distance is different for all cases for a top layer thickness of 2.5 meters (TLT2.5). As stated in the paragraph before, Case 1 (Top clay) leaks more energy into the fluid domain closer to the MP, due to local constructive interference. Further away from the MP, Case 1 (Top clay) shows a steeper decrease in SEL over radial distance compared to Case 2 (Top sand) and 3 (Top mud). Case 2 (Top sand) shows a smooth decay in radial energy and low vertical energy over radial distance due to the fact that there is no impedance mismatch at the soil-soil interface, but only influence of Scholte waves. Case 3 (Top mud) shows low radial energy, but a more capricious vertical energy profile over radial distance. This indicates a larger contribution of the reflections and transmissions in comparison to Case 1 (Top clay) and 2 (Top sand).

To this point, it has been discussed how the energy distributes over radial distance. The differences in distribution are ascribed two different energy leakage mechanisms, namely the Scholte waves and the reflections and transmissions in the upper soil layer and its local interference with each other and with Mach waves coming from the MP. This paragraph will discuss the distribution of energy along the MP in the soil domain and its capability to leak energy from the soil domain into the fluid domain. Looking at the energy distribution of Case 3 (Top mud) over the soil domain for both top layer thicknesses in Figure 4.16, it can be seen that less energy is irradiated in the soil domain close to the fluid-soil interface ($31.9 \leq z \leq 40$ m) for a TLT10 and more energy is irradiated in the soil below $z = 40$ m. As the top layer is less stiff for Case 3 (Top mud), less energy is irradiated into this soil layer. Looking at the SEL at $r = 750$ m for Case 3, it shows a significantly lower SEL for TLT10 with a difference of 3.4 dB in comparison to TLT2.5. It has to be noted that the total energy which is dissipated into the fluid and soil domain is equal for all cases for both top layer thicknesses. This could suggest that the distribution of energy over the length of the MP in the soil domain has a big influence on how much energy can leak into the fluid domain. Apparently, due to these different distributions of energy over the length of the MP for both top layer thicknesses for Case 3 (Top mud), the TLT2.5 is capable of leaking more energy into the fluid domain. This could be caused by the fact that more energy is irradiated into the soil domain in the vicinity of the fluid-soil interface, therefore finding a less demanding path to the fluid domain. Also, the attenuation could play a role. If the energy is irradiated into the soil domain closer to the fluid-soil interface, less travelling distance has to be bridged and therefore less attenuation takes place.

Two phases of energy distribution can be distinguished, namely the distribution of energy over the length of the MP in the soil domain and how the energy which reaches the fluid domain, is distributed over the radial distance. Figure 6.2 schematizes these two different phases of energy distribution.

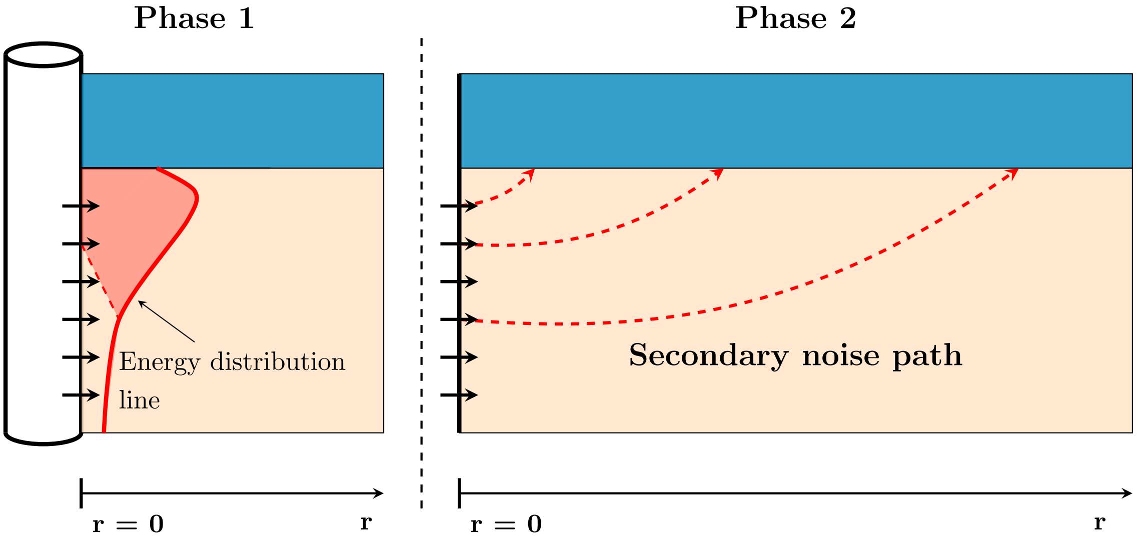

Figure 6.2: Schematization of (Phase 1) the distribution of energy along the MP in the soil domain and (Phase 2) the distribution of the energy over the radial distance. The red area indicates the energy which can reach the fluid domain.

Furthermore, a quantitative analysis was performed for all three cases. A tipping point, the point from where no significant energy leakage from the soil into the fluid domain occurs, was not found for a practical range of 65 to 165 meters. Therefore, the robust approach (see Figure 6.3 was added to the steps shown in Figure 4.20. By looking at the fluctuating SEL results in Figure 4.8 and 4.17, it can be argued whether a tipping point is reached when increasing the range to radial distances above 165 meters. These fluctuations are caused by local constructive interference between the leakage from the soil and reflected Mach waves which indicates energy leakage for radial distances far above practical limitations. For this reason, a robust approach was chosen where each combination of significant parameters (i.e. nozzle diameter, gas velocity at the nozzle and radial position of the BBC) was tested and the corresponding SEL at 750 meters had to comply with a predetermined noise limit. It is important to state that the BBC configuration is a system with complex non-linear behaviour between air supply hose length, nozzle diameter, nozzle spacing and gas velocity at the nozzle. Therefore, it can be argued whether all combinations of parameters can be achieved in practice. By increasing, for example, the nozzle diameter for each nozzle, the pressure loss at the end of the air supply hose is significantly higher and it might be that certain gas velocities cannot be achieved.

What can be seen from Figures 4.22a, 4.22b, and 4.22c is that a distinct optimization for each soil configuration with a TLT2.5 is present. All three cases examined show different combinations of parameters below the noise limit. However, these results should be analyzed with a critical view. The reduction potential is overestimated for Case 2 (Top sand) and 3 (Top mud) and it cannot be said in a quantitative manner what this does to the overall SEL values. If the numerical instabilities (see Section 4.4) are solved, the robust approach could be a tool which could coincide with findings regarding the qualitative analysis, and not yet available literature on pressure losses in air supply hoses, to give a better estimation of the mitigation effectiveness of a BBC configuration.

Results show that for all cases, the reduction potential relative to the optimal reduction by a full block, was between 20 to 60 %. This could indicate a trend, which could be used for future noise prognoses.

SILENCE BUBBLES is able to perform a robust approach. The semi-analytical model allows for separate analyses of the sound generation and propagation module. This means that a simulation of the sound generation module only has to be performed once. Subsequently, it is coupled to the sound propagation module which runs all combinations of parameters to provide a full prediction of the propagated and mitigated sound field making it computationally efficient. However, it has to be stated that SILENCE BUBBLES is an extremely comprehensive model which requires very detailed knowledge about the model setup to be able to properly work with it.

The qualitative and quantitative analysis can be captured within a framework which can be applied to all soil configurations. The framework and its steps are depicted in Figure 6.3.

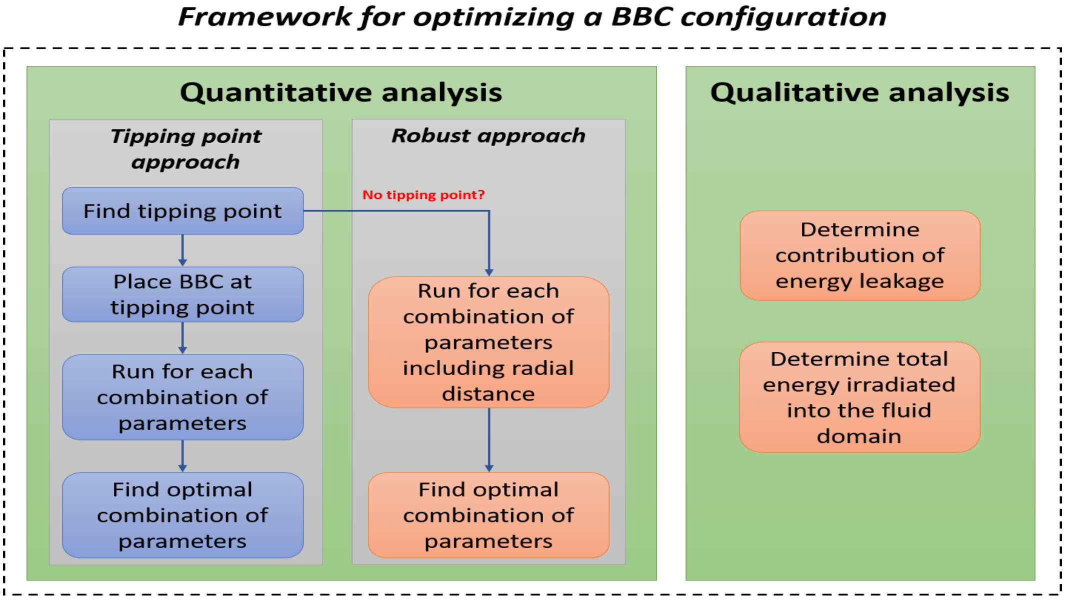

Figure 6.3: Theoretical framework for optimizing a BBC configuration.

6.2 An alternative coupling approach for integrating an air bubble curtain model

The aim for this subject was to examine an alternative coupling approach for coupling an air bubble curtain model to a non-mitigated field. For this purpose, one main research question (2, shown in bold) and two sub-questions (2a, 2b) were defined as follows.

2. **What is the difference between a two-dimensional and a one-dimensional coupling approach with respect to noise mitigation?**
   (a) How can the effect of the two-dimensional coupling approach be modelled?

(b) How can the two-dimensional coupling approach be integrated in SILENCE BUBBLES?

To answer these research questions the air bubble curtain model developed by Bohne et al. (2019) was reproduced. This model was chosen, because it is the basis of the model by Bohne et al. (2020) which is implemented in SILENCE BUBBLES. The bubbly medium is represented by a complex triangular shaped effective wavenumber distribution. This was simplified to a real rectangular shaped effective wavenumber distribution which was subsequently integrated in an ideal fluid waveguide. A characteristic of this waveguide is the definition of only real propagating modes. Therefore, only the real part of the effective wavenumber distribution was taken into account for the bubble curtain. It is worth mentioning that normally, the imaginary part of the effective wavenumbers is the dominant factor for attenuation. However, due to its absence, the attenuation for this air bubble curtain is solely ascribed to reflection and transmission due to the difference in wavenumbers (i.e. wave speeds) between the layers in the bubbly medium. Subsequently, a mode-coupling approach was applied to couple a non-mitigated field to the air bubble curtain.

Looking at the results, it can be observed that for both depths, the 1D approach generates higher transmission losses for frequencies below around 300 Hz and the 2D approach generates higher transmission losses for frequencies above 300 Hz. For the 1D approach, high peaks are visible for $f = 100$ Hz, $f = 125$ and $f = 175$ Hz. It could not be identified how these high peaks originate. A reason might be that a convergence error exists for the lower frequencies which resolves for higher frequencies. That could also explain the fact that the ΔTL for the 1D approach tends to smoothen for higher frequencies. One could also argue that the absence of the evanescent spectrum has more influence on the lower frequency regime due to less propagating modes for this frequency regime. For higher frequencies, more propagating modes are present leading to a better representation of the pressure in comparison to the lower frequency regime. This could be an explanation for the large difference in transmission loss between the 1D and 2D approach. As the evanescent spectrum decays more rapidly over distance than the propagating modes, it is expected that the difference in transmission loss becomes less further away from the MP.

The 2D approach shows on average lower transmission loss for lower frequencies and increases for increasing frequency. This is explained by the increasing number of modes taken into account for higher frequencies. The results show that the 1D approach is more conservative with respect to the 2D approach for frequencies above 300 Hz. This might be due to the fact that angle dependency plays a more significant role for higher order modes due to the shape of the eigenfunctions for higher modes. Neglecting this angle dependency for higher order modes could lead to a conservative transmission loss.

Integration of a rectangular shaped air bubble curtain into SILENCE based on mode-coupling has been done by Tsouvalas and Metrikine (2016). However, this was based on a more simplistic version of a bubbly medium which was constant in composition throughout the air bubble curtain (Tsouvalas, 2020). This thesis incorporates the air bubble curtain model developed by Bohne et al. (2019), however, simplified to a real rectangular shaped wavenumber distribution. Complexity of the wavenumbers can be added by incorporating the air bubble curtain model in a more complex waveguide with additional soil layers. In this way, the definition of the eigenfunctions allow for complexity. The biggest challenge lies in incorporating an air bubble curtain with varying wavenumbers over the depth. A first step could be made by splitting the air bubble curtain into two or three segments over the depth to include depth-dependency in a simplified manner.

Chapter 7

Conclusions and recommendations

This chapter presents the main conclusions of this thesis for both subjects. Section 7.1 describes the main conclusions for optimizing mitigation by a BBC. Section 7.1.1 focuses on the recommendations for this subject. The conclusions about the alternative coupling approach for integrating an air bubble curtain model are presented in Section 7.2 after which Section 7.2.1 discusses the recommendations for this subject.

7.1 Optimizing mitigation by a BBC

- From this study it becomes clear that sensitive parameters of a BBC are the nozzle diameter and the gas velocity at the nozzle. Furthermore, the radial distance of the BBC from the MP is of significant importance for the potential SEL reduction of the BBC at $r = 750$ m.
- SILENCE BUBBLES can be used for a quantitative robust approach for determining an optimal combination of parameters for different soil configurations. Each soil configuration has its own distinct optimization process.
- Together with a qualitative analysis regarding energy distribution over the radial distance and total energy being irradiated into the fluid domain, the framework presented can lead to a better estimation of whether noise limits will be met for future noise prognoses.

7.1.1 Limitations and recommendations

- A limitation of SILENCE BUBBLES is that the nozzle spacing is not included as the sound reduction module is not dependent of the nozzle spacing due to its definition (Peng et al., 2021b). For a complete view on the influence of the BBC parameters, it is therefore recommended to include the nozzle spacing in the sound reduction module.
- The quantitative robust approach shown in this thesis showed numerical instabilities for two cases. These numerical instabilities need to be solved to obtain a reliable quantitative analysis of the robust approach.
- SILENCE BUBBLES is an extremely comprehensive model which requires expert knowledge to use properly. In the early stages of using the model, it is advised to be accompanied by an expert which knows how to use the model.

- Research must be conducted into the non-linear pressure loss behaviour of air supply hoses. In this way, achievable gas velocities at certain nozzle diameter and nozzle spacing can be determined. Together with the presented quantitative approach, this could lead to a solid determination of the optimal combination of parameters to comply with the set noise limit.
- This thesis treats three different soil configurations with two different top layer thicknesses. To generalize the qualitative approach, it is advised to apply this approach to more soil layers and top layer thicknesses. For each soil configuration, the energy composition in the fluid domain before the BBC and the total energy irradiated into the fluid domain can be mapped. Besides the fact that this increases understanding about the influence of soil configurations on the mitigation effectiveness of a BBC, it could be a convenient tool which can be used in future noise prognoses.

7.2 An alternative coupling approach for integrating an air bubble curtain model

- For frequencies higher than 300 Hz, the 1D coupling approach becomes conservative with respect to the 2D coupling approach.

7.2.1 Limitations and recommendations

- The waveguide used in this thesis allows only for the definition of real eigenfunctions therefore accounting only for real propagating modes. Implementing the simplified air bubble curtain into a waveguide with one or more soil layers (e.g., Pekeris waveguide (Jensen et al., 2011)) allows for the definition of complex eigenfunctions. This results in a more complete modal sum which is especially relevant for the low frequencies.
- The definition of complex eigenfunctions in the waveguide allows for the definition of complex wave numbers, and therefore wave speeds, in the bubbly medium. This results in a better approximation of the bubble distribution defined by Bohne et al. (2019, 2020).
- This thesis used a modified rectangular shaped air bubble curtain model. Implementing a triangular shaped air bubble curtain results in a better approximation of the bubble distribution defined by Bohne et al. (2019, 2020). This leads to a more realistic mitigation profile over the depth of the fluid domain as the width of the bubble distribution is smaller at the vicinity of the seabed leading to less mitigation performance in this region.
- It is recommended to extend the used approach for a pile driving source instead of point source to account for a more realistic sound profile hitting the air bubble curtain.

Bibliography

Ainslie, M. (2010). *Principles of sonar performance modelling.* https://doi.org/10.1007/978-3-540-87662-5

Aziman, M., Hazreek, Z. A., Azhar, A. T., & Haimi, D. S. (2016). Compressive and shear wave velocity profiles using seismic refraction technique. *Journal of Physics: Conference Series*, *710*. https://doi.org/10.1088/1742-6596/710/1/012011

Bellmann, M. (2014). Overview of existing noise mitigation systems for reducing pile-driving noise. *INTERNOISE 2014 - 43rd International Congress on Noise Control Engineering: Improving the World Through Noise Control.*

Bellmann, M., May, A., Wendt, T., Gerlach, S., Remmers, P., & Brinkmann, J. (2020). *Underwater noise during percussive pile driving: Influencing factors on pile-driving noise and technical possibilities to comply with noise mitigation values*. Itap GmbH.

Bohne, T., Grießmann, T., & Rolfes, R. (2019). Modeling the noise mitigation of a bubble curtain. *The Journal of the Acoustical Society of America*, *146*. https://doi.org/10.1121/1.5126698

Bohne, T., Grießmann, T., & Rolfes, R. (2020). Development of an efficient buoyant jet integral model of a bubble plume coupled with a population dynamics model for bubble breakup and coalescence to predict the transmission loss of a bubble curtain. *International Journal of Multiphase Flow*, *132*. https://doi.org/10.1016/j.ijmultiphaseflow.2020.103436

Bórawski, P., Bełdycka-Bórawska, A., Jankowski, K. J., Dubis, B., & Dunn, J. W. (2020). Development of wind energy market in the european union. *Renewable Energy*, *161*. https://doi.org/10.1016/j.renene.2020.07.081

Chapman, D. M., & Ellis, D. D. (1998). The elusive decibel: Thoughts on sonars and marine mammals. *Canadian Acoustics - Acoustique Canadienne*, *26*.

Commander, K. W., & Prosperetti, A. (1989). Linear pressure waves in bubbly liquids: Comparison between theory and experiments. *Journal of the Acoustical Society of America*, *85*. https://doi.org/10.1121/1.397599

Degraer, S., Brabant, R., Rumes, B., & Vigin, L. (2018). *Environmental impacts of offshore wind farms in the belgian part of the north sea.* Royal Belgian Institute of Natural Sciences (RBINS).

Evans, R. B. (1983). A coupled mode solution for acoustic propagation in a waveguide with stepwise depth variations of a penetrable bottom. *The Journal of the Acoustical Society of America*, *74*(1), 188–195. https://doi.org/10.1121/1.2133240

Ewing, W. M., Jardetzky, W. S., Press, F., & Beiser, A. (1957). Elastic waves in layered media. *Physics Today*, *10*. https://doi.org/10.1063/1.3060203

Fricke, M. B., & Rolfes, R. (2015). Towards a complete physically based forecast model for underwater noise related to impact pile driving. *The Journal of the Acoustical Society of America*, *137*. https://doi.org/10.1121/1.4908241

Fried, L., Shukla, S., & Sawyer, S. (2017). Growth trends and the future of wind energy. https://doi.org/10.1016/B978-0-12-809451-8.00026-6

Glasbergen, G. J. W. (2020). *Underwater noise: An analysis to the relevant criteria for positioning a bubble curtain*. Delft University of Technology.

Göttsche, K. M., Juhl, P. M., & Steinhagen, U. (2013). Numerical prediction of underwater noise reduction during offshore pile driving by a small bubble curtain. *42nd International Congress and Exposition on Noise Control Engineering 2013, INTER-NOISE 2013: Noise Control for Quality of Life*, *6*.

Hamilton, E. L. (1980). Geoacoustic modeling of the sea floor. *Journal of the Acoustical Society of America*, *68*. https://doi.org/10.1121/1.385100

Jensen, F. B., Kuperman, W. A., Porter, M. B., & Schmidt, H. (2011). *Computational ocean acoustics* (2nd ed.). Springer New York. https://doi.org/10.1007/978-1-4419-8678-8

Kaltenbacher, M. (2018). *Computational acoustics* (M. Kaltenbacher, Ed.; Vol. 579). Springer International Publishing. https://doi.org/10.1007/978-3-319-59038-7

Kaplunov, J. D., Kossovich, L. Y., & Nolde, E. V. (2012). *Dynamics of thin walled elastic bodies*. https://doi.org/10.1016/C2009-0-20923-8

Kargl, S. G. (2002). Effective medium approach to linear acoustics in bubbly liquids. *The Journal of the Acoustical Society of America*, *111*. https://doi.org/10.1121/1.1427356

Kim, Y. H. (2010). *Sound propagation: An impedance based approach*. https://doi.org/10.1002/9780470825853

Klages, E., von Pein, J., Lippert, S., & von Estorff, O. (2019). Reducing offshore pile driving noise: Shape optimization of the impact hammer. *Proceedings of the 23rd International Congress on Acoustics*, 6231–6238.

Kong, D., Liu, Y., Deng, M., & Zhao, X. (2020). Analysis of influencing factors of lateral soil resistance distribution characteristics around monopile foundation for offshore wind power. *Applied Ocean Research*, *97*. https://doi.org/10.1016/j.apor.2020.102106

Koschinski, S., & Lüdemann, K. (2020). *Noise mitigation for the construction of increasingly large offshore wind turbines: Technical options for complying with noise limits*. Federal agency for Nature Conservation.

Kuhn, C., Sychla, H., Stein, P., & Bruns, B. (2014). Dynamic measurements of pile deflections as a source of underwater sound emissions during impact pile driving of offshore pile foundations. *Inter-noise*.

Li, Y., Huang, X., Tee, K. F., Li, Q., & Wu, X. P. (2020). Comparative study of onshore and offshore wind characteristics and wind energy potentials: A case study for southeast coastal region of china. *Sustainable Energy Technologies and Assessments*, *39*. https://doi.org/10.1016/j.seta.2020.100711

Lima, M. A., Mendes, L. F., Mothé, G. A., Linhares, F. G., de Castro, M. P., da Silva, M. G., & Sthel, M. S. (2020). Renewable energy in reducing greenhouse gas emissions: Reaching the goals of the paris agreement in brazil. *Environmental Development*, *33*. https://doi.org/10.1016/j.envdev.2020.100504

Lippert, S., Huisman, M., Ruhnau, M., von Estorff, O., & van Zandwijk, K. (2017). Prognosis of underwater pile driving noise for submerged skirt piles of jacket structures. *4th Underwater Acoustics Conference and Exhibition*, 903–910.

Lippert, S., Lippert, T., Heitmann, K., & Estorff, O. V. (2013). Prediction of underwater noise and far field propagation due to pile driving for offshore wind farms. *Proceedings of Meetings on Acoustics*, *19*. https://doi.org/10.1121/1.4800517

Lippert, S., Nijhof, M., Lippert, T., Wilkes, D., Gavrilov, A., Heitmann, K., Ruhnau, M., Estorff, O. V., Schäfke, A., Schäfer, I., Ehrlich, J., MacGillivray, A., Park, J., Seong, W., Ainslie, M. A., Jong, C. D., Wood, M., Wang, L., & Theobald, P. (2016). Compile - a generic benchmark case for predictions of marine pile-driving noise. *IEEE Journal of Oceanic Engineering*, *41*. https://doi.org/10.1109/JOE.2016.2524738

Lippert, T., Ainslie, M. A., & von Estorff, O. (2018). Pile driving acoustics made simple: Damped cylindrical spreading model. *The Journal of the Acoustical Society of America*, *143*. https://doi.org/10.1121/1.5011158

Martin, S. B., Morris, C., Bröker, K., & O'Neill, C. (2019). Sound exposure level as a metric for analyzing and managing underwater soundscapes. *The Journal of the Acoustical Society of America*, *146*. https://doi.org/10.1121/1.5113578

Meegan, G. D., Hamilton, M. F., Il'inskii, Y. A., & Zabolotskaya, E. A. (1999). Nonlinear stoneley and scholte waves. *The Journal of the Acoustical Society of America*, *106*. https://doi.org/10.1121/1.427920

Müller, A., Juretzek, C., & Boethling, M. (2019). *Assesment of effects of offshore wind energy facilities on the marine environment*. Bundesamt für Seeschifffahrt und Hydrographie (BSH).

Nealy, J. L., Collis, J. M., & Frank, S. D. (2016). Normal mode solutions for seismo-acoustic propagation resulting from shear and combined wave point sources. *The Journal of the Acoustical Society of America*, *139*. https://doi.org/10.1121/1.4944752

Peng, Y., Tsouvalas, A., Stampoultzoglou, T., & Metrikine, A. (2021a). A fast computational model for near- and far-field noise prediction due to offshore pile driving. *The Journal of the Acoustical Society of America*, *149*. https://doi.org/10.1121/10.0003752

Peng, Y., Tsouvalas, A., Stampoultzoglou, T., & Metrikine, A. (2021b). Study of the sound escape with the use of an air bubble curtain in offshore pile driving. *Journal of Marine Science and Engineering*, *9*. https://doi.org/10.3390/jmse9020232

Ramírez, L., Fraile, D., & Brindley, G. (2021). *Offshore wind in europe: Key trends and statistics 2020*. Wind Europe.

Reinhall, P. G., & Dahl, P. H. (2011). Underwater mach wave radiation from impact pile driving: Theory and observation. *The Journal of the Acoustical Society of America*, *130*. https://doi.org/10.1121/1.3614540

Rijkswaterstaat. (n.d.). *Water - getij*. Retrieved October 28, 2021, from https://www.rijkswaterstaat.nl/water/waterdata-en-waterberichtgeving/waterdata/getij

Rijkswaterstaat. (2016). Kavelbesluit ii windenergiegebied borssele [Online; accessed 27 June 2021].

Rustemeier, J., Grießmann, T., & Rolfes, R. (2012). Underwater sound mitigation of bubble curtains with different bubble size distributions. *Proceedings of Meetings on Acoustics*, *17*. https://doi.org/10.1121/1.4772936

Sadorsky, P. (2021). Wind energy for sustainable development: Driving factors and future outlook. *Journal of Cleaner Production*, *289*. https://doi.org/10.1016/j.jclepro.2020.125779

Saidur, R., Islam, M. R., Rahim, N. A., & Solangi, K. H. (2010). A review on global wind energy policy. *Renewable and Sustainable Energy Reviews*, *14*. https://doi.org/10.1016/j.rser.2010.03.007

Sánchez, S., López-Gutiérrez, J. S., Negro, V., & Esteban, M. D. (2019). Foundations in offshore wind farms: Evolution, characteristics and range of use. analysis of main dimensional parameters in monopile foundations. *Journal of Marine Science and Engineering*, *7*. https://doi.org/10.3390/JMSE7120441

Schecklman, S., Laws, N., Zurk, L. M., & Siderius, M. (2015). A computational method to predict and study underwater noise due to pile driving. *The Journal of the Acoustical Society of America*, *138*. https://doi.org/10.1121/1.4922333

Sertlek, H. Ö., & Blacquiere, G. (2019). Effects of the rough sea surface on the signature of a single air gun. *IEEE Journal of Oceanic Engineering*. https://doi.org/10.1109/JOE.2018.2890464

Sokolichin, A., Eigenberger, G., & Lapin, A. (2004). Simulation of buoyancy driven bubbly flow: Established simplifications and open questions. *AIChE Journal*, *50*. https://doi.org/10.1002/aic.10003

Southall, B. L., Finneran, J. J., Reichmuth, C., Nachtigall, P. E., Ketten, D. R., Bowles, A. E., Ellison, W. T., Nowacek, D. P., & Tyack, P. L. (2019). Marine mammal noise exposure criteria: Updated scientific recommendations for residual hearing effects. *Aquatic Mammals*, *45*. https://doi.org/10.1578/AM.45.2.2019.125

Thompson, A., & Taylor, B. (2008). *Guide for the use of the international system of units*. National Institute of Standards and Technology.

Thompson, P. M., Graham, I. M., Cheney, B., Barton, T. R., Farcas, A., & Merchant, N. D. (2020). Balancing risks of injury and disturbance to marine mammals when pile driving at offshore windfarms. *Ecological Solutions and Evidence*, *1*. https://doi.org/10.1002/2688-8319.12034

Tsouvalas, A., & Metrikine, A. V. (2013). A semi-analytical model for the prediction of underwater noise from offshore pile driving. *Journal of Sound and Vibration*, *332*. https://doi.org/10.1016/j.jsv.2013.01.026

Tsouvalas, A., & Metrikine, A. V. (2014). A three-dimensional vibroacoustic model for the prediction of underwater noise from offshore pile driving. *Journal of Sound and Vibration*, *333*. https://doi.org/10.1016/j.jsv.2013.11.045

Tsouvalas, A., & Metrikine, A. V. (2016). Noise reduction by the application of an air-bubble curtain in offshore pile driving. *Journal of Sound and Vibration*, *371*. https://doi.org/10.1016/j.jsv.2016.02.025

Tsouvalas, A. (2015). *Underwater noise generated by offshore pile driving* (Doctoral dissertation). Delft University of Technology.

Tsouvalas, A. (2020). Underwater noise emission due to offshore pile installation: A review. *Energies*, *13*. https://doi.org/10.3390/en13123037

Tsouvalas, A., Peng, Y., & Metrikine, A. (2019). Underwater noise generated by offshore pile driving: A pile-soil-water vibroacoustic model based on a mode matching method. *Underwater Acoustic Conference and Exhibition.*

Wu, X., Hu, Y., Li, Y., Yang, J., Duan, L., Wang, T., Adcock, T., Jiang, Z., Gao, Z., Lin, Z., Borthwick, A., & Liao, S. (2019). Foundations of offshore wind turbines: A review. *Renewable and Sustainable Energy Reviews*, *104*. https://doi.org/10.1016/j.rser.2019.01.012

Würsig, B., Greene, C. R., & Jefferson, T. A. (2000). Development of an air bubble curtain to reduce underwater noise of percussive piling. *Marine Environmental Research*, *49*. https://doi.org/10.1016/S0141-1136(99)00050-1

Appendix A

SILENCE

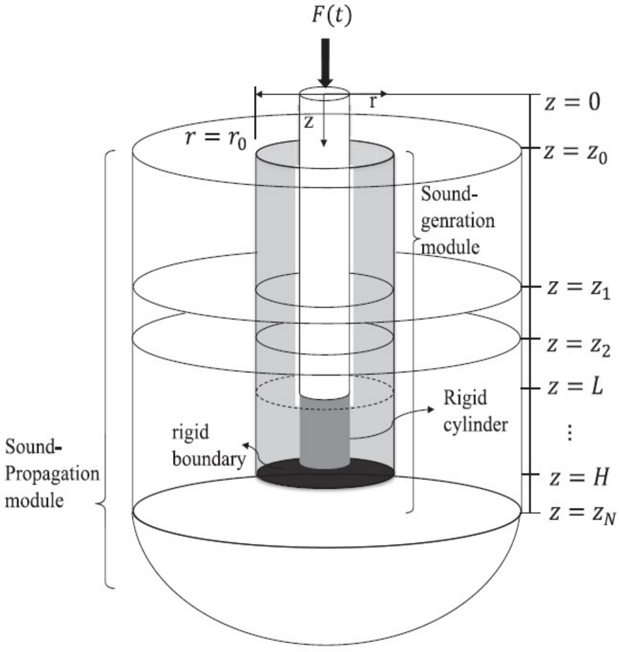

Figure A.1: Schematic of the sound prediction model (Peng et al., 2021a)

A.1 Sound generation module

The following partial differential equations govern the linear dynamic vibration response of the pile-water-soil system in the time domain, where first the shell vibrations are discussed based on the work of Kaplunov et al. (2012) and Tsouvalas (2015). Subsequently, the response of the fluid domain surrounding the monopile is described and lastly, the response of the soil domain is discussed.

A.1.1 Shell vibrations

$$\begin{aligned}\mathbf{Lu} + \mathbf{I\ddot{u}} = -\big(H(z-z_1) - H(z-L)\big)\mathbf{t_s} \\ + \big(H(z-z_0) - H(z-z_1)\big)\mathbf{p_f} + \mathbf{f_e} \quad \text{(A.1)}\end{aligned}$$

In Equation (A.1) **L** represents the stiffness matrix and **I** represents the modified inertia matrix (Tsouvalas & Metrikine, 2014). The displacement of the mid surface of the shell is represented by the vector **u** and the corresponding acceleration vector is represented by $\ddot{\mathbf{u}}$. The vector $\mathbf{t_s}$ represents the boundary stress vector that takes into account the soil surrounding the shell at $\mathrm{z_1 \leq z \leq L}$ (Peng et al., 2021a). The vector $\mathbf{p_f}$ represents the pressure of the fluid on the shell at $\mathrm{z_0 \leq z \leq z_1}$. The externally applied force on the surface of the shell is represented by the vector $\mathbf{f_e}$. The Heaviside functions $H\big(z - z_i\big)$ indicate the domain upon which the soil and the fluid act on the shell. The relevant vectors and their notations are depicted below in a concise manner.

$$\begin{aligned}
\mathbf{u} &= \big[u_z\big(z,t\big)\ \ u_r\big(z,t\big)\big]^T \\
\ddot{\mathbf{u}} &= \big[\ddot{u}_z\big(z,t\big)\ \ \ddot{u}_r\big(z,t\big)\big]^T \\
\mathbf{t}_s^j &= \big[\lambda_s^j \nabla \cdot \mathbf{u_s}^j \mathbf{I} + \mu_s^j \Big(\nabla \mathbf{u_s}^j + \big(\nabla \mathbf{u_s}^j\big)^T\Big)\big] \\
\mathbf{p_f} &= \big[0\ \ p_{f,r}(z,t)\big] \\
\mathbf{f_e} &= \big[f_z\big(z,t\big)\ \ f_r\big(z,t\big)\big]
\end{aligned}$$

$$\tilde{G}\big(\omega\big) = \int_{-\infty}^{\infty} g\big(t\big)e^{-i\omega t}\,dt \ \text{ and } \ g\big(t\big) = \frac{1}{2\pi}\int_{-\infty}^{\infty} \tilde{G}\big(\omega\big)e^{i\omega t}\,dt \tag{A.2}$$

Applying the Fourier transform pair from Equation (A.2) to Equation (A.1) provides the equation for the shell vibrations in the frequency domain.

$$\begin{aligned}
\mathbf{L}\tilde{\mathbf{u}} + \tilde{\mathbf{I}}\tilde{\mathbf{u}} = -\big(H\big(z - z_1\big) - H\big(z - L\big)\big)\tilde{\mathbf{t}}_\mathbf{s} \\
+ \big(H\big(z - z_0\big) - H\big(z - z_1\big)\big)\tilde{\mathbf{p}}_\mathbf{f} + \tilde{\mathbf{f}}_\mathbf{e}
\end{aligned} \tag{A.3}$$

A.1.2 Fluid domain

The response of the inviscid compressible fluid is described by a wave equation for the pressure, assuming constant density in space, in the following manner:

$$\nabla^2 p_f(r,z,t) - \frac{1}{c_f^2}\ddot{p}_f(r,z,t) = 0 \tag{A.4}$$

Equation (A.4) can be written in terms of a displacement potential of the fluid by means of the following relationship,

$$p = -\rho\frac{\partial^2 \psi_f(r,z,t)}{\partial t^2}, \tag{A.5}$$

which leads to the scalar wave equation in terms of a displacement potential $\psi_f(r,z,t)$ depicted in Equation (A.6).

$$\nabla^2 \psi_f\big(r,z,t\big) - \frac{1}{c_f^2}\ddot{\psi}_f\big(r,z,t\big) = 0 \tag{A.6}$$

Applying the Fourier transform pair from Equation (A.2) to Equation (A.6) to go from time to the frequency domain yields the Helmholtz equation:

$$\nabla^2\tilde{\psi}_f\big(r,z,\omega\big)+\frac{\omega^2}{c_f^2}\tilde{\psi}_f\big(r,z,\omega\big)=0 \tag{A.7}$$

A solution to the Helmholtz equation (A.7), based on the method of separation of variables, is given by the following formula which satisfies the radiation condition at infinity.

$$\tilde{\psi}_f(r,z,\omega)=H_0^{(2)}(k_{\psi,f}r)\,\left(A_{f,1}e^{-\alpha_f z}+A_{f,2}e^{\alpha_f z}\right) \tag{A.8}$$

The function $H_0^{(2)}(k_{\psi,f}r)$ is the Hankel function of the first order and of the second kind, $k_{\psi,f}$ is the separation constant, $\alpha_f=\sqrt{k_{\psi,f}^2-\frac{\omega^2}{c_f^2}}$ and $A_{f,1}$ and $A_{f,2}$ are undetermined complex constants. The displacement vector and the pressure fields in the frequency domain are related to the displacement potential in the following manner:

$$\tilde{\mathbf{u}}_{\mathbf{f}}(r,z,\omega)=\nabla\tilde{\psi}_f(r,z,\omega),\ \text{with: }\nabla=\frac{\partial}{\partial r}\hat{r}+\frac{\partial}{\partial z}\hat{z} \tag{A.9}$$

$$\tilde{p}_f(r,z,\omega)=-\omega^2\rho_f\tilde{\psi}_f(r,z,\omega) \tag{A.10}$$

A.1.3 Soil domain

The response of the soil layers can be described by the following set of linear equations (Tsouvalas, 2015)

$$\mu_s^j\nabla^2\mathbf{u}_s^j+(\lambda_s^j+\mu_s^j)\nabla\nabla\cdot\mathbf{u}_s^j=\rho_s^j\frac{\partial^2\mathbf{u}_s^j}{\partial t^2} \tag{A.11}$$

where λ_s^j and μ_s^j are the Lamé constants, $\mathbf{u}_s^j=\left[u_{s,z}^j(r,z,t)\ \ u_{s,r}^j(r,z,t)\right]^T$ is the displacement vector and ρ_s^j is the density of soil layer j. Applying the Fourier transform to Equation (A.9) yields the following equation in the frequency domain.

$$\mu_s^j\nabla^2\tilde{\mathbf{u}}_s^j+(\lambda_s^j+\mu_s^j)\nabla\nabla\cdot\tilde{\mathbf{u}}_s^j=-\omega^2\rho_s^j\tilde{\mathbf{u}}_s^j \tag{A.12}$$

To describe the displacement in a solid body it is convenient to define a scalar potential and a vector potential as follows using the Helmholtz decomposition, $\tilde{\mathbf{u}}_s^j=\nabla\tilde{\phi}_s^j+\nabla\times\tilde{\psi}_s^j$, leading to two uncoupled equations of motion (Ewing et al., 1957; Tsouvalas, 2015).

$$\nabla^2\tilde{\phi}_s^j(r,z,\omega)+\frac{\omega^2}{c_{p_j}^2}\tilde{\phi}_s^j(r,z,\omega)=0 \tag{A.13}$$

$$\nabla^2\tilde{\psi}_s^j(r,z,\omega)-\frac{\tilde{\psi}_s^j(r,z,\omega)}{r^2}+\frac{\omega^2}{c_{s_j}^2}\tilde{\psi}_s^j(r,z,\omega)=0 \tag{A.14}$$

$$c_{p_j}^2=\frac{\lambda_s^j+2\mu_s^j}{\rho_s^j}\ \text{ and }\ c_{s_j}^2=\frac{\mu_s^j}{\rho_s^j} \tag{A.15}$$

The constants c_{p_j} and c_{s_j} denote the compressional and shear wave speeds in each soil layer j respectively. Solutions to both Equations (A.11) and (A.12) are found using the method of separation of variables and can be described by the following equations

$$\tilde{\phi}_s^j(r,z,\omega) = H_0^{(2)}(k_{\phi,p_j}r)\big(A_{s,1}^j e^{-\alpha_{p_j}z} + A_{s,2}^j e^{\alpha_{p_j}z}\big) \tag{A.16}$$

$$\tilde{\psi}_s^j(r,z,\omega) = H_1^{(2)}(k_{\psi,s_j}r)\big(A_{s,3}^j e^{-\beta_{s_j}z} + A_{s,4}^j e^{\beta_{s_j}z}\big), \tag{A.17}$$

where k_{ϕ,p_j} and k_{ψ,s_j} are defined as the separation constants and $\alpha_{p_j} = \sqrt{k_{\phi,p_j}^2 - \frac{\omega^2}{c_{p_j}^2}}$ and $\beta_{s_j} = \sqrt{k_{\psi,s_j}^2 - \frac{\omega^2}{c_{s_j}^2}}$ are the wavenumbers along the vertical direction (Tsouvalas, 2015). $A_{s,1}$, $A_{s,2}$, $A_{s,3}$ and $A_{s,4}$ are undetermined complex constants. The constitutive relation is described as

$$\tilde{\boldsymbol{\sigma}}_s^j = \lambda_s^j \nabla \cdot \tilde{\mathbf{u}}_s^j \mathbf{I} + \mu_s^j\big(\nabla \tilde{\mathbf{u}}_j + (\nabla \tilde{\mathbf{u}}_j)^T\big), \tag{A.18}$$

where $\tilde{\boldsymbol{\sigma}}_s^j$ is the stress tensor and $\mathbf{I}$ is the identity matrix. The displacement-potential and the stress-displacement relations in the frequency domain read (Ewing et al., 1957):

$$\tilde{u}_{s,r}^j(r,z,\omega) = \frac{\partial \tilde{\phi}_s^j(r,z,\omega)}{\partial r} - \frac{\partial \tilde{\psi}_s^j(r,z,\omega)}{\partial z} \tag{A.19}$$

$$\tilde{u}_{s,z}^j(r,z,\omega) = \frac{\partial \tilde{\phi}_s^j(r,z,\omega)}{\partial z} - \frac{1}{r}\frac{\partial\big(r\ \tilde{\psi}_s^j(r,z,\omega)\big)}{\partial r} \tag{A.20}$$

$$\tilde{\sigma}_{s,rr}^j(r,z,\omega) = \lambda_s^j\left(\frac{\partial \tilde{u}_{r,s}^j}{\partial r} + \frac{\tilde{u}_{r,s}^j}{r} + \frac{\partial \tilde{u}_{z,s}^j}{\partial z}\right) + 2\mu_s^j \frac{\partial \tilde{u}_{r,s}^j}{\partial r} \tag{A.21}$$

$$\tilde{\sigma}_{s,zz}^j(r,z,\omega) = \lambda_s^j\left(\frac{\partial \tilde{u}_{r,s}^j}{\partial r} + \frac{\tilde{u}_{r,s}^j}{r} + \frac{\partial \tilde{u}_{z,s}^j}{\partial z}\right) + 2\mu_s^j \frac{\partial \tilde{u}_{z,s}^j}{\partial z} \tag{A.22}$$

$$\tilde{\sigma}_{s,zr}^j(r,z,\omega) = \mu_s^j\left(\frac{\partial \tilde{u}_{r,s}^j}{\partial z} + \frac{\partial \tilde{u}_{z,s}^j}{\partial r}\right) \tag{A.23}$$

A.1.3.1 Boundary and interface conditions

The radiation condition at infinity for the velocity potential of the fluid and the velocity and displacement potential of the soil is already incorporated in the Equations (A.8), (A.16 & A.17) by means of the Hankel functions. The remaining complex unknown constants $A_{f,1}$, $A_{f,2}$, $A_{s,1}^j$, $A_{s,2}^j$, $A_{s,3}^j$ and $A_{s,4}^j$ can be expressed in one unknown complex constant by imposing the following boundary and interface conditions. This unknown constant can be determined by solving for the force response of the complete system, however this derivation is omitted for sake of brevity. For the detailed derivation, the reader is referred to the works of Peng et al. (2021a) and Tsouvalas (2015).

$$\tilde{p}_f(r,z_0,\omega) = 0,\ r \geq R \tag{A.24}$$

$$\tilde{\sigma}_{s,zz}^1(r,z_1,\omega) + \tilde{p}_f(r,z_1,\omega) = 0,\ r \geq R \tag{A.25}$$

$$\tilde{\sigma}_{s,zr}^1(r,z_1,\omega) = 0,\ r \geq R \tag{A.26}$$

$$\tilde{u}^1_{s,z}(r, z_1, \omega) - \tilde{u}_{f,z}(r, z_1, \omega) = 0,\ r \geq R \tag{A.27}$$

Equation (A.24) represents the pressure release boundary condition at the sea surface at $z = z_0$. At the fluid-soil interface at $z = z_1$ the continuity of vertical displacement and the continuity of traction normal to the interface must be satisfied, which is depicted in Equations (A.25 - A.27), respectively. At the soil-soil interfaces the displacement continuity and the stress equilibrium condition apply, which is given in Equations (A.28 - A.31).

$$\tilde{u}^j_{s,z}(r, z_j, \omega) = \tilde{u}^{j-1}_{s,z}(r, z_j, \omega),\ \ 2 \leq j \leq N,\ r \geq R \tag{A.28}$$

$$\tilde{u}^j_{s,r}(r, z_j, \omega) = \tilde{u}^{j-1}_{s,r}(r, z_j, \omega),\ \ 2 \leq j \leq N,\ r \geq R \tag{A.29}$$

$$\tilde{\sigma}^j_{s,zz}(r, z_j, \omega) = \tilde{\sigma}^{j-1}_{s,zz}(r, z_j, \omega),\ \ 2 \leq j \leq N,\ r \geq R \tag{A.30}$$

$$\tilde{\sigma}^j_{s,zr}(r, z_j, \omega) = \tilde{\sigma}^{j-1}_{s,zr}(r, z_j, \omega),\ \ 2 \leq j \leq N,\ r \geq R \tag{A.31}$$

At a depth $z = H$ a rigid boundary condition is applied, which is represented by the following two equations.

$$\tilde{u}^N_{s,z}(r, D, \omega) = 0,\ r \geq R \tag{A.32}$$

$$\tilde{u}^N_{s,r}(r, D, \omega) = 0\ \ r \geq R \tag{A.33}$$

At the pile-water interface the kinematic continuity boundary condition is imposed (A.34). At the pile-soil interface the assumption of a perfect connection is imposed, leading to no-slip boundary conditions (A.35 & A.36).

$$\tilde{u}_r(z, \omega) - i\omega\tilde{v}_{f,r}(R, z, \omega) = 0,\ \ z_0 < z < z_1 \tag{A.34}$$

$$\tilde{u}_r(z, \omega) - \tilde{u}^j_{s,r}(R, z, \omega) = 0,\ \ z_1 < z < z_N \tag{A.35}$$

$$\tilde{u}_z(z, \omega) - \tilde{u}^j_{s,z}(R, z, \omega) = 0,\ \ z_1 < z < z_N \tag{A.36}$$

A.2 Sound propagation module

The sound generation module discussed in the previous section can be used to predict the wave field up to any distance from the pile. However, the rigid boundary condition at $z = H$ causes reflections travelling back into the soil and the water column which are not realistic, but a by-product of the model set-up (Tsouvalas, 2020). To overcome this problem, a propagation module was developed which is coupled to the generation module and takes the output of the generation module as input. The way this is done is by modelling a ring source in cylindrical coordinates at the radial boundary of the generation module in both the fluid and the soil domain, where a pressure-type ring source is placed in the fluid and a pressure- and shear-type ring source is placed in the soil. A representation of the ring source is given in the following Figure 3.2.

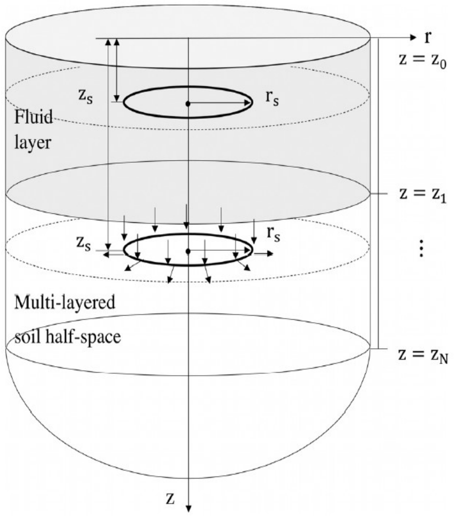

Figure A.2: Representation of the ring source at the radial boundary of the generation module (Peng et al., 2021a)

A.2.1 Ring source in the fluid domain

The acoustic wave field in the fluid domain of a ring source with unit amplitude in cylindrical coordinates in the frequency domain can be described by the following equation (Peng et al., 2021a), which describes the equation of motion for the fluid displacement potential.

$$\left[\nabla^2 + k_{\psi,f}^2\right]\tilde{\psi}_{f,f}^{g}(r,z;r_s,z_s,\omega) = \frac{1}{-\rho\omega}\frac{\delta(r-r_s,z-z_s)}{2\pi r} \tag{A.37}$$

For a ring source in the fluid domain the equations of motion for the soil displacement potentials are homogeneous and as follows,

$$\left[\nabla^2 + k_{\phi,p_j}^2\right]\tilde{\phi}_{s,f}^{j,g}(r,z;r_s,z_s,\omega) = 0, \tag{A.38}$$

$$\left[\nabla^2 + k_{\psi,s_j}^2\right]\tilde{\psi}_{s,f}^{j,g}(r,z;r_s,z_s,\omega) = 0, \tag{A.39}$$

where the first superscript stands for the soil layer j and the second superscript stands for the Green's potential function. The second subscript stands for the location of the source, either f or s, representing either the fluid or the soil domain, respectively. Applying the Hankel transform and integration by parts with respect to the r-coordinate to Equations (A.37 - A.39) yields the following depth-separated wave equations in the Hankel domain (Jensen et al., 2011; Peng et al., 2021a),

$$\left[\frac{d^2}{dz^2} + k_{z,f}^2\right]\hat{\psi}_{f,f}^{g}(k_r,z;r_s,z_s,\omega) = \frac{1}{-\rho\omega}\frac{\delta(z-z_s)}{2\pi}J_0(k_r,r_s), \tag{A.40}$$

$$\left[\frac{d^2}{dz^2} + k_{z,p_j}^2\right]\hat{\phi}_{s,f}^{j,g}(k_r,z;r_s,z_s,\omega) = 0, \tag{A.41}$$

$$\left[\frac{d^2}{dz^2}+k_{z,s_j}^2\right]\hat{\psi}_{s,f}^{j,g}(k_r,z;r_s,z_s,\omega)=0, \tag{A.42}$$

where $k_{z,\xi}=\sqrt{k_{\Xi,\xi}^2-k_r^2}$ for $\Xi=(\psi,\phi,\psi)$ and $\xi=(f,p_j,s_j)$, respectively. The solutions to Equations (A.40 - A.42) described above are the sum of the particular and the general solution to these equations, where the homogeneous equations only have a general solution,

$$\hat{\psi}_{f,f}^{g}\left(k_r,z;r_s,z_s,\omega\right)=\left(\frac{1}{-\rho\omega^2}\frac{e^{-ik_{z,f}|z-z_s|}}{4\pi ik_{z,f}}+A_1^g e^{ik_{z,f}z}+A_2^g e^{-ik_{z,f}z}\right)J_0\left(k_r r_s\right), \tag{A.43}$$

$$\hat{\phi}_{s,f}^{j,g}\left(k_r,z;r_s,z_s,\omega\right)=\left(A_{s,1}^{j,g}e^{ik_{z,p_j}z}+A_{s,2}^{j,g}e^{-ik_{z,s_j}z}\right)J_0\left(k_r r_s\right), \tag{A.44}$$

$$\hat{\psi}_{s,f}^{j,g}\left(k_r,z;r_s,z_s,\omega\right)=\left(A_{s,3}^{j,g}e^{ik_{z,p_j}z}+A_{s,4}^{j,g}e^{-ik_{z,s_j}z}\right)J_0\left(k_r r_s\right), \tag{A.45}$$

where the same boundary and interface conditions as stated in Section A.1.3.1 apply for Equations (A.43 - A.45). Going from the wavenumber domain to the frequency domain requires the application of the inverse Hankel transform to Equations (A.43 - A.45) which yields the solutions of the fluid and soil potentials in the frequency domain (Peng et al., 2021a),

$$\tilde{\mathbf{\Phi}}_{\Xi}^{g}\left(r,z;r_s,z_s,\omega\right)=-\frac{1}{2}\int_{-\infty}^{+\infty}\left(\hat{\mathbf{\Phi}}_{\Xi}^{g}\left(k_r,z;r_s,z_s,\omega\right)\right)H_0^{(2)}\left(k_r r\right)k_r dk_r, \tag{A.46}$$

where $\tilde{\mathbf{\Phi}}_{\Xi}^{g}=[\tilde{\psi}_{f,f}^{g},\tilde{\phi}_{s,f}^{j,g},\tilde{\psi}_{s,f}^{j,g}]^T$ represents the solutions of the potential functions in the frequency domain. In the same manner as done in Section A.1 the potential functions can be rewritten in terms of pressure, displacement and stress. For sake of brevity these equations have been omitted.

A.2.2 Ring source in the soil domain

The potential functions for a ring source in the soil domain are quite similar to the potential functions for a ring source in the fluid domain described by Equations (A.43 - A.45), except from the partical solution in Equation (A.43) and are given by Equations (A.47 - A.49). The homogeneous solutions of the displacement potentials for the soil are equal to Equations (A.44 & A.45).

$$\hat{\psi}_{f,s}^{g}\left(k_r,z;r_s,z_s,\omega\right)=\left(A_1^g e^{ik_{z,f}z}+A_2^g e^{-ik_{z,f}z}\right)J_0\left(k_r r_s\right), \tag{A.47}$$

$$\hat{\phi}_{s,s}^{j,g}\left(k_r,z;r_s,z_s,\omega\right)=\left(A_{s,1}^{j,g}e^{ik_{z,p_j}z}+A_{s,2}^{j,g}e^{-ik_{z,s_j}z}\right)J_0\left(k_r r_s\right), \tag{A.48}$$

$$\hat{\psi}_{s,s}^{j,g}\left(k_r,z;r_s,z_s,\omega\right)=\left(A_{s,3}^{j,g}e^{ik_{z,p_j}z}+A_{s,4}^{j,g}e^{-ik_{z,s_j}z}\right)J_0\left(k_r r_s\right), \tag{A.49}$$

To account for the source, a jump condition is applied to describe the relationship between the stresses just above and below the location of the source as a result of the local stress increase. For the radial load case, the interface conditions in the Hankel domain are as follows:

$$\hat{\sigma}^{+,g}_{zr,z_s}\left(k_r, z_s, \omega\right) - \hat{\sigma}^{-,g}_{zr,z_s}\left(k_r, z_s, \omega\right) = \frac{J_0\left(k_r r_s\right)}{2\pi}, \tag{A.50}$$

$$\hat{\sigma}^{+,g}_{zz,z_s}\left(k_r, z_s, \omega\right) - \hat{\sigma}^{-,g}_{zz,z_s}\left(k_r, z_s, \omega\right) = 0, \tag{A.51}$$

$$\hat{u}^{+,g}_{\alpha,z_s}\left(k_r, z_s, \omega\right) - \hat{u}^{-,g}_{\alpha,z_s}\left(k_r, z_s, \omega\right) = 0, \quad \text{with} \quad \alpha = r, z, \tag{A.52}$$

where the second subscript z_s indicates the location of the ring source. Similarly, the interface conditions for the vertical load case in the Hankel domain can be written as:

$$\hat{\sigma}^{+,g}_{zr,z_s}\left(k_r, z_s, \omega\right) - \hat{\sigma}^{-,g}_{zr,z_s}\left(k_r, z_s, \omega\right) = 0, \tag{A.53}$$

$$\hat{\sigma}^{+,g}_{zz,z_s}\left(k_r, z_s, \omega\right) - \hat{\sigma}^{-,g}_{zz,z_s}\left(k_r, z_s, \omega\right) = \frac{J_0\left(k_r r_s\right)}{2\pi}, \tag{A.54}$$

$$\hat{u}^{+,g}_{\alpha,z_s}\left(k_r, z_s, \omega\right) - \hat{u}^{-,g}_{\alpha,z_s}\left(k_r, z_s, \omega\right) = 0, \quad \text{with} \quad \alpha = r, z, \tag{A.55}$$

A combination of interface conditions at the height of the source given by Equations (A.50 - A.55) and the interface and boundary conditions given by Equations (A.24 - A.33) yields a system of linear algebraic equations of 4N+6 equations with equally many unknowns. In this way the displacement potentials can be solved in the Hankel domain and can be rewritten to the frequency domain. The sound generation module and the sound propagation module can then be coupled via a boundary integral formulation described by Peng et al. (2021a) and Tsouvalas (2020).

Appendix B

Soil profile

Figure B.1: Overview of the soil profile provided by the engineering report.

Appendix C

Comparison between small and large near field

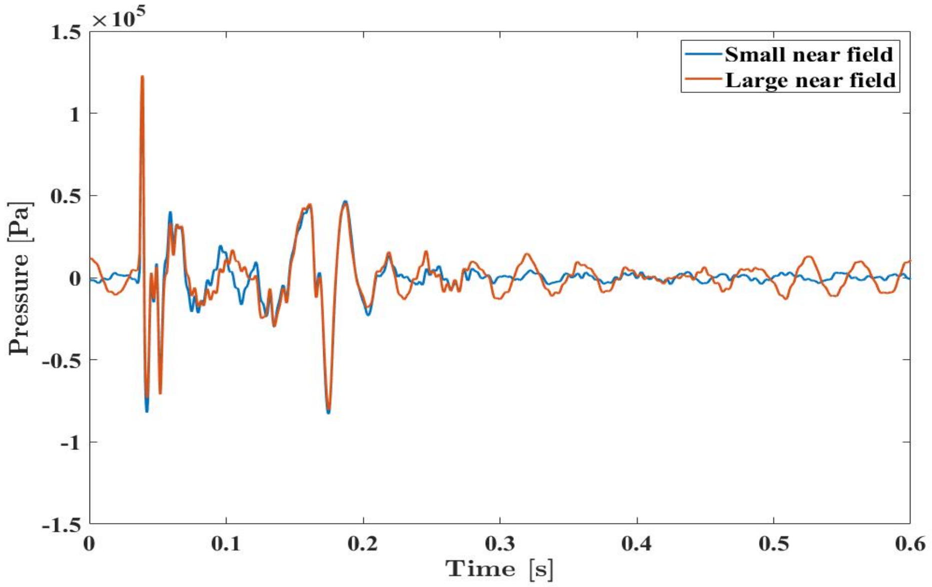

Figure C.1: Comparison between the pressure time signals for the small and large near field at 0.2 meters from the seabed at a radial distance of 48.7 meters

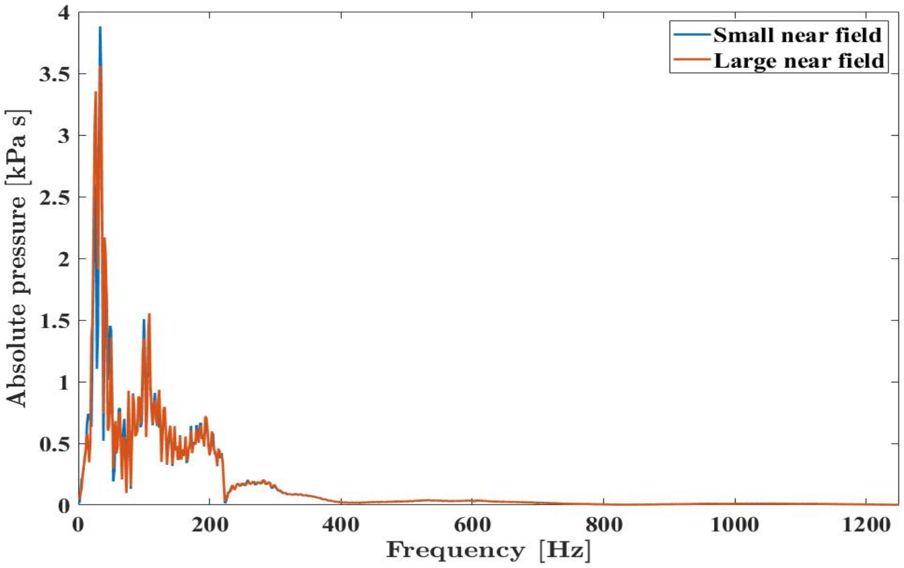

Figure C.2: Comparison between the pressure frequency spectra for the small and large near field at 0.2 meters from the seabed at a radial distance of 48.7 meters